Design of Traveling Wave SIW Antennas for 5G Base Stations

by

Fatemeh Mohamadi Monavar

A thesis submitted in partial fulfillment of the requirements for the degree of

Doctor of Philosophy

in
Electromagnetics and Microwaves

Department of Electrical and Computer Engineering
University of Alberta

Abstract

This thesis describes new configurations of traveling wave antenna arrays. The ability of traveling wave antennas to integrate radiating element with transmission line in one single device which can be easily fed, are among reasons for popularity of such structures. Leaky-wave antennas (LWA) can achieve highly directive beams that can be scanned with frequency which is very advantageous for wide angle scanning applications. Some applications however prefer a fixed broadside beam over a tilted off-broadside leaky-wave beam. In this case slot arrays are a more suitable choice. Both leaky-wave and slot arrays are studied in this thesis with regards to application in 5G base station antennas (BSA).

A new double layer subarray configuration for leaky-wave antenna at 15 GHz is presented. The structure is capable of frequency scanning a highly directive beam in the elevation and switching a flat-topped beam to illuminate specific regions of space in the azimuth. A cylindrical arrangement of such antennas is shown to be highly efficient for multi-beam antenna solutions. Beam-shaping in the array is done by *virtually* moving phase centers through appropriate port-excitations without physically changing antenna structures or need for phase shifters. Far-field patterns, scattering parameters and isolation between two leaky-wave antennas in the subarray are examined and show good agreement with the measurement results.

Our design of narrow-wall waveguide slotted array at 26 GHz serves to provide some additional features for BSA such as circular polarization (CP) and broadside radiation. More importantly CP is accomplished through reflection-cancelling slot pair unit cells on the *narrow wall* which compared to its broad wall counterparts more frequently discussed in literature, can considerably reduce the size of future planar arrays. Owing to the novel multilayer PCB topology employed, our design can easily be changed to operate at a new frequency with a different feeding system and unlike bulky waveguides is capable of full integration with planar circuitry. Near field, far-field, and scattering properties are evaluated in detail which show radiation performance according to desired Taylor aperture distribution is obtainable.

PREFACE

This thesis is an original work by Fatemeh Mohamadi Monavar.

Chapter 3 is published in The *IEEE Transactions on Antennas and Propagation*, vol. 65, no. 3. pp. 1108-1120, Feb 2017. by **F. M. Monavar,** S. Shamsinejad, R. Mirzavand, J. Melzer and P. Mousavi, **"**Beam-Steering SIW Leaky-Wave Subarray with Flat-Topped Footprint for 5G Applications" **F. M. Monavar,** S. Shamsinejad, and P. Mousavi, also published a conference paper **"**Beam-Steering Slotted Leaky Wave Antenna with Flexible Control of Azimuth Pattern". *Antennas and Propagation* (*AP-S/URSI) 2016 IEEE International Symposium on, Fajardo, PR, USA, July 2016.* pp.79-80. In both publications, I was responsible for design, simulation and manuscript composition under the supervision of Dr. P. Mousavi. S. Shamsinejad assisted with the design and analysis. Measurements were conducted with the help of R. Mirzavand using the lab facilities provided by Dr. P. Mousavi. Dr. P. Mousavi along with J. Melzer contributed to manuscript edits.

Chapter 5 of this thesis is yet to be published.

ACKNOWLEDGEMENT

I would like to express my deepest appreciation to my supervisor, firstly for giving me the opportunity to be part of his research team at University of Alberta and for his advice, guidance and patience over the past few years. I would like to place on record my gratitude for his crucial role in providing lab facilities and all the material and measurement equipment necessary for my project. I am also thankful to all the thesis committee members who took time out of their busy schedule to read this document and provide valuable feedbacks. I would like to acknowledge TELUS, NSERC and TR-Tech, for their generous funding of my PhD project. I am also grateful to ECE professors and FGSR staff at University of Alberta for nominating me for the Myer Horowitz Graduate Students' Association Scholarship, and Queen Elizabeth II Graduate Scholarship. I would like to take this opportunity to thank my fellow students at University of Alberta for their valuable insight and suggestions, course of friendship and collaboration which helped me in my doctoral research. I am also gratefully indebted to our graduate student advisor Ms. Pinder Bains, for her kind support.

Last but not least I'd like to thank my parents, my beautiful family and wonderful friends for their consistent support, encouragement and all the last-minute favors.

Table of contents

Contents

Table of contents

Table of contents

List of Tables

List of Figures

List of Abbreviations

ABF	Adaptive beamforming
AR	Axial ratio
BER	Bit error rate
BSA	Base station antenna
CBCPW	Conductor-backed coplanar waveguide
C/I	Carrier-to-interference
CP	Circularly polarized
CPW	Coplanar waveguide
CRLH	Composite right/left-handed
CSI	Channel state information
EBG	Electromagnetic bandgap
EFIE	Electric field integral equation
EM	Electromagnetic
GO	Geometric Optics
HFSS	High frequency structure simulator
HMSIW	Half mode substrate integrated waveguide
HPBW	Half power beamwidth
HWMLWA	Half width microstrip leaky-wave antenna
LHCP	Left hand circular polarization
LMDS	Local multipoint distribution systems
LOS	Line of sight
LTCC	Low temperature co-fired ceramic
LTE	Long term evolution
LWA	Leaky-wave antenna
MIMO	Multi input multi output
MLWA	Microstrip leaky-wave antenna
PCB	Printed circuit board
PEC	Perfect electric conductor
PRS	Partially reflective surface

RF	Radio frequency
RHCP	Right hand circular polarization
RTSA	Real time spectrum analyzer
SIW	Substrate integrated waveguide
SLL	Sidelobe level
SMA connector	SubMiniature version A connector
SMP connector	SubMiniature push on connector
SMRS	Sinusoidally modulated reactance surface
SNR	Signal to noise ratio
S-parameters	Scattering parameters
TE	Transverse electric
TEM	Transverse electromagnetic
TEN	Transverse equivalent network
TM	Transverse magnetic
TRM	Transverse resonance method
TWA	Traveling wave array
WRC	World radio conference

List of Symbols

α	Attenuation (leakage) constant
β	Phase (propagation) constant
β_{10}	Propagation constant of TE10 mode
$\Delta\theta$	Beamwidth in the elevation plane
ε_o	Free space permittivity constant
ε_r	Relative dielectric permittivity
ϵ	Error function
η	Antenna aperture efficiency
θ	Elevation angle
θ_{INC}	Incidence angle
θ_{rad}	Main beam pointing angle
λ_g	Guided wavelength
λ_r	Dielectric wavelength
λ_o	Free space wavelength
μ_o	Free space permeability constant
ρ_P	Reflection coefficient
φ	Azimuth angle
ω	Angular frequency
A_{eff}	Antenna effective aperture
A_{ph}	Antenna physical aperture
c	Free space phase velocity
C_n	Slot radiation coefficients
f_c	Cutoff frequency
k_o	Free space wavenumber
k_x	Wavenumber along x
k_y	Wavenumber along y
k_z	Wavenumber along z
P_{in}	Array input power

P_k	Slot radiated power
S11	Input reflection coefficient
|S12|	Reverse insertion loss
S22	Output reflection coefficient
|S21|	Forward insertion loss
v_k	Array excitation coefficient
Z_o	Characteristic impedance
Z_{RAD}	Radiation impedance

Chapter 1

1 Introduction

1.1 5G Base Station Antenna

With the emergence of 5G network and its diverse range of applications from medical and household appliances, monitoring and safety to mobile communications, introducing a new class of advanced antenna solutions to fulfill the corresponding massive traffic volume and substantial data rate demands seems necessary. Although intensive research is ongoing in outlining 5G network requirements and investigation of wireless channel environment from the system perspective, unfortunately the actual development of antennas and RF components for realization of this vision is lagging behind [1]–[3]. It is mainly attributed to the fundamental differences in propagation characteristics, path loss, and fabrication constraints exist for the wide range of high frequencies (namely 10 GHz-100 GHz) considered, yet not universally standardized and assigned, for future 5G mm-wave band communication applications [1]. There have been, however, some attempts to design antennas for 5G, mostly focused on cellphone applications as in [4]-[5]. Regarding base station antennas (BSA), probably due to more challenges and obstacles, limited study items can be found [6]-[7]. In addition to limited material available in the literature in this regard, another issue is that unfortunately most of them lack a certain degree of clarification

of goals and justification of choice of parameters from the point of view of the network in which the device would be deployed.

To obliterate these shortcomings, this work is focused on design and implementation of new antenna architectures as follows.

A beam scanning leaky-wave antenna (LWA) at 15 GHz

A broadside circularly polarized traveling wave array (CP TWA) at 26 GHz

Although throughout this manuscript, the design process is described in detail from the antenna and radiation perspective, we tried to keep the motive focused on future application of this in 5G BSA, hence our choice of parameters and configuration is done so as to accomplish the best compromise between electromagnetic (EM) performance, possible realization in current technology and also success in terms of network expectations. However, since application-based allocation of 5G frequency bands is yet to be formally identified in the world radio conference (WRC) 2018-2019, the material presented here should be considered as what is found most relevant to 5G network characteristics, drawn from the most recent literature in the area.

1.2 Advanced Aspects of Proposed Antenna Architectures

In this work, we propose

First, a novel *15 GHz double vertically-stacked substrate integrated waveguide leaky-wave antenna (SIW LWA) subarray* and investigate the implementation of such a subarray structure as a low complexity approach to build a cylindrical array suitable for flat-topped coverage of the entire azimuth plane. Our choice of 15 GHz band is inspired by Ericsson's recent 5G campaign revealing to achieve over 4.5 Gb/s data rate in this spectrum [8]. The proposed subarray antenna provides many unique features.

Second, a narrow-wall waveguide slot linear antenna array with circularly polarized radiation at 26 GHz. This structure is designed with multi-layer printed circuit board (PCB) in SIW technology. Two different feeding systems are investigated. The final configuration can be used to implement a low-profile planar antenna for 5G base stations as the narrow-

wall slots permit the adjacent waveguides to have inter-element spacing $< \lambda_o/2$, leading to a design which will also allow for grating-lobe free wide-angle beam scanning.

The following is the list of some of the key features of the above designs.

1.2.1 SIW structure

The SIW structure is appealing due to features such as having low loss, and high power handling capabilities that will come in handy since the antennas are supposed to work at a moderately high frequency band where propagation and conductor losses are notoriously high [2]-[4] not to mention its easy integration with planar structures which would make fabrication process simple and cost effective [9]–[12].

1.2.2 Leaky-wave antenna

The choice of the leaky-wave for the 1st design is due to its inherent beam scanning property with variation of frequency [12]–[19].This is advantageous from two different perspectives. First, it will eliminate the need for large and complicated electric circuitry for phase shifting purposes usually required in counterpart structures such as phase arrays. Secondly this frequency-scanning of elevation-beam will reduce the complexity of downtilt mechanisms, required for most sector antennas, and thus saving the network in terms of latency. This is due to the fact that the time scale upon which the downtilt process is carried out can be very slow whereas the speed of the analogue beamforming is much faster [1]. However, in wideband applications, frequency beam scanning is problematic due to the beam squint phenomenon and a fixed-frequency beam steering is more desirable. In regards with this issue, leaky-wave antenna arrays are more suitable for vertical sectorization of service area and will benefit the network in terms of size and cost reduction as they eliminate the need for multiple antennas for zone sectorization.

1.2.3 Slot antenna

The choice of slot antenna with broadside beam for our 2nd design is beneficial for the following reasons. First, to avoid intrinsic reduction in aperture efficiency caused by tilted beams according to the following formula [20]

$$\eta = \frac{A_{eff}}{A_{ph}} cos\theta_{rad} \qquad (1\text{-}1)$$

where η is the aperture efficiency and $A_{eff}\ and\ A_{ph}$ are the effective and physical aperture and θ_{rad} is the beam tilt relative to broadside. This is of particular importance for point-to-point high speed communication systems and land mobile platforms where high aperture efficiencies and broadside beam are required which will bring us to the second, point. Unlike lens and reflector antennas, that cannot be realized in planar configuration due to their need for a focal point, and printed microstrip arrays which have significant feeding loss especially when the antenna aperture is large, narrow-wall slot antennas can be used to develop low profile planar antennas with very low feeding loss, which are perfect for high gain applications [21].

1.2.4 Subarray

Another notable feature of our 1st design, is that each vertically-stacked subarray is composed of two 1D SIW LWA with separate dynamically-controllable illumination spots in the azimuth, which will make the exploitation of spatial domain possible, even when the antenna subarray is not used in an array configuration. The spatial re-use provided by each subarray, will increase spectrum efficiency which will in turn result in traffic capacity enhancement for a given spectrum [1]. When used in an array configuration, it also helps to achieve a good-all-around performance in the horizontal plane. Historically speaking, most literature in the area of LWA is mainly devoted to the radiation obtained in the leaky-wave fashion, neglecting the pattern features in the azimuth (see [19] , [22] and [23]). Here we attempted to obtain a more controlled radiation pattern in the azimuth plane by introducing spatial diversity in the proposed double layer subarray.

So, in addition to the above-mentioned network-related benefits of spatial exploitation, the main motive for employing more than one antenna in the subarray configuration is to equip our structure with azimuth beamforming in addition to the elevation beam-steering already possible through frequency scanning.

In particular, it is of interest to study ways to extend LWAs' capabilities to accomplish flexible control of beams in both principal planes. Since there exist many

applications, such as hybrid beamforming in BSA [3] in which 2D beamforming in the level of subarray is essential. In such architectures, analogue beamforming in subarray level compensates for the path loss at high frequencies, while digital beamforming in array level provides the opportunity to implement advanced multi-antenna techniques such as multi-beam MIMO [1]-[2] and [6]-[7].

1.2.5 Circular polarization

One important characteristic of our 2nd proposed antenna is the realization of CP radiation especially with narrow-wall slots. This is done in anticipation of various motions experienced by mobile terminal antennas in real 5G scenarios which will result in polarization mismatch. Having CP antennas on both base stations and mobile terminals helps to effectively reduce polarization mismatch losses and increase the quality of signal [24].

1.2.6 Flat-topped beam

Another remarkable feature of our 1st design is that we can obtain flat-topped beam in the azimuth plane. This will result in an improved performance with regards to link budget since flat-topped beams tend to experience lower bit error rate (BER) and keep higher signal to noise ratio (SNR) [25].

1.3 Research Objectives and Thesis Outline

The main goal of this project is to provide antenna solutions for 5G applications. Through the project, we adopt different procedures and configurations to tackle the challenges related to the development of high gain directive beam antennas in a low-cost low-profile technology that offer higher integration with planar circuitry.

This thesis is organized as follows:

Chapter 2 is focused on literature review for various beam scanning antennas. Main beam scanning mechanisms are introduced along with some examples to better clarify and highlight advantage and disadvantage of each category. In the end results of some recent publications are investigated and compared.

Chapter 3 presents a novel double-layered vertically-stacked substrate integrated waveguide leaky-wave antenna (SIW LWA). An array of vias on the narrow wall, produces leakage through excitation of TE10 fast-wave mode of the waveguide. Attenuation and phase constants of the leaky mode are controlled independently to obtain desired pattern in the elevation. In the azimuth, top and bottom layers radiate independently, producing symmetrically located beams on both sides of broadside. In addition to frequency beam-steering in the elevation plane, the proposed topology also offers flexibility for multi-spot illumination of the azimuth plane with flat-topped beams at every $\boldsymbol{\varphi}-$ cut through excitation of each layer separately or both antennas simultaneously. A 15 GHz prototype has been fabricated and tested. Measured results are in good agreement with those of simulations.

Chapter 4 is a brief introduction to slot arrays and tries to unfold general guidelines for the choice of shape, orientation and relative placement of slots in order to achieve desired radiation patterns and polarizations from a linear slot array. Two main categories of slot arrays namely, a resonant array and a traveling wave slot array are discussed which will build the foundation for the next chapter where the CP narrow-wall slot array is proposed. Difference between hollow waveguide and dielectric loaded waveguide arrays are explained through visualization based on dispersion diagrams. Advantages, disadvantages and design challenges in each environment are listed. This will direct reader to choose the right technology for antenna realization to better serve the design requirement for a slot array at hand.

Chapter 5 addresses design methodology for the proposed 13 element narrow-wall waveguide slotted linear antenna at 26 GHz. Very little material can be found in the literature for *circularly polarized narrow-wall* slots. The design of CP antennas is mostly limited to broad wall of the waveguide where there is enough space for offset perpendicular slot pairs or cross slots to produce CP. Other efforts use only one tilted slot per unit cell, therefore CP is not accessible in the unit cell level but rather in the array level. To produce CP, these structures rely on having two adjacent linear slot arrays with opposite slot inclinations, fed 90 out of phase at the input port. Compared to structures where CP is

available at the unit cell level, these structures due to their need for phase shifters are not very efficient especially for low-cost mass production solutions.

Due to little design approach information in the literature for *circularly polarized narrow-wall* slot arrays, parameter studies are carried out to first find a unit cell capable of producing CP with good return loss at the broadside. Then a 13-element linear array is designed based on these unit cells capable of achieving 14.5 dB left hand circular polarization (LHCP) gain and 1.5 dB axial ratio (AR) on the broadside. A stripline-CPW transition used for feeding is designed separately. Once the feeding section is connected, an optimization is carried out which proved to be very effective for the entire antenna-feed system to accomplish excellent return loss while producing good axial ratio and gain at the broadside.

Finally, Chapter 6 provides conclusions of this research and suggestions for future work.

Chapter 2

2 Literature Review

2.1 Introduction

SIW-based LWAs depending on their beam scanning ability and radiation mechanism can be categorized into two groups as follows.

2.2 Different Beam Scanning Capabilities

SIW-based LWAs reveal a variety of interesting features regarding their beam scanning ability. This is due to numerous radiation mechanisms that could be adopted in a large variety of possible geometries. For example, the scanning range for antennas in [19], and [23] and [30]-[31] covers from broadside to forward endfire while others can provide radiation from backward endfire through broadside directions [17], [32] and [33]. There is also another group realized in composite right/left-handed (CRLH) metamaterial technology like the ones proposed in [13]–[16], and [34] which offer full scanning from the backward to the forward direction.

2.3 Different Radiation Mechanisms

From another point of view SIW LWAs can be distinguished by their different leakage mechanisms. For example in the *transverse slot LWAs*, the reason for radiation is due to the well-known fact that the longitudinal currents are cut by transverse slots (usually on the broad wall of the waveguide) [9]. Some others take advantage of large spacing between vias to achieve radiation from side walls of the SIW [12].These are examples of *periodic SIW LWAs* for which the fundamental mode is a slow wave and does not radiate so radiation is obtained using its first space harmonic. There is also another type of LWA in SIW technology that radiates similar to a conventional *microstrip leaky-wave antenna* or *half mode SIW LWA* discussed in [11], and [35]–[37] where leakage occurs from the equivalent longitudinal magnetic current created at the open edges of microstrip line. In such structures the fundamental mode is bound and, the first higher order mode must be excited to take care of the radiation. An SIW LWA resembles this, is the one proposed in [22] and will also be discussed at the end of this chapter. In this architecture, although the array of sparsely located vias is creating a partially reflective surface (PRS) at the lateral edge of the SIW and the structure is becoming somewhat periodic but still the fundamental TE10 mode of the waveguide could act as a fast leaky-mode causing the radiation to occur. The reason for this is the extension of substrate beyond the PRS wall of the SIW which makes it more like a conventional microstrip leaky-wave antenna (MLWA).

Depending on the application at hand, one could choose from numerous available varieties. In the following some examples from each group are discussed briefly.

2.4 Printed Leaky-Wave Antenna Based on Sinusoidally-Modulated Reactance Surface (SMRS)

As shown in Fig. 2-1 this structure is composed of an array of modulated metallic strips over a grounded dielectric slab. This antenna is capable of scanning in the first quadrant. A scanning range of 17^{o} per 1 GHz is reported however beam shape has been deteriorated over the scanning range. The antenna is planar and simple-to-feed and the

modulation factor could be selected such that both attenuation and phase constants could be controlled independently.

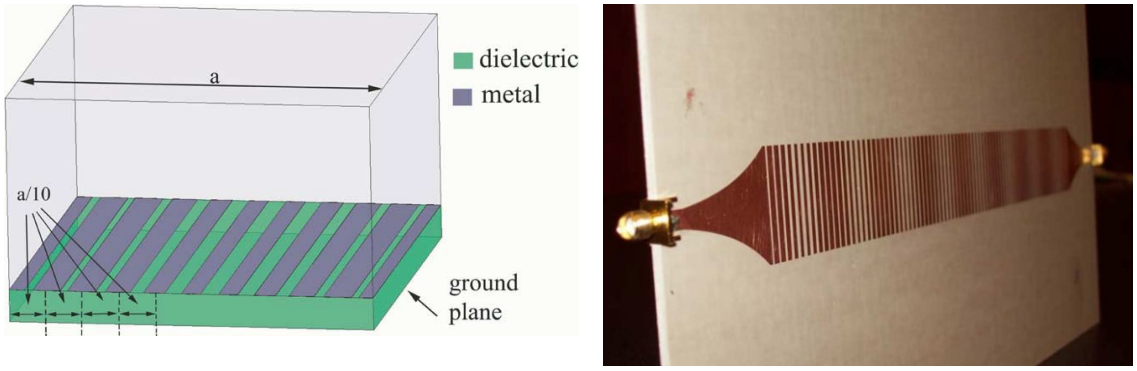

(a) (b)

Fig. 2-1 (a) Unit cell of SMRS, (b) Photograph of fabricated antenna with eight series unit cells. Courtesy of [23]

However, realization of the desired modulated surface impedance is not an easy task. Even for small values of modulation, a wide range of impedances should be covered for the structure to have the main beam at a specific location. This will limit the application of such architecture. Also due to its periodic nature, this architecture suffers from excitation of higher order harmonics leading to appearance of unwanted lobes, which limits the bandwidth of the antenna and reduces its efficiency.

2.5 CPW Based Slot Leaky-Wave Antenna

This planar structure could be treated as a uniform leaky-wave antenna for which fundamental harmonic ($n = 0$) is responsible for radiation so essentially there is no need for complex feeding to suppress the fundamental mode of the guide, as is usual for microstrip leaky-wave antennas. Plus with $n = 0$ being the leaky mode, the scanning range is limited to the forward quadrant (7^o per 1 GHz as reported in [19]). The antenna configuration can be seen in Fig. 2-2.

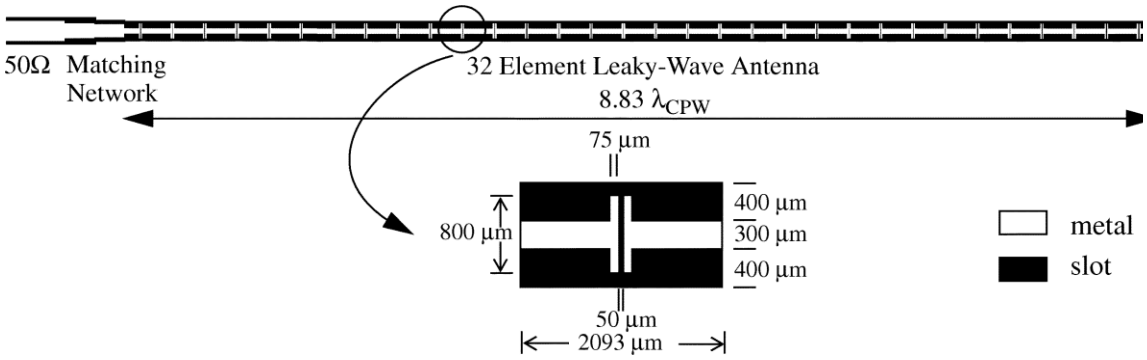

Fig. 2-2 CPW based LWA configuration. Courtesy of [19]

One drawback of this structure is its bidirectional pattern since the slot radiator by nature is a bidirectional radiator. To suppress the back lobe, either a cavity or ground plane must be placed to the back of the slot. However spurious resonances may result in the former approach, reducing the bandwidth and in the latter approach, parasitic TEM wave could be created between ground and slot. Some other more complex techniques such as using electromagnetic bandgap (EBG) structures or phase cancellation methods are also suggested in the literature.

2.6 Half Mode Substrate Integrated Waveguide (HMSIW) LWA

Wide bandwidth and bidirectional pattern are reported for the simple-to-feed planar antenna of Fig. 2-3. For millimeter-wave applications this is more qualified than half-width MLWA due to lower loss it experiences, owing to the SIW configuration. It is also advantageous since it occupies less space and has a more compact size compared to conventional SIW LWA.

However, it is not capable of producing a unidirectional beam as preferred by most applications. The bidirectional pattern is due to the emergence of an unwanted lobe happening for small value of substrate thickness. Beam squint of 9^o over 1.5 GHz is reported. This could be used in road vehicle communication applications since the quasi-omni-directional pattern leads to uniform signal reception

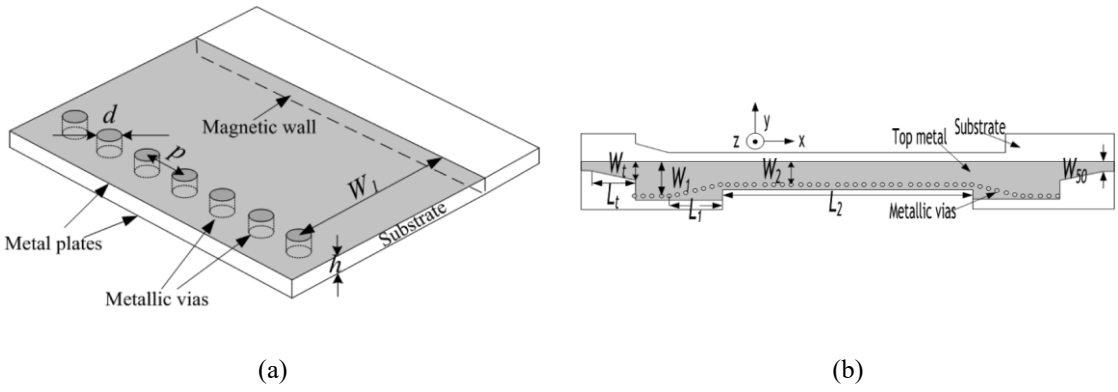

(a) (b)

Fig. 2-3 Structure of HMSIW (b) HMSIW LWA configuration. Courtesy of [11]

2.7 Periodic LWA in Hybrid Waveguide-Planar Technology

This class of antennas is exemplified by two different configurations as seen below. In Fig. 2-4 TE01 mode is responsible for radiation and scanning range from backfire to broadside can be accomplished. The main drawback of this structure however is the inability to independently control leakage and phase constants of the leaky mode. It is due to the fact that, although *Q/P* (relative slot length) can be used to control the leakage rate, but this will affect the broadside bandgap and also the main beam pointing angle.

To remedy this situation the slot-loaded structure in Fig. 2-5 has been introduced where slots are located asymmetrically with respect to lateral walls. The other modification compared to Fig. 2-4 is that the slot widths do not cover the entire width of the waveguide ($W < a$). The latter modification is done to keep radiation, horizontally-polarized as in Fig. 2-4. This fact is explained in Fig. 2-5 where it can be seen how the symmetrically located slots, make TE10 mode, non-radiative and radiation occurs if the asymmetry is introduced in the structure. Therefore, by controlling the level of asymmetry one can control the leakage rate of the TE10 mode. Moreover, *P* is chosen to determine the operating frequency whereas the slot length *Q* can be varied to obtain minimum possible bandgap at broadside to achieve more continuous scanning feature from backward to forward quadrant. Therefore, this structure is superior to the one in Fig. 2-4 due to its ability for independent control of leakage and phase constant which also leads to more freedom in determination of scanning range.

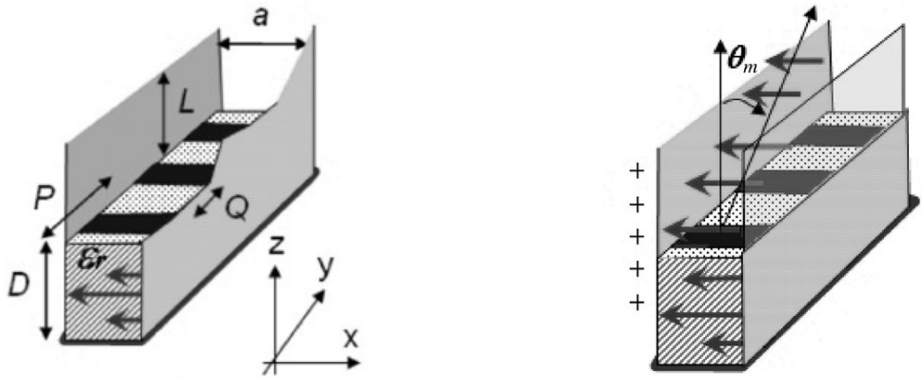

Fig. 2-4 (a) Dielectric-inset laterally-shielded top-open LWA, (b) Leaky TE01 mode in symmetrical structure. Courtesy of [17]

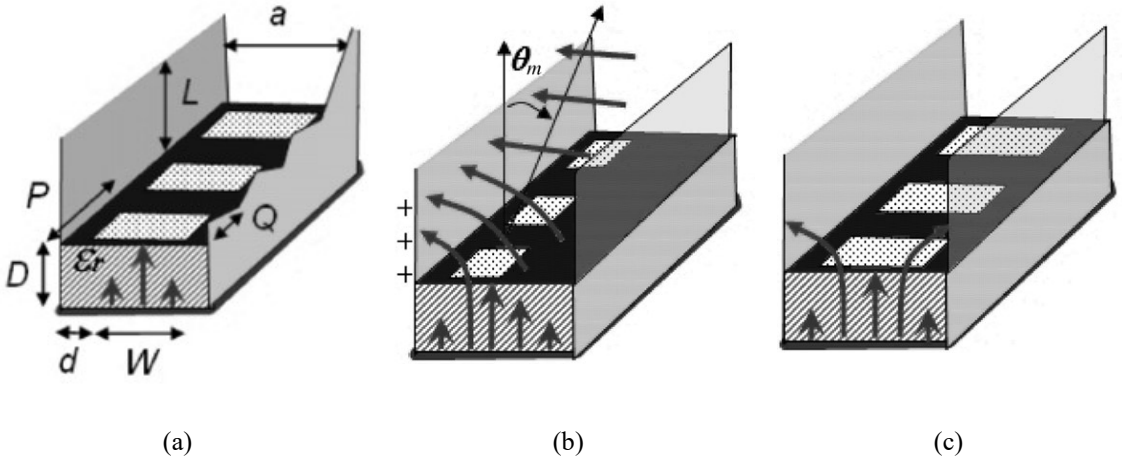

Fig. 2-5 (a) Slot-loaded laterally-shielded top-open LWA, (b) Leaky TE10 mode in asymmetrical structure, (c) Non-radiative TE10 mode in symmetrical structure. Courtesy of [17]

However, for all periodic structures, higher order harmonics could give rise to the emergence of unwanted lobes. Moreover, the reflected power from the end of the waveguide, due to the discontinuity, also leads to stronger power level for these lobes, which results in considerable loss of gain in the desired direction.

2.8 Periodic Half Width Microstrip LWA (HWMLWA)

As shown in Fig. 2-6 this structure consists of a series of half-width MLWA radiating the slow-wave along the edges. The non-radiating outside walls are shorted using metallic vias so each half-width section performs in the first higher order mode. Special consideration should be taken on the feed, so it guards against the fundamental mode of the guide. However, since the entire structure is periodic, leakage through $n = -1$ harmonic could create wide scanning range from backward to forward. An actual scanning range of -60^o to 60^o is reported for variation of frequency in the range of 4.2 GHz to 8.9 GHz. This structure has the advantage of simpler construction over the composite right/left handed (CRLH) configurations.

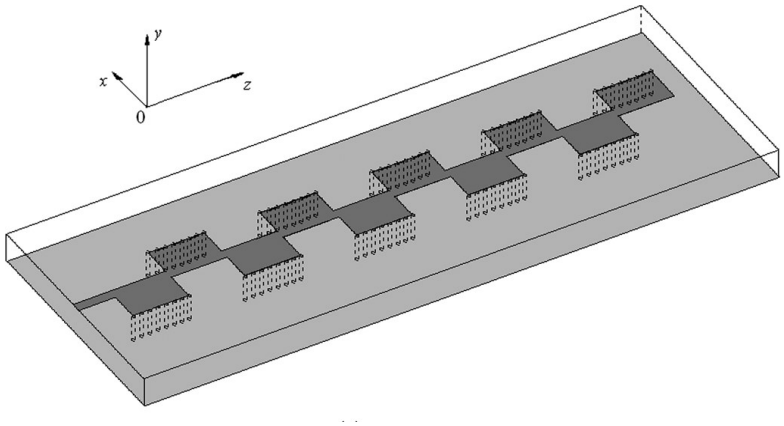

Fig. 2-6 Periodic half-width MLWA with forward to backward scanning capability. Courtesy of [15]

However compared to the asymmetric waveguide structure of [17], the half-width MLWA suffers from wider stop-band around the broadside.

2.9 Composite Right/Left-Handed (CRLH) SIW LWA

The radiating elements are interdigital slots etched on the top surface and ground of the waveguide as seen in Fig. 2-7. Backward to forward scanning feature is obtained through CRLH behavior of the slots. The left-handed behavior is achieved through combination of series capacitance introduced by interdigital slots, and the shunt inductance of SIW vias. One main benefit of this class of antennas is their miniaturized size.

Miniaturization is accomplished by reducing the width through HWSIW architectures and also by enforcing the below cut-off frequency operation.

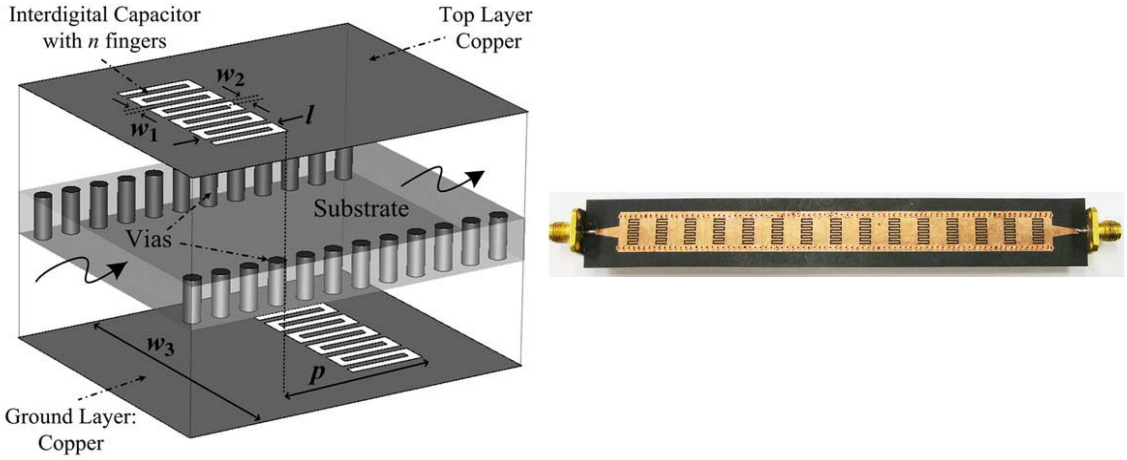

(a) (b)

Fig. 2-7 CRLH SIW LWA. (a) Double-sided radiating element, (b) Antenna configuration. Courtesy of [16]

Generally speaking, the antennas in this category suffer from narrow bandwidths not to mention their multi-layer PCB fabrication and complicated realization.

2.10 Planar SIW Leaky-Wave Antenna

This structure is created by replacing one of the narrow walls of the conventional SIW with a partially reflective surface (PRS) as illustrated in Fig. 2-8. To create the PRS wall a set of sparsely located circular vias has been used. The PRS wall is creating an inductive impedance according to its equivalent circuit given in [38], thus exciting the TE leaky-wave inside the antenna structure. One of the remarkable features is that independent control of leakage rate and beam angle can easily be achieved by modification of periodicity and width of the guide. This will guarantee that the antenna maintains high efficiency while scanning.

Since our proposed subarray in the next chapter is inspired by this configuration, a more detailed investigation of this antenna is presented here. This is done by analyzing equivalent circuit theory and discussing results of parametric studies obtained in [38]–[40].

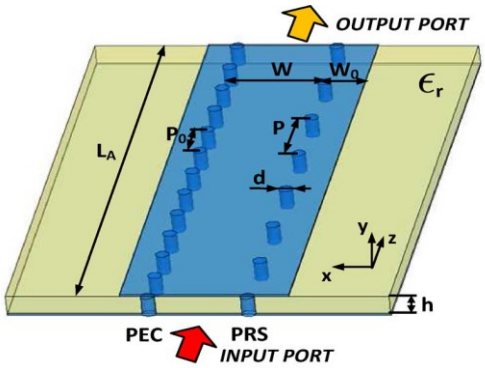

Fig. 2-8 SIW LWA Courtesy of [38]

2.10.1 Parametric dispersion curves

To gain more insight into the radiation mechanism of the structure, here some parametric dispersion curves are given and discussed. The analysis in this section is mostly based on the transverse equivalent network (TEN) and precise modeling of the inductive PRS wall of the waveguide. Transverse resonance method (TRM) is then used to find the leaky-wave wavenumber.

2.10.2 Transverse equivalent network

Fig. 2-9 shows the proposed TEN for the antenna in Fig. 2-8. Transmission line sections of length W and W_o are modeled with characteristic impedances of Z_o, where Z_o is the wave impedance of the TE10 mode excited in the waveguide. To model the radiating discontinuity at the edge of the parallel plate waveguide, the radiating strip of width w_o is terminated with radiation impedance Z_{RAD}. A T-impedance network is also used to model inductance and capacitance values corresponding to the rows of vias on both sides of the SIW guide. X_a and X_b values can be obtained through graphs available in [39]. However, to find more accurate approximations these values are also obtained using full-wave simulations as explained below.

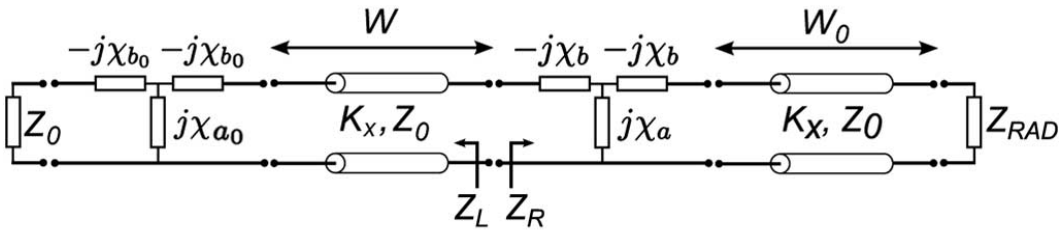

Fig. 2-9 Transverse equivalent network of Fig. 2-8. Courtesy of [40]

2.10.2.1 Accurate full-wave modeling of PRS wall

A more accurate estimation of X_a and X_b is available through electric field integral equation (EFIE) method. In this approach a TE-polarized wave is incident on the row of PRS posts as illustrated in Fig. 2-10, and then from its reflection coefficient ρ_P, the associated complex impedance is computed for a specific incidence angle θ_{INC} as follows.

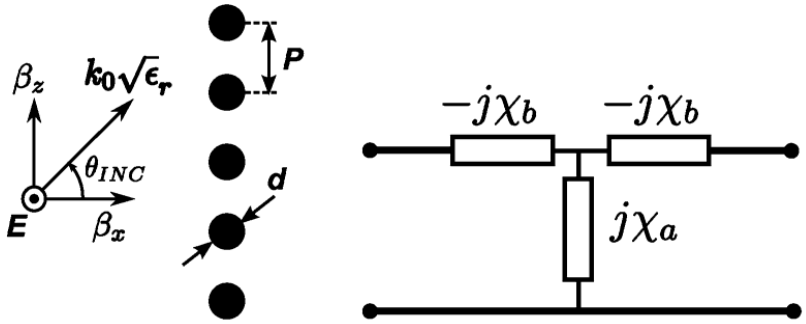

Fig. 2-10 T network describing TE-incidence on an array of metallic posts. Courtesy of [40]

$$\overline{Z_P}(P,\theta_{INC}) = \frac{Z_P}{Z_o} = \frac{1+\rho_P(P,\theta_{INC})}{1-\rho_P(P,\theta_{INC})} = \overline{R_P}(P,\theta_{INC}) + j\overline{X_P}(P,\theta_{INC}) \quad (2\text{-}1)$$

If we compare impedance of the T network, proposed by Fig. 2-10, to the one obtained above, X_a and X_b can be obtained from the real and imaginary parts $\overline{R_P}(P,\theta_{INC})$ and $\overline{X_P}(P,\theta_{INC})$ as below.

$$\overline{X_a}(P,\theta_{INC}) = \frac{X_a}{Z_o} = \sqrt{\bar{R}_P(P,\theta_{INC})\left[1+\left(\frac{\bar{X}_P(P,\theta_{INC})}{1-\bar{R}_P(P,\theta_{INC})}\right)^2\right]} \quad (2\text{-}2)$$

$$\overline{X_b}(P,\theta_{INC}) = \frac{X_b}{Z_o} = \bar{X}_a(P,\theta_{INC}) - \left(\frac{\bar{X}_P(P,\theta_{INC})}{1-\bar{R}_P(P,\theta_{INC})}\right) \quad (2\text{-}3)$$

Results are shown in Fig. 2-11 for $\theta_{INC} = 30^o$ from both methods explained above. It can be seen that from Marcuvitz approach [39], for small values of periodicity ($P < 3mm$ in this case), X_a is becoming negative, suggesting the PRS wall's impedance becoming capacitive which is not true. So, Marcuvitz model is not accurate for small values of periodicity.

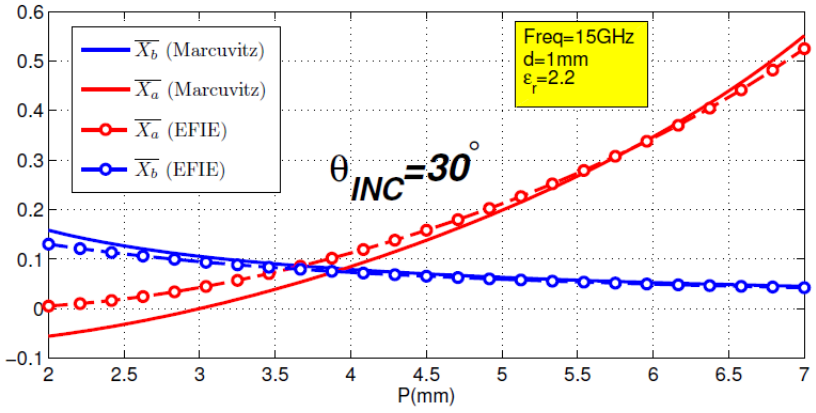

Fig. 2-11 Values of reactance from T network described in Fig. 2-10. Courtesy of [38]

From EFIE approach, behavior of reflection coefficient is depicted through Fig. 2-12. It can be seen that, the PRS wall is totally reflective for small values of P due to $|\rho_P| \cong 1$ and as distance between vias is expanded, the PRS wall is becoming more transparent as evident through $|\rho_P| < 1$ for upper range of P values. As stated before, PRS is inductive so phase of ρ_P is supposed to be positive. However, as we saw earlier, an exchange of behavior from inductive to capacitive is observed for small values of P.

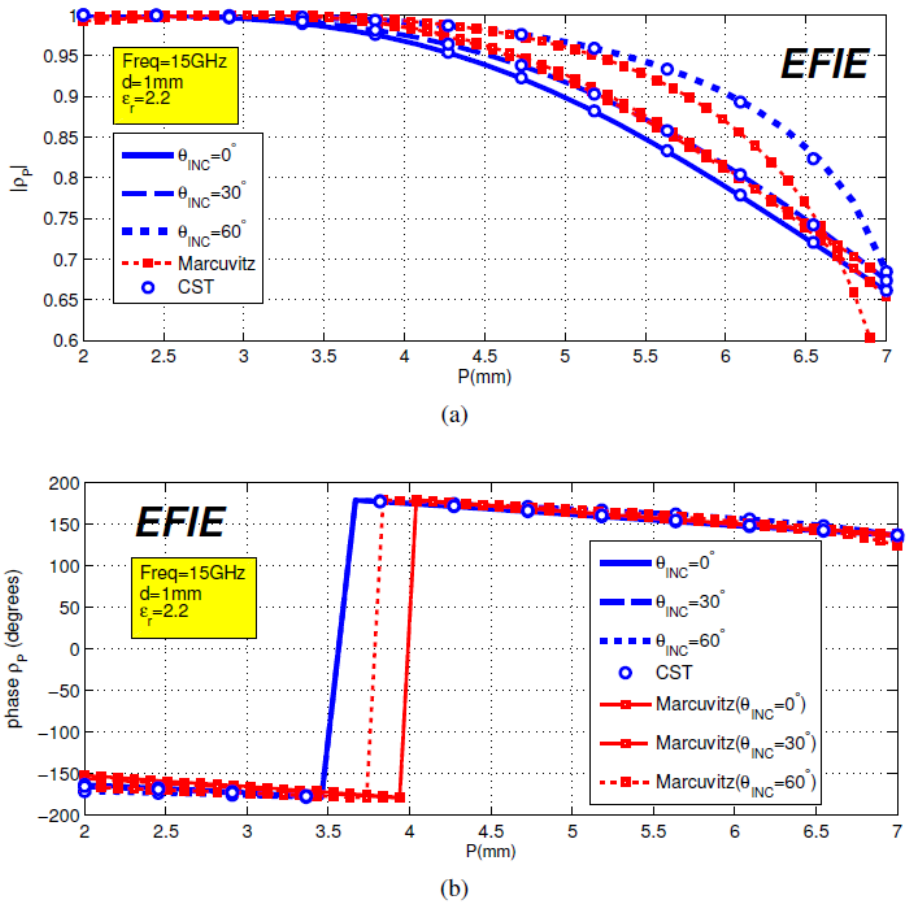

Fig. 2-12 Amplitude and phase of reflection coefficient from a TE-incident wave on an array metallic posts. Courtesy of [38]

2.10.2.2 Transverse resonant method

After finding an accurate model for the PRS wall, we can proceed to the calculation of leaky-wave wavenumber, using the TRM formulation as below.

$$Z_L(k_z) + Z_R(k_z) = 0 \qquad (2\text{-}4)$$

Z_L and Z_R are the impedances to the left and right of the reference plane as indicated in Fig. 2-9. The impedance of transmission line sections of length W and W_o are functions of Z_O and

$$Z_O(\theta_{INC}) = \frac{\omega\mu_o}{k_x(\theta_{INC})} \quad (2\text{-}5)$$

where transverse wavenumber k_x is related to the longitudinal wavenumber k_z as in

$$k_x(\theta_{INC}) = \sqrt{k_o^2\varepsilon_r - k_z^2(\theta_{INC})} \quad (2\text{-}6)$$

where k_z is given by

$$k_z(\theta_{INC}) = \beta_z(\theta_{INC}) - j\alpha \quad (2\text{-}7)$$

and

$$sin(\theta_{INC}) \approx \frac{\beta_z}{k_o\sqrt{\varepsilon_r}} \quad (2\text{-}8)$$

So, all the components of TEN can be represented as functions of $\beta_z(\theta_{INC})$ and α. The immediate conclusion is that the problem of finding leaky mode wavenumber, can be reduced to minimization of the equation (2-4) in the complex plane of $\beta_z - j\alpha$ at any given frequency and dimensions of LWA. Graphical representations of Fig. 2-13 show the normalized values of attenuation and phase constants. It is seen that good agreement between methods is obtained for larger values of periodicity *P* as was expected.

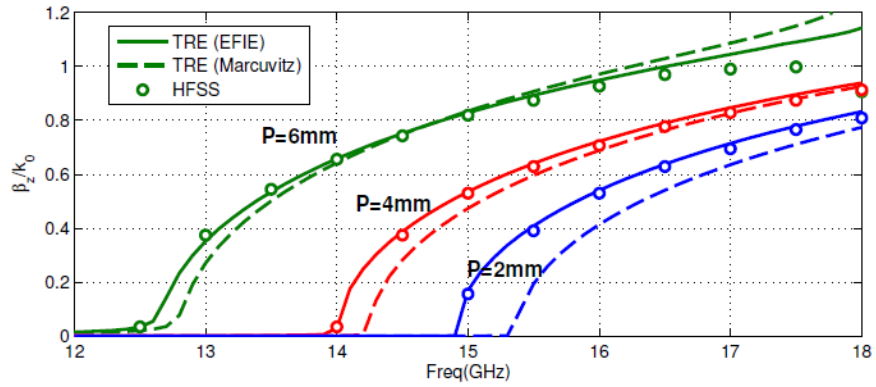

(a)

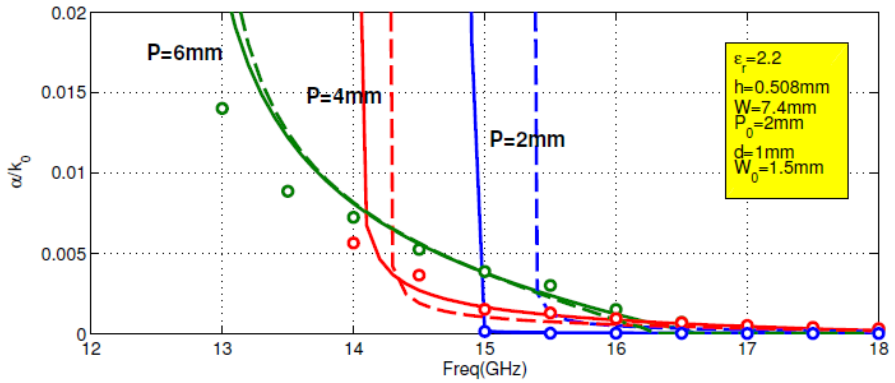

(b)

Fig. 2-13 (a) Normalized phase constant and (b) Normalized attenuation constant using TRM. Courtesy of [38]

2.10.3 Parametric study

First *W* is set such that the frequency of operation lies within the fast-wave region. Then *P* could be varied to obtain desired leakage rates as shown in Fig. 2-14. We also see how increasing *W* decreases the leakage rate, for a fixed value of periodicity *P*. This effect is attributed to the fact that cut-off frequency will shift to smaller values as *W* is raised. This will translate to less attenuation, since the given operating frequency is now further away from the cut-off.

Another explanation for this is by noting that waveguide cross section *W,* is mainly responsible for leaky-mode phase constant. So as seen in Fig. 2-15, at a fixed value of *P*,

an increase of W will make the beam to point at larger angles (θ_{rad} increases) closer to endfire, hence approaching the slow-wave region where leakage is almost zero.

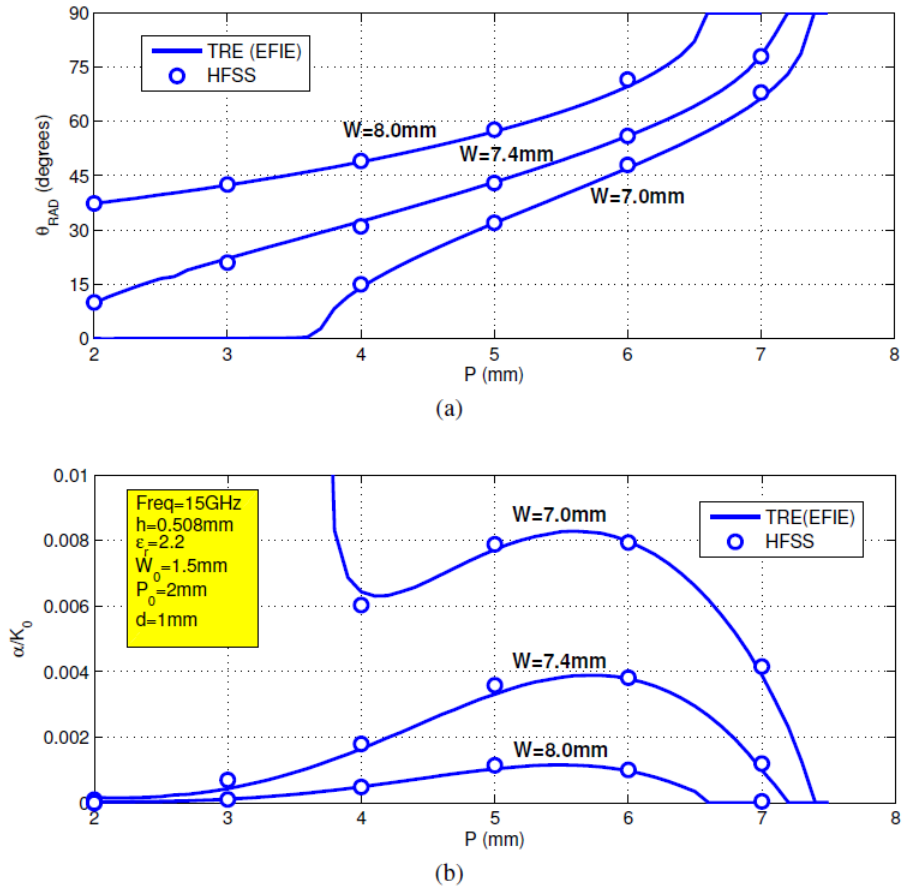

Fig. 2-14 (a) Change of main beam angle and (b) Change of leakage rate with variation of distance between posts. Courtesy of [38]

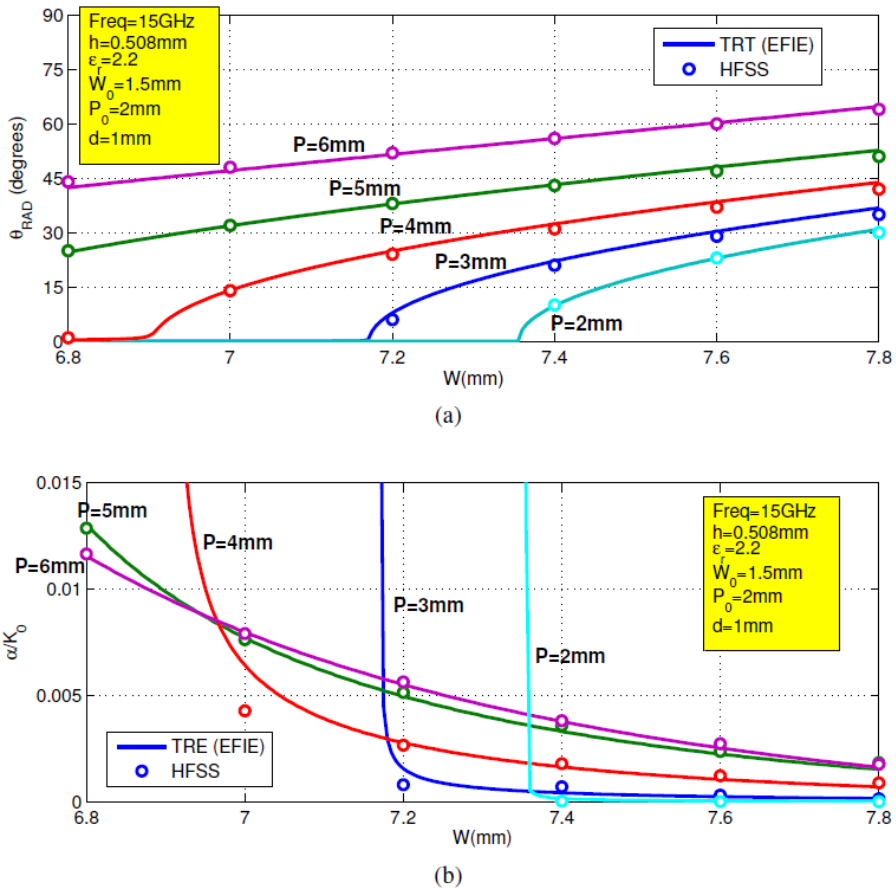

Fig. 2-15 (a) Change of main beam angle and (b) Change of leakage rate with variation of width of the guide. Courtesy of [38]

From the above plots, it is evident how simultaneous control of *W* and *P* can help to independently design the main beam pointing angle and its beamwidth.

2.11 Conclusion

Different types of Leaky-wave antennas are listed in Table. 2-1. As stated earlier, these antennas can be compared from different perspectives. Generally speaking, SIW LWA and MLWA are more favorable than waveguide structures due to their easy integration with the rest of the electric circuitry. However, one must cope with more difficult and costly metallization process for SIW vias or higher loss levels of microstrips

at higher frequency range. On the other hand, SIW LWA and MLWA have more straightforward feeding mechanisms.

From the radiation mechanism point of view, LWAs could be divided into two categories of uniform and periodic. In uniform structures the fundamental mode is the fast wave and radiates whereas in the periodic architectures usually the fundamental mode is bound to the surface and radiation happens by its first harmonic which is a slow-wave. While uniform structures can easily achieve sidelobe level (SLL) of less than -10 dB, periodic configurations, due to the array-factor theory, are limited to SLL ~ -13 dB unless tapering is performed which will result in more complicated design and fabrication process.

Regarding the scanning ability, LWAs are categorized in three different groups. Those with scanning range in forward quadrant, i.e. from broadside to forward endfire, are essentially the fast-wave uniform type antennas. The second group is identified by backward to broadside scanning range and the last category has full scanning range, i.e., from backward endfire to forward endfire. However most of the antennas in the last group suffer from an appearance of stopband around broadside which prevents continuous scanning. One solution to minimize this stopband is exemplified by composite right/left hand metamaterial structures. However, these are commonly narrowband and have complex configurations. There are also some examples of conventional periodic structures that could provide full range scanning. However, in the forward quadrant their beam-steering ability is limited by the emergence of an unwanted lobe due to the next higher order harmonic entering the radiation cone.

Another important criterion is the ability to independently control main beam angle and beamwidth. This is realized in variety of different technologies. This is normally advantageous since it offers design flexibility and allows for radiation efficiency to be optimized at a certain pointing angle for a given antenna length.

The above discussion leads to the conclusion that there are different tradeoffs that must be considered in design of LWA. However, given the numerous structures developed over the years and available fabrication technologies, one should be able to select the configuration that can best serve for the specific application at hand.

Table. 2-1 Summary of literature review on different types of LWA

Ref.	Frequency (GHz)	Scanning Range (degree)	Gain (dB)	Independent Ctrl. (α, β)	Unwanted Lobe	Simple Feed	Planar
Broadside to forward scanning							
[19] Grbic-Eleftheriades	25.5-33.5	$21^o\ to\ 78^o$	9.2	no	yes	yes	yes
[23] Patel-Grbic	9-11	$13^o\ to\ 48^o$	18.4	yes	yes	yes	yes
[11] Xu – K. Wu	26.5-28	$21^o\ to\ 30^o$	12	no	yes	yes	yes
[22] Ros-Goussetis	14.4-16.1	$20^o\ to\ 45^o$	10	yes	no	yes	yes
[18] Liu -Jackson	10.5-11.5	$30^o\ to\ 64^o$	7	no	no	yes	yes
Backward to forward scanning							
[15] Li -Long	4.2-8.9	$-60^o\ to\ 60^o$	7	no	no	no	yes
[16] Dong-Itoh	8.5-12.8	$-70^o\ to\ 60^o$	12	no	yes	yes	yes
[17] Tornero -Melcon	42-54.8	$-90^o\ to\ 30^o$	NA	yes	yes	yes	no
[41] Mehdipour-Eleftheriades	5.3-11	$-53^o\ to\ 65^o$	7	no	yes	yes	yes
Backward to broadside scanning							
[17] Tornero -Melcon	38.75-45	$-50^o to\ 0^o$	NA	no	yes	yes	no
[12] Xu - K. Wu	28-34	$-70^o to\ 0^o$	9.3	yes	yes	yes	yes
[42] Cheng-K. Wu	33-37	$-45.7^o\ to -27.1^o$	12	no	no	yes	yes

Chapter 3

3 Dual Layer SIW Leaky Wave Subarray

3.1 Introduction

In this chapter, inspired by the simple antenna introduced in [22] we have proposed a novel dual layer subarray configuration. It has combined many interesting features among those are taking advantage of leaky-wave frequency scanning ability in the elevation plane, providing three modes of operation, each generating a separate beam at a different direction, in the azimuth plane, plus the effective use of space through a double stacked configuration whilst keeping the antenna feed absolutely simple through a SIW-microstrip transition section. The whole antenna is passive and there is no need for phase shifters which keeps the costs to minimum along with better stability and easier and more reliable realization in PCB technology.

3.2 Design Procedure

3.2.1 Proposed two-element subarray

The vertically-stacked antennas of the module in Fig. 3-1(c), are each a 1D SIW LWA, as shown in Fig. 3-1(a) and (b). The substrate used for both layers is RT/duroid 5880

with $\varepsilon_r = 2.2$ and thickness 1.575 mm. A pair of input-output ports is assigned for each end of both LWAs making the proposed subarray of Fig. 3-1(c) a four-port structure. The performance of an individual 1D SIW LWA is given in the next section. Here, description of geometry along with the radiation property of the proposed structure of Fig. 3-1(c) in both principal planes, are discussed briefly.

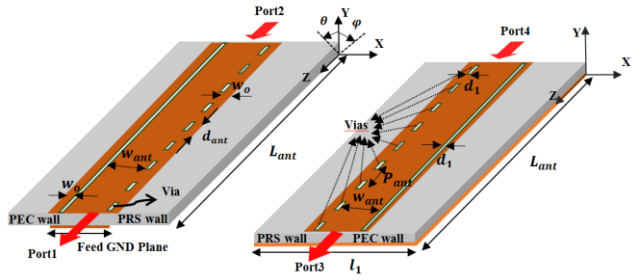

(a) (b)

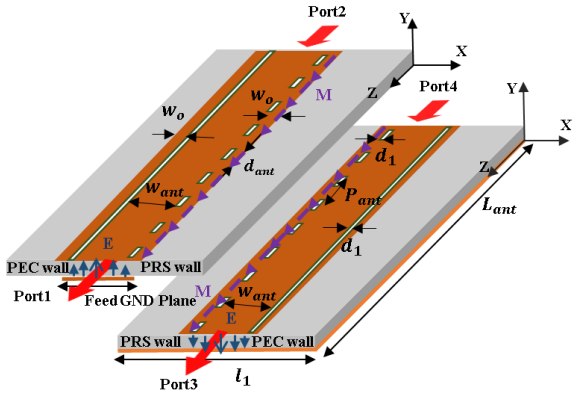

(c)

Fig. 3-1(a) Top antenna, (b) Bottom antenna, and (c) Proposed dual layer subarray. Radiation occurs from the co-directed longitudinal magnetic currents M, following Maxwell's equation, $M = \hat{n} \times E$ on the two opposite PRS walls. The PRS walls are created by arrays of rectangular vias on $x > 0$ and $x < 0$ on top and bottom SIW LWAs respectively. Dimensions are as, $P_{ant} = 4.5\ mm$, $w_{ant} = 7.3\ mm$, $w_o = 1.5\ mm$, $L_{ant} = 150\ mm$, and $l_1 = 28.9\ mm$. Substrate thickness for both antennas is 1.575 mm. Each rectangular via has dimensions of $d_1 = 0.4\ mm$ and $d_{ant} = 1\ mm$ and is located at $0.5\ w_{ant}$ away from the center of the waveguide as identified by the curved arrow in Fig. 3-1(a) and a set of dotted arrows in Fig. 3-1 (b).

The geometry of our proposed double stacked antenna is depicted in Fig. 3-2(a) where layer 3, shown in blue, and layer 1, shown in red are the antennas' common ground plane and the common radiating layer respectively. Fig. 3-2(b) illustrates the cross section where it is observed how the width of metal layer 1 is extended by w_o from each end. This width w_o of the edge microstrip section called radiating strip and, is used for tuning purposes to improve antenna radiation efficiency and co to cross polarization ratio.

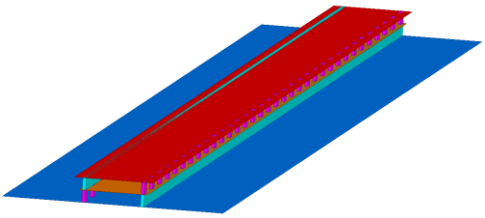

(a)

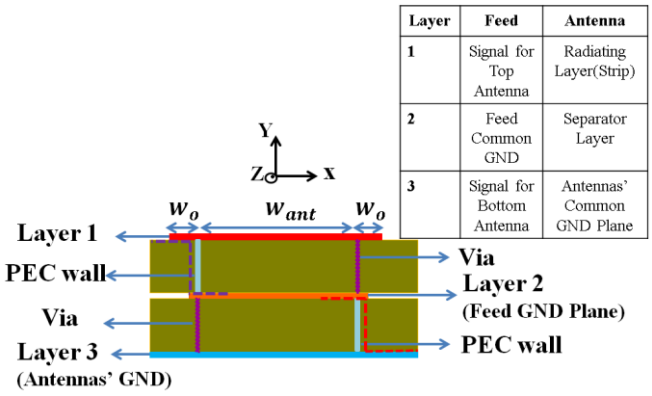

(b)

Fig. 3-2 Proposed dual layer subarray structure. (a) 3D view and (b) Cross sectional view. Red and purple dashed lines on the right and left handside of the picture designate steps in ground plane (layer 3) and radiating strip (layer 1) respectively.

From Fig. 3-2(b) it is also seen that the two SIWs, each act as an individual LWA, bonded together through a paper tape, are sharing the mid metal layer; layer 2. This mid layer separates the top and bottom waveguides and it has been cut immediately after the row of vias and the perfect electric conductor (PEC) wall on both ends. For fabrication

purposes the width of layer 2 is extended only $\lambda_o/20$ beyond vias and PEC walls as can be seen in Fig. 3-2(b).

To create the bottom LWA in our double stacked subarray of Fig. 3-2(b), the SIW line between metal layers 2 and 3 has been perturbed by introducing a PEC wall at $x > 0$ and an array of sparsely located rectangular vias at $x < 0$. In the same manner, the top SIW LWA, has been obtained by integrating a substrate between metal layers 1 and 2, however the PEC wall and the row of sparse rectangular vias are printed at opposite positions with respect to their counterparts in the bottom LWA. Fig. 3-2(b) illustrates this situation where for the top SIW LWA, PEC wall and the row of sparse rectangular vias are shown to be located at $x < 0$ and $x > 0$ respectively. Each of these sparsely located arrays of rectangular-shaped vias is creating a PRS wall at the lateral edge of the SIW, which will make the radiation possible.

As depicted in Fig. 3-2 (b) and also concluded from description of structures above, the apertures of the top SIW LWA are located between layers 1 and 2 at $x > 0$ whereas for the bottom antenna apertures are placed between layer 2 and layer 3 at $x < 0$. It is worth emphasizing that from the perspective of geometry and configuration, top and bottom antennas are distinctly different where the former has a continuous radiating strip but a step ground plane and the latter has a step radiating strip but a continuous ground plane. The step discontinuity is referred to the substrate thickness that forms a stepped distance between the apertures and their corresponding ground plane (layer 3) or radiating strip at either ends of layer 1.

As stated earlier, both antennas are sharing the mid metal layer; layer 2 which can be conveniently used as a common RF ground plane for the input ports, exciting top and bottom antennas. Hence electric fields excited in the top and bottom waveguides will have opposite directions as already illustrated in Fig. 3-1(c). These 180^o out of phase input ports will allow for adjusting the main beam direction in the azimuth plane (X-Y plane) as described below.

When port 2 gets excited, main beam is mainly produced by the PRS wall of the top antenna thus illuminating the 1st quarter in the azimuth plane, whereas switching the

excitation to port 4 will cause the leakage to occur from between the vias on the PRS wall of the bottom antenna, thereby illuminating the 2nd quarter in the azimuth plane. When both antennas are excited simultaneously, these two beams are merged into one perfect flat-topped beam pointed at broadside (y-axis) due to the complete far-field phase cancellation of oppositely-directed electric fields from each antenna as will be discussed later in this chapter.

The beam in the elevation plane (Y-Z plane) is produced due to the excitation of leaky mode and its pointing angle and beamwidth as will be described in the following section, remain quite constant and will not be affected by changing excitation at the input ports. So, in all three operating modes, i.e. radiation from antenna on top, radiation from the antenna on the bottom, or both simultaneously, this structure yields quite the same beam in the elevation plane. This condition is ideal since it means we will observe almost the same scanning behavior in all three modes as the frequency is changed.

The proposed double stacked structure inspired from the simple single layer antenna introduced in [38] however favorable geometrical modifications, as described above, have been made to the antenna structure so that to influence radiation pattern in the azimuth plane (azimuth beamforming) without affecting the pattern in the elevation plane and also cross-polarization level.

Our strategy to control over the azimuth plane pattern is proved to be straightforward but extremely effective and it includes applying the steps in the common ground plane (layer 3) and radiating layer (layer 1), stacking up two antennas, tuning key geometrical parameters such as l_1 and w_o , and also switching the excitation between input ports in order to obtain symmetrically-located and flat-topped radiation patterns in the azimuth plane. These aspects will be elaborated in the later sections.

3.2.1.1 Feeding mechanism

As stated earlier this is a four-port structure so four input ports must be assigned at both ends of each antenna. In practice this will be realize by SMA connectors attached to the edges of the PCBs. Since substrate thickness of each board is much smaller than the height of a standard SMA, it seems impossible to have two SMAs on top of each other (to

model ports 1 and 3 or ports 2 and 4 in Fig. 3-1(c)). To solve this issue the feedlines are bent towards opposite directions for the top and bottom antennas so their input ports though at the same ends along *z* axis but are located at a distance from each other along *x* (see Fig. 3-9). The SIW bends and tapering is done in such a way that the input feeding microstrip line is 50 ohm. The tapering is done in three stages. In the first step a SIW tapering is performed so the perturbed TE10 leaky mode is transformed into the TE10 mode in the waveguide with minimum leakage loss. So, the sparse array of vias in the antenna part of the design, is now changing to a closely located set of vias to prevent any possible leakage. The rest of tapering is carried out in the form of an SIW bend with its radius chosen so as to accommodate enough space along the *x* direction between SMA connectors for antennas on top and bottom. A metalized groove technique is used to create PEC walls for bends. It is worth to mention that both microstrip and CPW bends were also tested and SIW line was selected since it gave better performance in terms of insertion loss.

The last stage is the SIW-microstrip transition which is done first by a small tapering followed by a 50 ohm straight microstrip line. This transition has been chosen since the electric field profile for TE10 resembles that of quasi-TEM in the cross section of the guide as already discussed in many references like [10]. The last part transforms the TE10 mode of the waveguide into a quasi-TEM mode of the microstrip. The parameters of tapering and bends (depicted in Fig. 3-3) are optimized over the frequency band of interest and their final values are listed below Fig. 3-3. Note that both antennas are sharing the same ground plane in the mid layer as explained before, so the input ports are 180^o out of phase and this will allow for adjusting the main beam direction in the azimuth plane.

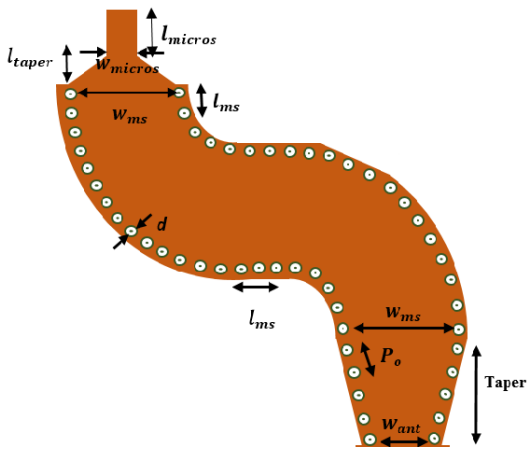

Fig. 3-3 Back to back SIW to microstrip transition (only half is shown) used to feed the antenna of Fig. 3-1. $l_{micros} = 6.75\ mm$, $l_{taper} = 1.7\ mm$, $w_{micros} = 4.7mm$, $l_{ms} = 3mm$, $w_{ms} = 9mm$, $d = 0.5mm$, $w_{ant} = 7.3mm$, $P_o = 1mm$, $Taper = 10mm$ *also bend radius is chosen to be 12mm.*

3.2.2 Single layer SIW leaky-wave antenna

In this section full-wave analysis of a single antenna similar to that of Fig. 3-1(b) is presented except that the PRS is assumed to be on the $x > 0$ wall and the PEC wall on the $x < 0$ lateral edge of the waveguide. As proved in [9] SIW guides show similar dispersion properties as in standard waveguides for TEn0 modes. Therefore, in the design of Fig. 3-1(b), perturbed-TE10 mode is the leaky mode and its complex wavenumber could be described as

$$k_z = \beta - j\alpha \tag{3-1}$$

where β is the propagation constant and determines the beam pointing angle in the elevation plane as

$$\sin(\theta_{rad}) = \frac{\beta}{k_0} \tag{3-2}$$

where θ is measured from the y-axis normal to the antenna. Since β is related to the guide cross section; w_{ant}, and w_{ant} itself determines the cutoff frequency, for the antenna to work at 15 GHz , w_{ant} has to be tuned to obtain the main beam at a desired angle for a

certain frequency according to (3-2). Having in mind that, this antenna will be used in a cylindrical configuration mounted on a pole at a base station and will be looking down on the cell site, the pointing angle has been chosen 50^o from the antenna broadside (40^o from the vertical pole) assuming excitation is placed at port 2. The period between the metallic posts on the lateral wall of the SIW controls the leakage rate and as a result will determine the attenuation constant or the imaginary part of the wavenumber. The PRS wall is designed to produce appropriate leakage for selected antenna length using (3-3) such that efficiency is better than 90%.

$$\eta = 1 - e^{-2\alpha L_{ant}} \tag{3-3}$$

In conformity with the most commonly used sector antennas where half power beamwidth, HPBW<15^o, the leaky beamwidth has been chosen ≈ 10^o using (3-4)

$$\Delta\theta \approx \frac{\lambda_o}{\cos(\theta_{rad}) L_{ant}} \tag{3-4}$$

The resulting pattern in the elevation plane can be seen in Fig. 3-4.

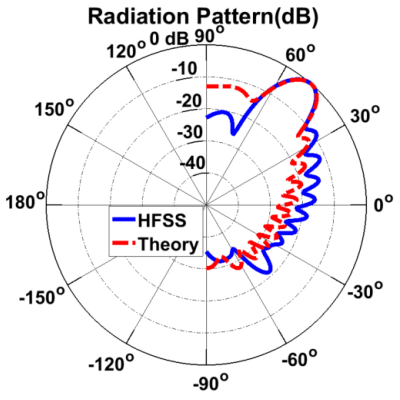

Fig. 3-4 Radiation pattern of single LWA in the elevation (Y-Z) plane.

Essentially an individual LWA of the form depicted in Fig. 3-1(a) or (b) can be treated as a linear array along the *z*-axis and an array factor as below will yield a good approximation of its pattern.

$$AF(\theta) = \sum_{n=1}^{N} I_o e^{-\alpha_z (n-1) P_{ant}} e^{jK_o (n-1) P_{ant} (sin\theta - sin\theta_{rad})} \quad (3\text{-}5)$$

Note that in our problem the elevation angle, θ is separated from the *y*-axis (as shown in Fig. 3-1(a)). The beam produced by (3-5) is also plotted in Fig. 3-4 indicating a good agreement between the theory and simulation. We however notice slight difference in the sidelobe levels. The main reasons for such discrepancies (also observed and discussed in [18] and [42]) are summarized in the following. 1) The assumption that array factor could *solely* furnish an accurate representation of the total pattern of the LWA is predicated on the ratio of periodicity over guided wavelength to be much smaller than unity. For $Pant/\lambda_g \approx 0.2$ in our case, the formula in (3-5), as expected, is only providing a *good approximation* of the pattern especially in the main beam area where the leaky-wave is mainly responsible for the radiation. 2) The array factor formula in (3-5) only considers the leaky-wave wave number whereas in the actual structure, surface-wave is also excited. This explains the difference in the sidelobe levels since for angles in directions away from the pointing angle, the effect of attenuation constant becomes more pronounced due to the factors such as excitation of surface-waves, and diffraction effects from finite ground plane. Also, appearance of lobes in the opposite direction in simulated pattern is a result of energy reflecting back due to the imperfect matching and discontinuity at the end of the antenna. Results from theory however do not follow the same behavior. This is due to the consideration of only forward wave in computation of leakage constant in formulation of array factor in (3-5).

Therefore, all these factors should be considered in order to characterize an accurate representation of the total pattern especially at angles far from the pointing direction.

Regarding the azimuth pattern of BSA, depending on different antenna alignments and cell shapes, the most frequently reported HPBW values are $30^o \sim 120^o$ [7]. Since the radiating equivalent magnetic current along the z-axis produces a fan-shaped beam in the azimuth, as seen in Fig. 3-5, it provides enough freedom in terms of choosing an optimum value for the horizontal aperture angle appropriate for different propagation environments; urban, suburban or rural areas. Results of Fig. 3-5, shows that maximum occurs at $\varphi = 30$ where φ is measured from the y-axis. The final optimum values of design parameters are summarized in Table. 3-1.

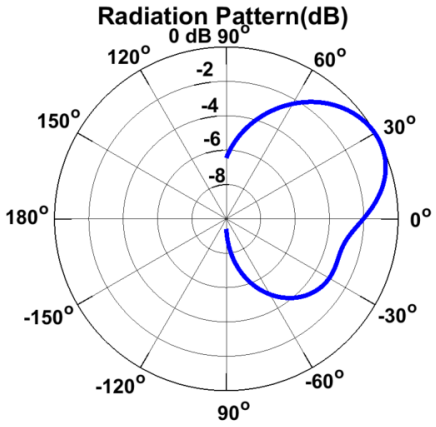

Fig. 3-5 Normalized gain of single LWA in the azimuth (X-Y) plane.

Table. 3-1 Dimensions for single leaky-wave antenna

Parameter	w_{ant}	P_{ant}	l_1	w_o	d_1	d_{ant}	L_{ant}
Dimension(mm)	7	4	23	1.5	0.1	1	130

3.3 2D Multi-Beam Subarray Performance

3.3.1 Simulation

As seen in the previous section, an SIW LWA was capable of producing a beam at 50^o and 30^o in the elevation and azimuth planes respectively. Now if two LWAs of this

kind are arranged in a double stacked array as shown in Fig. 3-1 then it is possible to realize a structure to control beams in both planes through variation of frequency and excitation at input ports. Since the cross section, geometry and number of vias in both antennas are the same, once excited at input ports, they produce the same propagation constant (β) along z, so the main beam pointing angle in the elevation plane which is a function of β will remain the same. It is also worth to mention that due to having the same length, both antennas will experience the same leakage constant which will yield same beamwidth in the elevation plane. Based on this, in the elevation plane, we expect quite the same performance from both antennas of the subarray. Both co-and cross-polarized patterns are shown in Fig. 3-6(a). Frequency scanning of the leaky-wave beam is also depicted in Fig. 3-6(b). Details of physical dimensions are listed below Fig. 3-1.

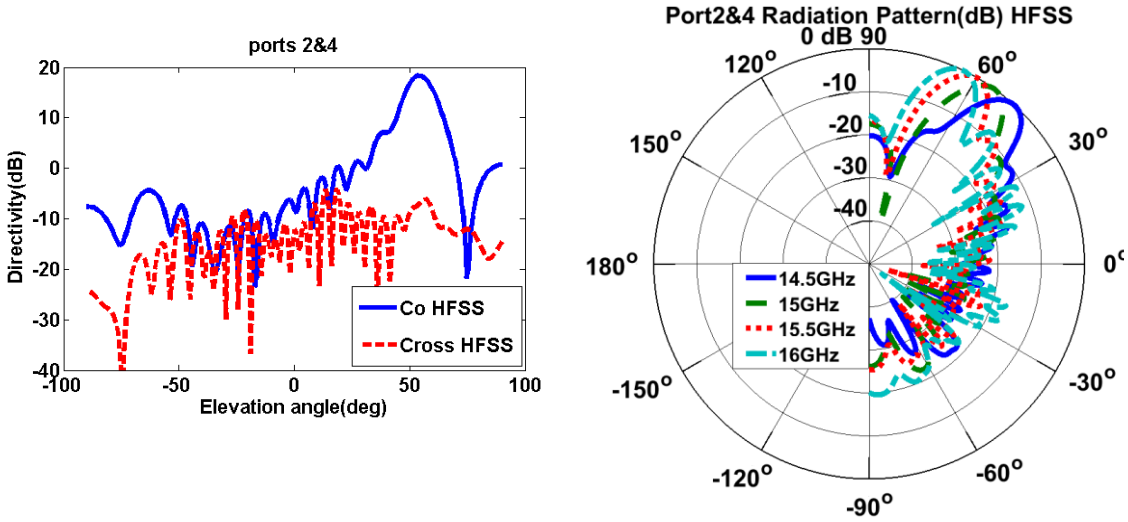

(a) (b)

Fig. 3-6(a) Comparison of simulated co- and cross-polarized components in the elevation plane for the double stacked antenna when both ports are excited. (b) Simulated frequency-scanning behavior in the elevation plane of double stacked antenna when both ports are excited.

From Fig. 3-6(b), it can be seen that the main beam angle scans about 10^o within 1 GHz. Variation of gain over this frequency range is about 0.7 dB as it falls from 17.65 dB

at 14.5 GHz to 16.93 dB at 16 GHz. The sidelobe level also remains below -10 dB for *almost* all angles over the scanning range.

One important parameter here, is l_1 or the substrate width along x-axis. This will determine the symmetry of (separate) azimuth beams (from each antenna) with respect to broadside. The more symmetrically located the main beams are with respect to $\varphi = 0^o$, the easier it is to achieve flat-topped main beam at broadside once both antennas are radiating simultaneously. So l_1 has been changed and phase of electric field at $\varphi = 0^o$ azimuth in the far field for top and bottom antenna has been recorded separately as φ_t and φ_b. The optimum value for l_1 is obtained when the far-field phases φ_t and φ_b completely cancel each other out at $\varphi = 0^o$. It would mean that once two antennas are excited simultaneously, the main beam in the azimuth plane appears at broadside. Graphical representation of such behavior is given by Fig. 3-7(a) and Fig. 3-7(b).

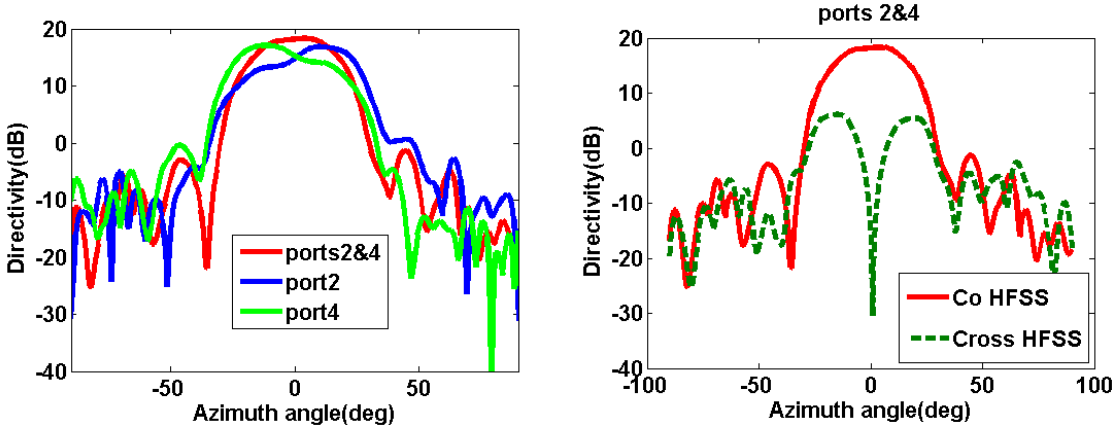

(a) (b)

Fig. 3-7 (a) Simulated azimuth plane patterns of double stacked antenna when top antenna is radiating, bottom antenna is radiating and finally when both antennas are radiating. (b) Comparison of simulated co- and cross-polarized components in the azimuth plane for double stacked antenna when both antennas are excited.

Simulated S-parameters are also shown in Fig. 3-8 where good isolation between channels is observed. In addition, $|S22| \leq -10$ dB over the entire frequency range, shows wideband matching performance. It is also seen that the value of $|S12|$ remains almost

below -10 dB for the desired scanning frequency range (up to 16 GHz) which is an indication of good radiation efficiency, since it would mean that the input power has considerably reduced due to the leakage, before arriving at the output port. For the higher frequency points in the band however, $|S12|$ increases due to the stronger and more dominant excitation of the surface-wave and the reduction in the radiation leakage as a result of approaching the slow-wave region.

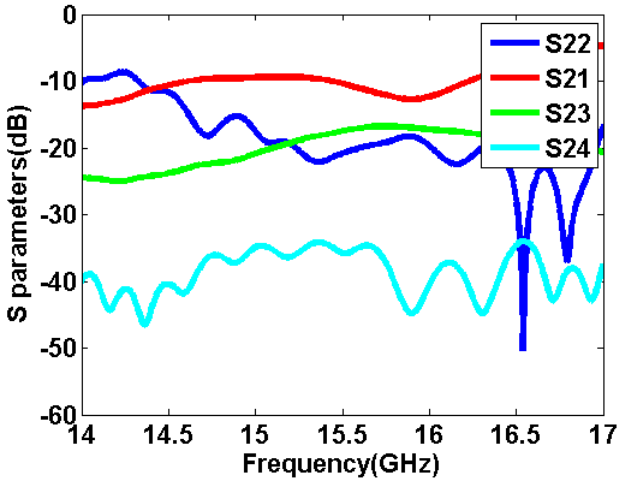

Fig. 3-8 Simulated S parameters for the antenna of Fig. 3-1.

3.3.2 Fabrication and measurement

PCB process has been used to fabricate each antenna on a single layer RT duroid 5880 of thickness 1.575 *mm* as shown in Fig. 3-9. Then both layers are bound together to implement the double layered configuration of Fig. 3-1.

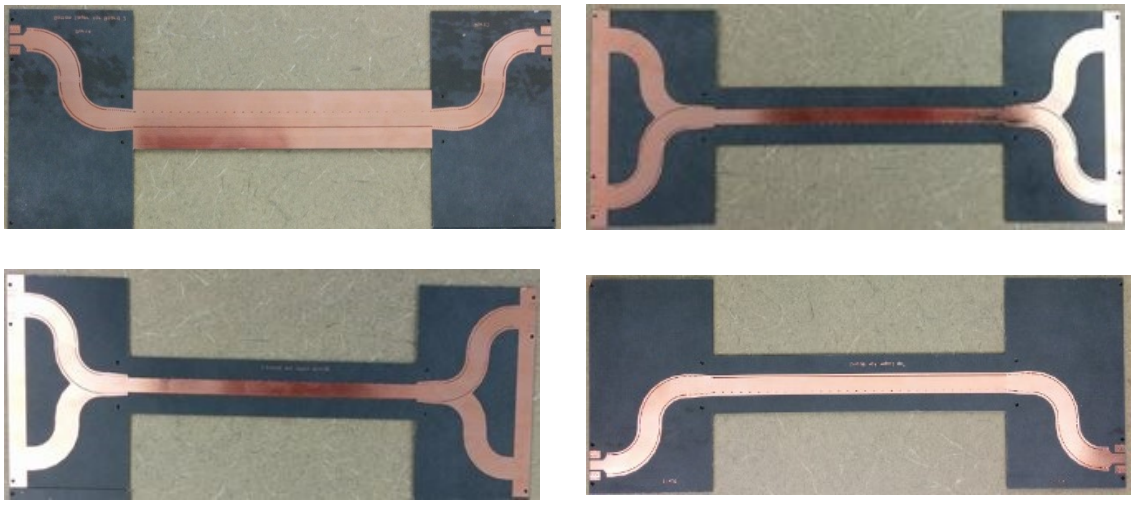

(a) (b)

Fig. 3-9 Photograph of the fabricated SIW antenna. (a) Separate layers of board 1, and (b) Separate layers of board 2.

Measured S-parameters are given in Fig. 3-10. For convenience simulated results are also presented to make comparison easier.

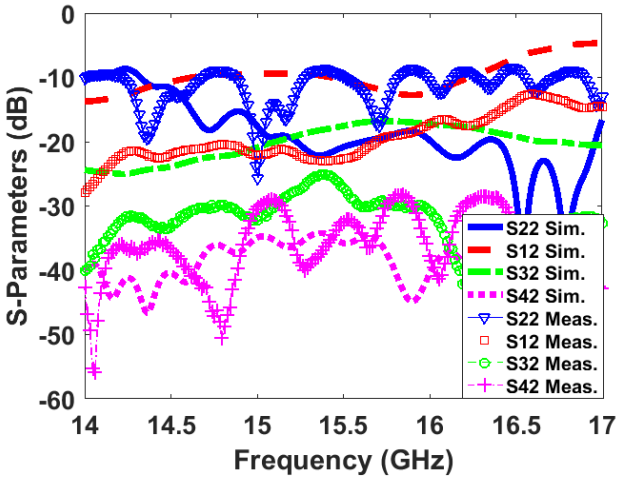

Fig. 3-10 Comparison of mearsured and simulated S parameters for the antenna of Fig. 3-1.

It is observed that $|S22|$ parameter is mostly better than -10 dB for the entire frequency range of 14 GHz ~ 17 GHz. Although at some frequency points inside the band of interest, its values shift up and reach -8.5 dB at the highest, we still observe an acceptable matching performance. A quick look at Fig. 3-10 also reveals a difference in the level of $|S22|$ between the simulation and measurement. Some of the reasons for such discrepancy

can be attributed to the loss from the SMA connectors which is not considered in the simulation and also the fabrication errors in PCB implementation, metallization of vias, and attaching the layers together. The isolation coefficients, $|S32|$ and $|S42|$ remain below -25 dB within 14 GHz ~ 17 GHz. Also note that the insertion loss is better than the simulation results. It is due to increased reflection and the added loss from dielectric and metallic parts in the measurement. The choice of the offset, i.e., the distance required between two SMA connectors, can be used to optimize the total length of bends and tapers to achieve better reflection and insertion loss factors.

The difference between level of S-parameters when port 2 (top antenna) is excited versus when port 4 (bottom antenna) is excited are given in Fig. 3-11.

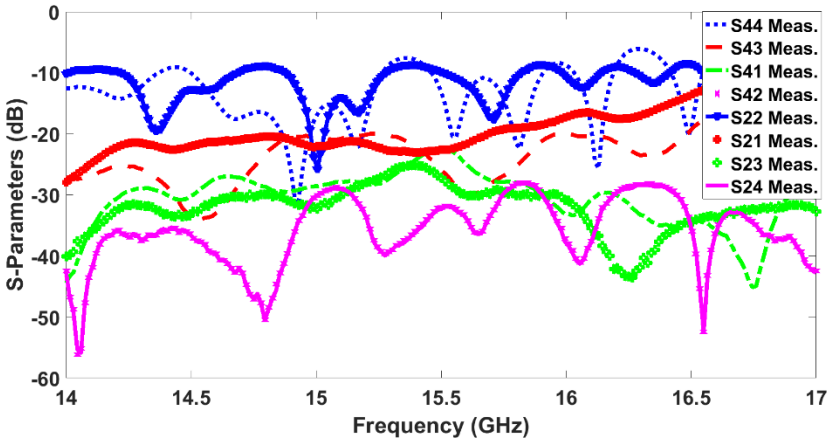

Fig. 3-11 Comparison between measured S-parameters of top and bottom antennas.

To measure the radiation performance a setup like the one shown in Fig. 3-12 has been used.

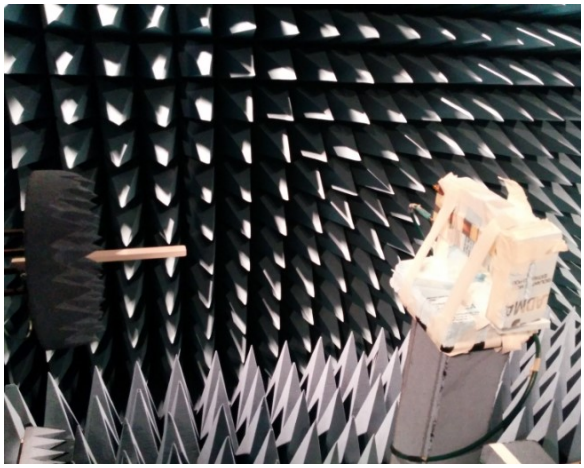

Fig. 3-12 Measurement setup to capture far-field radiation pattern.

Measured radiation patterns in the elevation plane compared to the simulation results are demonstrated in Fig. 3-13(a). It can be seen that the antenna is capable of covering the angular region of 10^o with its main directivity dropping less than 3 dB. Fig. 3-13(a) also indicates that the cross-polarization isolation is better than 14 dB for almost the entire range of angles. We also observe that the level of cross polarization in measurements is increased compared to simulations, owing to the diffraction effects of the finite ground plane which has a more serious impact in practice than it does in simulations.

To study beam-steering, radiation pattern in the elevation plane is tested at different frequencies and results are presented in Fig. 3-13(b). A quick look at this figure reveals that the measured patterns present higher sidelobe levels compared with the simulated ones in Fig. 3-6(b). It can be attributed to metallic parts of the azimuth stage not being perfectly covered during the test and also, possible blockage effects due to the coupler and its cables at some angles. Radiation from microstrip feed lines is also partially responsible for the increased sidelobe level. Since part of the leaky mode energy is reflecting back unwanted lobes in the opposite direction can be seen in both simulated and measured patterns. However, this effect is weaker in the simulations owing to better matching and lower values of $|S22|$ as already observed in Fig. 3-10. We also observe a slight increase in the beamwidth of the antenna at higher frequencies which is due to the excitation of a surface wave. As the antenna scans toward endfire, surface wave radiation becomes stronger and

contaminates the leaky-wave radiation. In fact, the main beam of the surface mode becomes very close and almost merged into the main lobe of the leaky mode which widens the beamwidth as can be seen in Fig. 3-13(b).

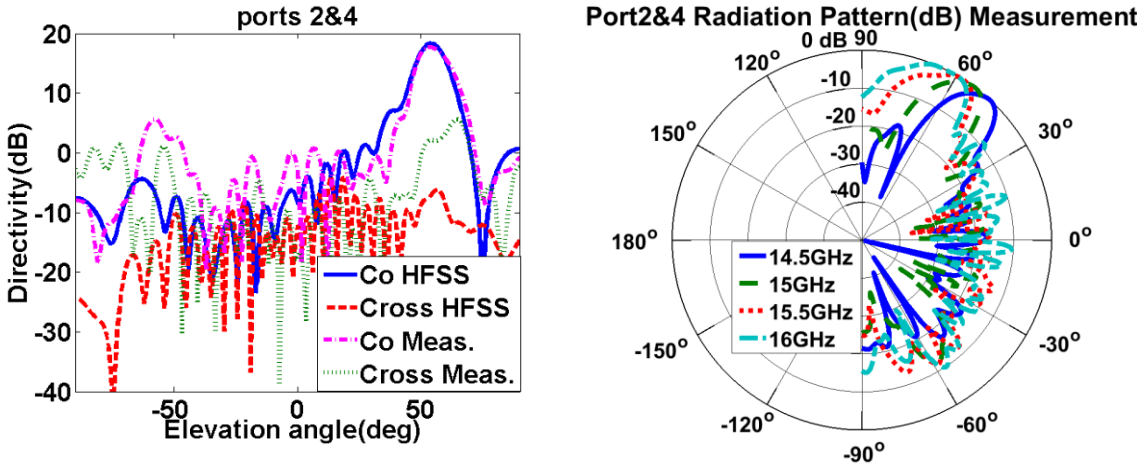

(a) (b)

Fig. 3-13 (a) Comparison of measured and simulated co- and cross-polarized components in the elevation plane for the double stacked antenna when both ports are excited. (b) Measured frequency-scanning behavior in the elevation plane of double stacked antenna when both ports are excited.

The same scanning behavior is also plotted in Fig. 3-14 over the entire range of elevation angles $(-180^o \leq \theta \leq 180^o)$. We observe that beyond the desired range of $-90^o \leq \theta \leq 90^o$, the level of radiation is almost below -15 dB over the entire range of angles and frequencies, except at 16 GHz where the level of back lobe rises and reaches almost -10 dB around $\theta \approx 110^o$.

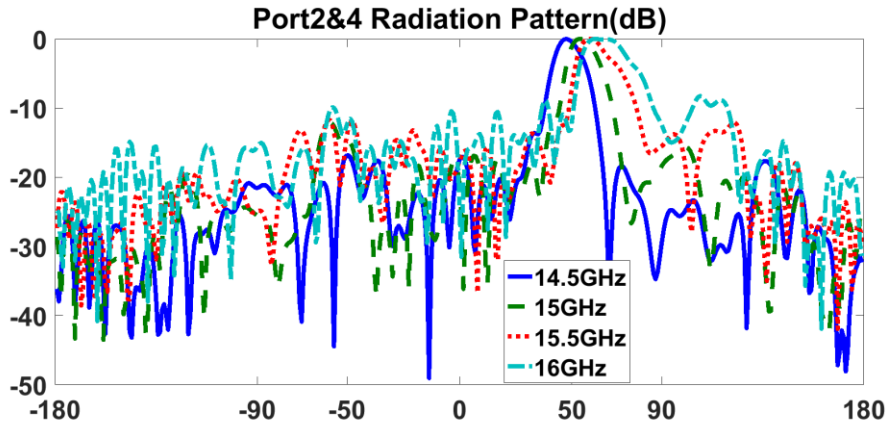

Fig. 3-14 Measured frequency-scanning behavior in the elevation plane for the entire range of angles.

To capture main beam in the azimuth plane, several measurements have been performed to account for the main beam angle pointing at different directions according to the corresponding input port. Results are presented in Fig. 3-15(a) where flat-topped extension of almost 30^o is achieved within 3 dB beamwidth of each individual pattern.

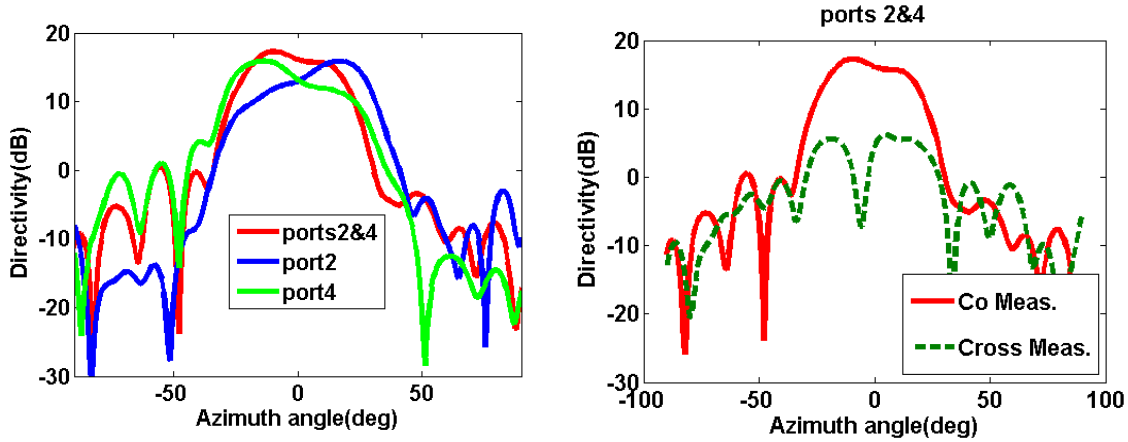

(a) (b)

Fig. 3-15 Measured azimuth plane patterns of double stacked antenna when top antenna is radiating, bottom antenna is radiating and finally when both antennas are radiating. (b) Comparison of measured co- and cross-polarized components in the azimuth plane for double stacked antenna when both antennas are excited.

The value of cross-polarized vs. co-polarized pattern is also shown in Fig. 3-15(b) where it reveals an isolation of better than 12 dB obtained at the main beam angle. It is worth to note that in calculation of 30^o for the extension of flat-topped beam, ripple value

of 1.8 dB was considered. However, for ripple to be less than 1 dB, the azimuth beam reveals flat-topped extension of 21^o and 16^o in simulation and measurement respectively.

3.4 Application in Base Station Antenna Array

In this section we investigate the potential of our proposed design to be used as an element of a base station antenna array system. Of course, different scenarios have different preferences regarding the antenna characteristics. Here a typical scenario is considered where an array of eight of these antennas could be arranged in a cylinder configuration, as illustrated in Fig. 3-16.

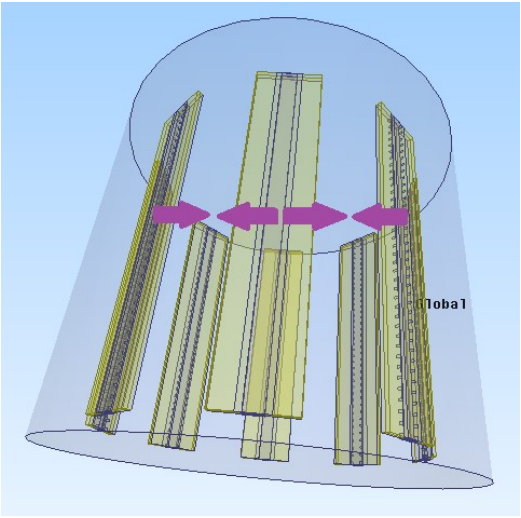

Fig. 3-16 Realization of base station antenna with an array of eight subarray modules proposed in Fig. 3-1.

The whole cylinder could then be mounted on a pole to provide the best all-around performance. In this scenario frequency scanning is done in order for the leaky-wave beam to steer in the elevation plane and choose between different floors of a building and the users distributed across each floor are then covered using the flat-topped beam of the azimuth plane. Results are given in Table. 3-2 where in each floor send and receive channels are assumed to be 400 MHz apart which could be realized by ordinary multiplexers.

The range in the azimuth indicated with $\pm 15^o$ around 80^o. This 30^o span of the azimuth angles considered in Table. 3-2 is for a subarray located at $\varphi = 90^o$ in the azimuth, in eight-element array configuration of Fig. 3-16.

The gain values given in Table. 3-2 are in fact obtained from one subarray module at different frequencies, and φ −cuts. In order to determine what mode of excitation should be used for the subarray to achieve maximum possible gain at an arbitrary φ −cut, we follow the simple rule as below. For every φ −cut the offset between this φ −cut and φ_{max} is calculated where $\varphi_{max} = 90^o$ for simultaneous excitation (ports 2&4) and $\varphi_{max} = 78^o$ in the case of individual excitation (port 2), then the mode of excitation that yields the minimum offset value is selected to illuminate that specific φ −cut. This will yield the subarray switching scheme in the first column of Table. 3-2.

Table. 3-2 Performance of the proposed cylindrical array for a scenario where users are spread in both azimuth and elevation

$\varphi(deg)$	Subarray switching scheme	Co-Polarized Gain (dB)						Array switching scheme
		1st floor		2nd floor		3rd floor		
		Send	Receive	Send	Receive	Send	Receive	
95	Ports 2&4	16.82	16.80	17.91	17.86	17.57	16.69	---
90	Ports 2&4	17.02	17	18.11	18.06	17.77	16.89	---
80	Port 2	15.92	15.60	16.71	16.76	16.52	15.49	---
70	Port 2	15.19	14.60	15.75	15.50	15.20	14.40	P12+P24
65	Port 2	12.57	12.65	13.71	13.76	13	12.55	P12+P24

	14.5	14.7	14.9	15.1	15.3	15.5	15.7	15.9	16.1	*f(GHz)*
	48	50	52	54	56	58	60	62	64	$\theta(deg)$

Hence for angles close to broadside ($\varphi = 90^o$ and $\varphi = 95^o$ as given in Table. 3-2) maximum gain is obtained for the case of simultaneous excitation (ports 2&4) whereas for

the span of angular regions further away from broadside ($\varphi = 80^o$ to $\varphi = 65^o$) the subarray configuration yields maximum gain if only the top antenna (port 2) is excited.

However, once the subarray is located in the cylindrical array configuration, the contribution from adjacent elements, should also be taken into account and added to the original gain of the subarray. Such situation is illustrated by yellow (interfering) beams in Fig. 3-17. To get this done, the *subarray switching scheme* in the first column must be revised to form the *array switching scheme* given in the last column of Table. 3-2 to include the impact from the neighboring element.

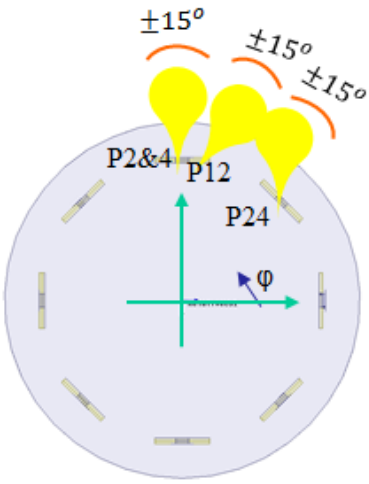

Fig. 3-17 Top view of the cylindrical array and an example of beam interference between neighboring elements according to the array switching scheme given in Table. 3-2

Once beamforming matrices are known, next challenge is to ensure flat-topped coverage in every desired φ −cut. This could be accomplished by beam shaping through the movement of antenna phase centers in the azimuth plane as will be explained below.

In Fig. 3-16 eight subarray modules are arranged in every 45^o. Considering the 3dB beamwidth of 30^o, for the observation angles fit in the span of $\pm 15^o$ around each subarray's broadside, the possibility of having a flat-topped beam is seen to be guaranteed,

through excitation of both ports in the corresponding subarray. (Operation on mode 3, see either Fig. 3-7(a) or Fig. 3-15(a)). In Table. 3-2, the first two rows exemplify a situation like this for a module centered at $\varphi = 90^o$. Also, from the last column it can be seen that the contribution from neighboring elements over this angular sector is negligible and could be ignored. This is because the 30^o flat-topped extension of the beam for the neighboring element located at $\varphi = 45^o$ will drop more than 3 dB before it can reach the angular regions around broadside of the original element ($\varphi = 90^o$, $\varphi = 95^o$, and $\varphi = 80^o$). So, the gain values given for the angles in the first three rows of Table. 3-2 remain intact and will not be affected by the neighboring elements.

The BSA will change its focus from the span of 30^oaround every $45^o\varphi$ −cut to an angular sector in between two subarrays, if the mode of operation in each subarray, changes from simultaneous excitation (mode 3) to one-at-a-time excitation (mode 1 for one subarray and mode 2 for its adjacent neighbor). This will move the phase center in each subarray, from center-broadside to some distance in front of its radiating aperture. Such situation is illustrated by purple arrows in Fig. 3-16 where phase centers from two adjacent contributing elements are moving towards one another, provided that, beamwidths and element spacing are well adjusted beforehand, over the angular sector where they almost coincide, a flat-topped beam emerges, illuminating the area. Such constructive interference phenomenon is described in the last two rows of Table. 3-2 where *Pij* indicates the beam produced by antenna *i* when port *j* is excited. Index *i* takes values of 1 and 2 respectively for the subarray antenna located at $\varphi = 90^o$ and its neighbor at $\varphi = 45^o$.

This example shows that the proposed structure is capable of covering the entire azimuth with flat-topped beams and this beam shaping occurs through *virtual* moving of phase centers without actually bending or changing shape, size, or location of antennas in the array. It proves that our design is suited for scenarios where users are separated in the horizontal azimuth plane. This configuration is also efficient in terms of keeping the installation and site costs to minimum since it prevents additional costs associated with mechanisms necessary for deployment of large antennas and substantial space required for widely spaced arrays.

Despite all the above advantages of the proposed antenna in the azimuth, one should note that leaky-wave antennas have limited bandwidth due to the beam squint phenomena that happens with variation of frequency in the elevation. This could change the coverage size of a desired sector. In our proposed design a variation of a few hundred MHz results in the sector size change of a few degrees which may not be ideal for base stations operating over a wide frequency band although for 10 MHz bandwidth of the 2 GHz LTE band a deviation of $\pm 0.7^{o}$ for main beam of an LWA in base station is reported *'negligible beam squint'* and acceptable [43]. In general, a squint-free leaky-wave beam over a broad bandwidth is much more desirable and it can be achieved by using methods such as implementation of metamaterials which is not the focus of this work. The proposed design here is qualified for multi-beam switching in the azimuth and, in the elevation plane to avoid beam squint, it can be seen as a spatial spectrum analyzer. The frequency-beam steering property of the LWA can be effectively used to map each frequency to a particular direction in space thereby providing a real time frequency-space separation mechanism. The real time spectrum analyzer (RTSA) as discussed in [44] takes advantage of the spectral-spatial decomposition property of LWA to analyze complex signals and it is widely used in radars and electromagnetic interference and compatibility systems.

3.5 Comparison with other Base Station Antennas

In this section we briefly compare the characteristics of our proposed design against other popular types of BSA (given in Table. 3-3) such as lens antennas, leaky and traveling wave arrays, patch arrays, and dipole slot arrays. More detailed features are listed in Table. 3-3. In listing these criteria in Table. 3-3, several fundamental challenges in BSA design are considered. These challenges were identified by taking into account requirements that would allow 5G to successfully perform its five exemplary scenarios [45]. Some of the challenges are reflecting the link budget related requirements such as capacity enhancement and latency reduction, whereas some others are to address issues such as network densification to assess if the BSA is efficient in terms of power consumption and realization costs. (e.g. how many access points/antenna elements are required for a specific coverage area, availability of low cost and energy-efficient devices). Each class of the BSAs presented in Table. 3-3 has employed different strategies to overcome design

challenges. In the following we discuss these strategies and also, explain how the solutions employed in our proposed design are most likely capable of tackling these challenges.

3.5.1 Flat-topped beam

As mentioned in the introduction, higher SNR and lower BER can be achieved by transmission of flat-topped beams. This is very beneficial for 5G since network will be capable of serving more traffic while still maintaining an acceptable SNR, hence increasing the network capacity. Generating flat-topped beam is one of the key aspects of our design and is also important from another aspect; solving network densification problem. As proven in [25], flat-topped beams tend to preserve good SNR over wider communication range. Therefore, generating flat-topped beam in general makes the design appropriate for networks with larger cell size as it is capable of providing service over a larger coverage zone.

3.5.2 Phase shifters

Phased arrays are effective solutions for all cell geometries and environment and the design could be independent of the layout of the coverage area as in [46] and [47]. However, they are not efficient in terms of phase shifters' realization and cost especially at higher frequencies. Furthermore, use of phase shifters makes it difficult to maintain 5G's strict limits of low intermodulation level. In this regard lobe-switched antennas (as in [48] and our work) and also fixed-beam lens antennas (as in [49]) are more appropriate choices. In fact, the former has gained a lot of attention in 5G community due to its ability to cover a large sector without having to resort to current inefficient steering solutions such as low-speed mechanical or costly electronic scanning. However, in both of these cases (switched-beam arrays and lens antennas), unlike the phased arrays, antenna design must be in accordance with the cell configuration.

3.5.3 Low cost reproducibility

In general lens antennas as in [49] and patch arrays as in [48] have the advantage of low-cost mass production. However, lenses are 3D structures whereas in many scenarios, planar configurations such as our proposed design or antennas in [48] and [50] are more

favorable choices. Another factor that could affect reproducibility is the feed simplicity. In this regard the antenna introduced in this work and, also the one in [48] outperform those of [49] and [50]. This is due to the complicated feeding mechanism provided by 3D waveguides in [49] and, also Butler matrices in [50].

3.5.4 2D beam forming

Beam forming will provide an opportunity for shaping the pattern which among other things results in an efficient use of transmitter power over the coverage area. In our design it is easily done through the change of phase centers, only by switching excitations at the input ports. In some other antennas such as adaptive arrays of [50], more complex beamforming networks based on Butler matrices are employed that can dynamically change the pattern however due to their complex signal-processing algorithms they also alter the radiation pattern to some extent. In [49] Geometric Optics (GO) can be used to calculate a surface profile which will optimally transform radiation of the waveguide feed into the desired coverage. Shaping the 3D surface of the lens also conveniently compensates path loss and ground reflection. This will keep multipath fading down and as a result reduces the delay spread and hence number of equalizers required for the network.

3.5.5 High gain

In general having a high-gain directive narrow-beam (as produced by LWA in our design and adaptive arrays of [50]) is advantageous due to several reasons including higher carrier-to-interference (C/I) ratio and better likelihood for line of sight (LOS) arrival which will in turn reduce the number of parameters that has to be estimated to obtain channel state information (CSI) [1], [50]. This will also reduce the delay spread and save the network from the excessive use of equalizers. The high-gain beam also allows for additional coverage and hence could combat aesthetic difficulties and installation costs associated with densification of networks [50]. Another solution to extend antenna coverage and solve for network densification problem, as mentioned earlier, is by generating flat-topped beams as done in our proposed design.

Table. 3-3 Comparison between different base station antennas

Antenna Type	Flat-Topped OR Shaped Beam	Phase Shifters	Feed Simplicity / Planar	Dimension OR Number of Elements	Coverage area / Beamforming	Frequency / Gain
Microstrip Patch Phased Array with Adaptive Beamforming [47]	No	Yes	No	$440\ mm \times 320\ mm$ $41\ \lambda_o \times 30\ \lambda_o$	1 km	28 GHz
			Yes	8 Subarrays each made of 4×2 Patch Antennas Total of 64 Elements	Beam Steering	21 dB
Slot Dipole Phased Array [46]	No	Yes	No	$72\ mm \times 52\ mm$ $5.3\ \lambda_o \times 4\ \lambda_o$ $11\ \lambda_r \times 8\ \lambda_r$	$\pm 60^o$ Sector Elevation	22.25 GHz
			Yes	8 Subarrays each made of 1×8 Slot Dipole Antennas Total of 64 Elements	Elevation Beam Steering	19 dB
Switched-Beam Travelling-Wave Microstrip Patch Array [48]	No	No	Yes	$50\ mm \times 25\ mm$ $4\ \lambda_o \times 2\ \lambda_o$ $12.5\ \lambda_r \times 6.25\ \lambda_r$	90^o Sector Elevation 60^o Sector Azimuth	24 GHz
			Yes	Inner and Outer Subarray made of 1×8 and 1×11 Patch Antennas Total of 19 Elements	Elevation Beam Steering	10 dB
3D Dielectric Lens Antenna [49]	Shaped Beam $sec^2\theta$	No	No	$106\ mm \times 40mm \times 20\ mm$ $21\ \lambda_o \times 8\ \lambda_o \times 4\ \lambda_o$	40 m - 240 m	60 GHz
			No	1 Lens Antenna	Fixed-Beam	11.4 dB
Aperture-Coupled Microstrip Patch Adaptive Antenna [50]	No	Yes	No	$1250\ mm \times 500\ mm$ $7.5\ \lambda_o \times 3\ \lambda_o$	$\pm 60^o$ Sector Azimuth	1800 MHz
			Yes	---	Azimuth Beamforming	22 dB
Aperture-Coupled Microstrip Patch Adaptive Antenna [50]	No	Yes	No	$800\ mm \times 900\ mm$ $2.42\ \lambda_o \times 2.72\ \lambda_o$	$\pm 60^o$ Sector Azimuth	900 MHz
			Yes	---	Azimuth Beamforming	16.5 dB
Our Proposed Leaky-Wave Cylindrical Array (Simulation results)	Flat-Topped Beam	No	Yes	$150\ mm \times 28.9\ mm$ $7.5\ \lambda_o \times 1.4\ \lambda_o$ $11.12\ \lambda_r \times 2.14\ \lambda_r$	360^o Azimuth 26^o Elevation	15 GHz
			Yes	8 Subarrays each made of 2 LWA Total of 16 Elements	Azimuth Beamforming Elevation Beam Steering	17.59 dB

3.6 Conclusion

In this chapter we proposed and implemented a novel frequency scanning leaky-wave antenna which has the ability to dynamically switch the main beam direction between different angles in the azimuth plane thereby providing three modes of operation. The proposed architecture is synthesized in the SIW technology. This topology has made up of two LWA each generating a high-gain leaky-wave beam in the elevation plane that scans with frequency. The ability of this antenna to dynamically switch the input ports to illuminate a specific region of space required by a certain application, gives this architecture enough flexibility to satisfy requirements for multi-beam systems using only a simple fed unit. However, in the elevation plane, the frequency beam scanning though well suited for applications such as RTSA, is not ideal for wide band base stations. Despite the beam squint problem, a wider scanning range translates to using more frequency resources which will be expensive in terms of realization. In this case a fixed-frequency beam scanning is much more desirable as it prevents signal distortion in baseband and will alleviate problems such as SLL increase and gain reduction, that are otherwise inevitable when scanning over wide angular regions. Moreover, by having fixed-frequency scanning capability, only one set of transceiver module working at the frequency range of interest is adequate for baseband signal processing. This will result in more compact and cost-efficient system design due to notable reduction in the number of multi-frequency transceivers. The proposed design could be integrated with varactors or pin diodes to accomplish reconfigurable LWA with more robust performance in terms of scanning, in the elevation plane. Using metamaterials for reduced beam squint is another way to obtain fixed-frequency beam scanning. This could help to achieve more reconcilable solutions in terms of radiation performance, size and cost in mobile communication applications.

Chapter 4

4 Waveguide Slot Antenna Array

4.1 Introduction

The Waveguide slot antennas are widely used particularly because they can handle high powers and produce high directivity beams. The basic idea for a slot array is to create holes in the conductor surface such as to interrupt current density. Slots radiate due to the interruption of current flow on the waveguide wall as a result of conductor discontinuity. Appropriate choice of the shape, orientation and relative positioning of slots along the guiding structure can lead to many interesting radiation patterns useful for many mm-wave applications where high gain and high-power transmission is requested. In the following first, a brief overview of commonly used slot radiators is presented. Then different types of slot arrays along with general guidelines to achieve different radiation characteristics are discussed. Next, design procedures to generate required polarizations are investigated. The topology of our circularly polarized slot antenna array and feeding technique is described in the next chapter.

4.2 Common Slots

Fig. 4-1 (a-d) shows the TE10 mode on waveguide walls and the three common types of slots. The longitudinal slot at the center line of broad wall (slot(a)) barely radiates as it hardly cuts any current line. However, if we introduce a little offset as can be seen in slot (b), the amount of electric field induced in the slot will increase and slot (b) becomes a radiating slot as it cuts through the transverse currents on the broad wall. It is clear from Fig. 4-1 that reversing the direction of offset will in fact change the polarity of electric field in the slot.

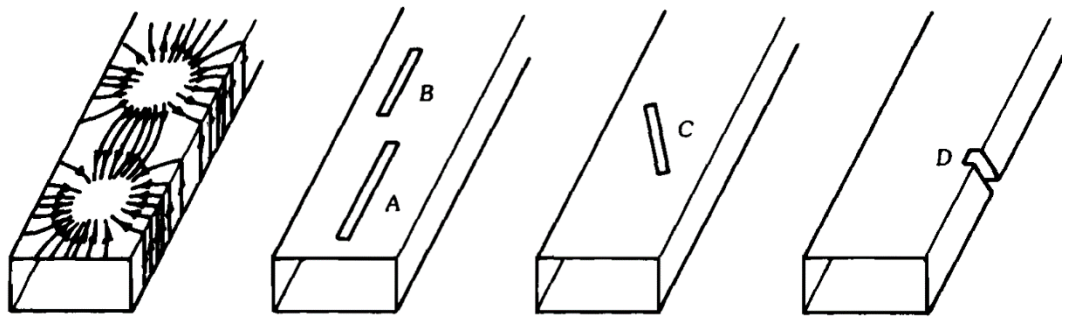

Fig. 4-1(a) Waveguide TE10 current distribution (b) Longitudinal broad wall slot (c) Centered inclined broad wall slot (d) Inclined narrow-wall slot. Courtesy of [51]

The inclined slot along the centerline of the broad wall (slot(c)) interrupts the longitudinal currents and again polarization of E fields will be reversed if the tilt angle is reversed in the opposite direction.

Last but not least, is the edge slot on the narrow wall of the waveguide which interrupts the transverse currents. Slot (d) will radiate reversely-polarized E fields if the direction of inclination is reversed.

One common characteristic of all the above slots is that the amount of radiated field and its polarity can be controlled by changing the offset or inclination of the slots [51].

4.3 Standing and Traveling Wave Slot Arrays

In a general waveguide slot array, if the inter-element spacing between slots is set at $\lambda_g/2$ where λ_g is the guided wavelength, and the array is terminated with a short or open, then it is called a standing wave array whereas if the slot spacing is other than a half-guided wavelength and a matched load is placed at the end, the array is said to be a traveling wave array [51]. Both types are briefly discussed as follows.

4.3.1 Resonantly spaced (standing wave) broadside array

From theory of linear antenna arrays we know if the elements have common phase (progressive phase factor = 0, $2n\pi$) then a broadside radiation can be obtained. In the context of slot array this will happen when slots are $\lambda_g/2$ apart with alternative offsets or tilt angles as shown in Fig. 4-2.

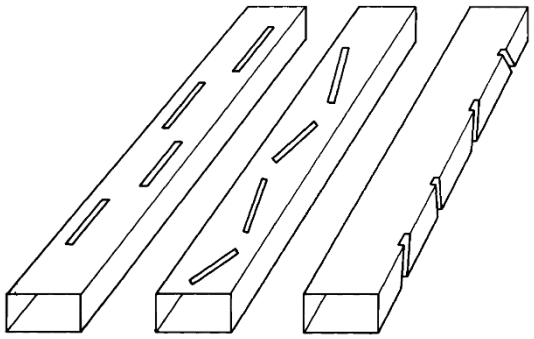

(a) (b) (c)

Fig. 4-2 Linear slot array of alternative (a) Longitudinal broad wall slots (b) centered inclined broad wall slots (c)Inclined narrow-wall slots. Courtesy of [51]

The $\lambda_g/2$ spacing in fact introduces a π phase shift which is compensated by the phase reversal caused due to alternative tilting or alternate offset, resulting in an equi-phase aperture distribution which generates broadside radiation.

4.3.2 Non-resonantly spaced (traveling-wave array) with off-broadside beam

In the case of traveling wave slot antenna when slots are designed to be at a distance *d* apart where $d \neq \lambda_g/2$, two cases need to be studied for the phase progression.

4.3.2.1 Case1. Slots are alternatively spaced at equal distance d where $\boldsymbol{d \neq \lambda_g/2}$

In this case the general array factor formula can be modified as below to account for the extra phase shift of βd and phase reversal π.

$$F(\theta) = \sum_{n=1}^{N} e^{-jnd(K_0 cos\theta - \beta_{10})} e^{-j\pi} \qquad (4\text{-}1)$$

Now the beam pointing angle is given by

$$cos\theta_{rad} = \frac{\beta_{10} d - \pi}{K_0 d} \qquad (4\text{-}2)$$

It can be seen that where the beam lies in the space actually depends on the spacing *d*.

If $\beta d < \pi$ then

Beam points at some angle between broadside and reverse endfire. Also note that *d* should be chosen greater than a certain value to avoid slot overlap and prevent the internal higher-order mode coupling. Also, the upper limit on *d* should be set such that $\beta d - \pi$ is not very close to zero as it causes the reflections from slots to add up in phase and ruin the matching at the input port.

If $\beta d > \pi$ then

In this case beam to point at a direction between forward endfire and broadside. The upper bound on *d* should be set not to permit the possibility of multiple beams. There is obviously

a lower limit on *d* cause as βd gets closer to π, the in-phase interactions between reflections from different slots results in mismatch at the input.

4.3.2.2 Case2. Slots are equi-spaced at distance d where $\boldsymbol{d \neq \lambda_g/2}$

In this case equation (4-3) indicates a phase progression of $\beta_{10}d$ being added to the general array factor formula.

$$F(\theta) = \sum_{n=1}^{N} e^{-jnd(K_0 cos\theta - \beta_{10})} \qquad (4\text{-}3)$$

This happens when $\beta_{10}d$ is the only phase shift between slots and no other extra factor as a result of phase reversal is being added to the total phase of the array. One example of such scenario would be when all the slots are on the same side of the center line on the broad wall of the waveguide. It is easy to see that in this case the beam points at θ_{rad} described by the equation below.

$$cos\theta_{rad} = \frac{\beta_{10}}{K_0} \qquad (4\text{-}4)$$

It is obvious that in this case, the result does not depend on the inter-element spacing, *d* and regardless of the choice of *d*, beam points somewhere between the forward endfire and broadside. Parameter *d* can be chosen large enough so that slots do not overlap yet not too big to avoid multiple main beams.

The above discussion gives general guidelines on the choice of suitable structure of waveguide slot antenna to obtain either fixed broadside beam or a tilted off-broadside beam that can also be scanned with frequency. Since in chapter 3 the focus of study was on beam scanning leaky-wave antennas, in order to have a thorough study, for what follows we focus on the design and analysis of a fixed broadside beam.

4.4 Polarization

If more specific requirements such as a particular polarization is needed to be met for a particular application, deeper analysis has to be done to decide on the appropriate configuration. In general, for simple linear polarizations (vertical/horizontal) achieving a broadside beam is easy as the slots can be placed every $\lambda_g/2$ and still generate an in-phase radiation given that the phase reversal condition is met either by alternating the offsets from the center line on the broad wall or by alternating the rotation angle for narrow-wall edge slots. The electric field for the latter case is shown in Fig. 4-3 where opposite inclination of the adjacent slots helps to cancel out the vertical component of the E field, resulting in the horizontally polarized radiation.

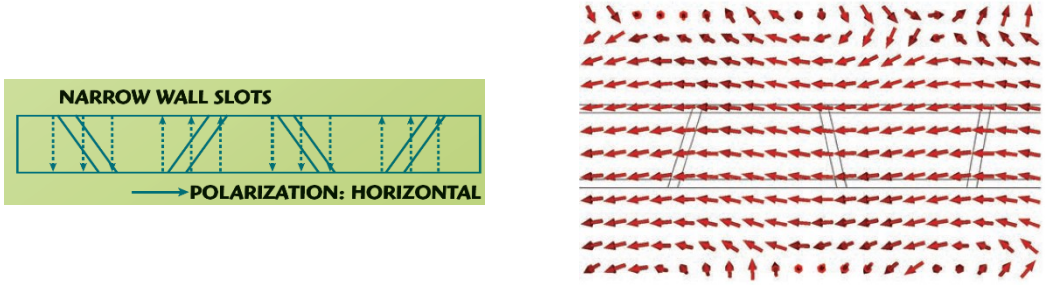

(a) (b)

Fig. 4-3 (a) Dashed lines represent current flow on narrow wall for a TE10 standing wave condition (b) Vertical E field is cancelled as a result of alternatively rotated edge slots located at 0.5 λ_g *intervals, leading to horizontal polarization. Courtesy of [52]*

For a more complicated case of a diagonal linear polarization (for example 45 degrees) or a circular polarization however these simple geometry tricks (alternating offset or inclination) do not produce desired results and an inter-element spacing of λ_g must be considered for the in-phase condition required by the broadside radiation. The following two cases are studied in this regard.

4.4.1 Hollow waveguide

The relationship between λ_g and λ_o in a hollow waveguide is given in (4-5). Plots are also provided for a hollow waveguide of width $a = 3.36mm$ to better illustrate the concept.

$$\lambda_g = \frac{\lambda_o}{\sqrt{1 - (\frac{\lambda_o}{2a})^2}} \qquad (4\text{-}5)$$

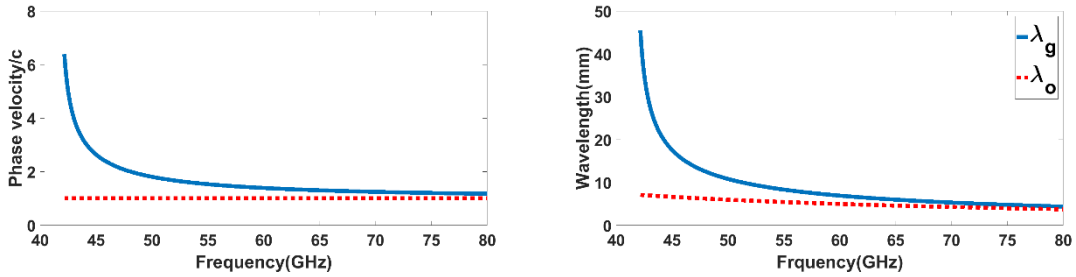

(a) (b)

Fig. 4-4 Hollow waveguide of a=3.36mm and b=1.6 mm (a) Phase velocity (b) Guided wavelength.

It is clear that the slot spacing of λ_g becomes greater than λ_o which would translate to the emergence of grating lobes in a slot array pattern. Appearance of grating lobes will decrease the antenna gain and in some particular applications such as radar systems it could have some undesirable effects such as detection of a ghost image in the direction of the grating lobe [21]. Also from the plots of Fig. 4-4 it is obvious that if a slot array needs to be designed in this case an appropriate choice for the operating frequency is toward the end of the single TE10 mode propagation band, just below the TE20 (or TE01) cutoff frequency. At this point λ_g is very close to λ_o which can satisfy the in-phase radiation for an *almost* grating lobe-free broadside pattern. However, one has to deal with the problem of narrow bandwidth in this case.

Pros: width of the waveguide could be chosen large enough therefore fitting a resonant slot is possible which will lead to more radiation.

Cons: appearance of grating lobes which will result in gain and efficiency degradation and narrow bandwidth in order for TE10 single mode propagation.

Design challenges: for narrow wall waveguide slot arrays, increasing the width of the waveguide to have λ_g closer to λ_o, will reduce the power density around the slots making the radiation mechanism more challenging. In this case normally a post or cavity is needed to be designed to increase the power density around the slot.

4.4.2 Dielectric loaded waveguide

One way to remedy the situation of grating lobes appearance for broadside radiation is to fill the waveguide with dielectric. In this case λ_g as described by equation (4-6), is plotted in Fig. 4-5.

$$\lambda_g = \frac{\lambda_o}{\sqrt{\varepsilon_r - (\frac{\lambda_o}{2a})^2}} \qquad (4\text{-}6)$$

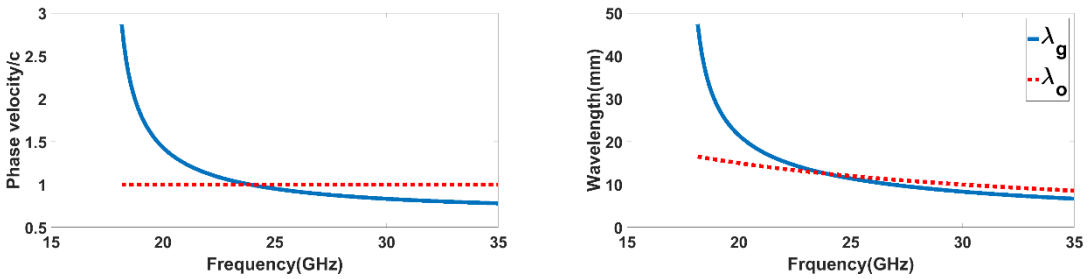

(a) (b)

Fig. 4-5 Dielectric loaded waveguide of a=5.72mm and b=3 mm and $\varepsilon_r = 2.2$ (a) Phase velocity (b) Guided wavelength.

It can be seen that over the slow wave frequency range λ_g becomes smaller than λ_o and therefore an equi-spaced slot array of interelement spacing λ_g will no longer suffer from the emergence of the grating lobes.

Pros: broadside radiation is possible with no grating lobes.

Cons: less efficiency due to added loss of the dielectric.

Design challenges: According to the equation of cutoff frequency, $f_c = \frac{c}{2a\sqrt{\varepsilon_r}}$ as ε_r increases, width of the waveguide *a,* has to become smaller in order to guarantee the TE10 single mode operation. This will limit the area on the waveguide wall therefore resonant slots cannot fit. Since the range of slot lengths that can be fitted in the waveguide wall is limited, realization of a prescribed aperture distribution becomes challenging but still possible if some of the stringent conditions on SLL in a sum or difference pattern (or ripple in a shaped beam pattern) are relaxed.

4.5 Conclusion

In this chapter we summarized general guidelines on slot array design and how the location and spacing of slots can change along the array to achieve a certain polarization. Two types of slot arrays namely traveling and standing wave were discussed along with the waveguide medium in which these antennas can be realized. From the dispersion plots provided, it was visually evident that in a waveguide filled with air only, the $n = 0$ mode is a fast wave. In order to suppress the dominant mode and retain radiation from $n = -1$ harmonic, a common practice is to introduce phase reversal. This can be accomplished by alternately switching the offset of slots from the centerline in the broad wall or alternating the tilt angle for the edge slots on the narrow wall. It was shown however if a waveguide is filled with dielectric, the phase reversal is no longer necessary. Distinction between air filled and dielectric loaded waveguide were clarified in detail through elaboration of advantages, disadvantages and design challenges imposed on the antenna designer in each environment.

Chapter 5

5 Circularly-Polarized Narrow Wall Slot Array

5.1 Introduction

One observation from previous chapter is that Leaky-wave antennas have the advantage of producing highly directive beams that can be scanned with frequency. This is very favorable when scan range is large and restrictions on size and cost do not allow utilization of phase shifters. There are some applications however such as point-to-point communication systems where a fixed broadside beam is preferred over a tilted off-broadside leaky-wave beam. In this case slot arrays are more appropriate. They could produce interesting behavior similar to periodic LWA such as highly directive beams however their difference lies in the nature of individual discontinuities and the fact that broadside radiation is possible. Therefore, in order to cover requirements of different 5G base station systems, in this chapter we attempt to design a narrow-wall waveguide linear slot array. Regarding the polarization, since a linearly polarized antenna array is designed in chapter 3, here we focus on the design of a circularly polarized slot array.

Despite the wealth of knowledge available in the literature about linearly polarized slot arrays, and some examples of CP broad wall waveguide slot arrays, not much can be

found on the discussion of CP arrays on the narrow wall. Existence of both transverse and longitudinal surface currents and more available space on the broad wall makes it easier for placement of variation of orthogonal slot radiators to achieve CP whereas restricted area on the narrow wall and a single surface current makes it very challenging for creating CP radiations from narrow-wall slot arrays. To alleviate these problems, a novel design approach is introduced which can achieve CP by using unit cells composed of a pair of slots and metallic posts and it is shown that radiation performance according to desired Taylor aperture distribution is obtainable. Taylor distribution is chosen in accordance with most recent literature since the excitation factors for such aperture distribution lead to smooth variation of geometry between adjacent slots. This will keep the mutual coupling down. Therefore, even in the case of total disregard of mutual coupling factors, the resulting pattern would not be as dramatically different from the ideal. Also, in our design the existence of posts on the opposite side of the slots helps to reduce mutual coupling as they cancel out reflections between slots and limit the backward traveling waves that could contribute to mutual coupling. Also, for many applications, having monotonic decrease of side lobes as offered by Taylor distribution, is more desirable than Dolph-Tschebyscheff distribution with equal SLL, as the decaying minor lobes further diminish the effect of interfering and spurious signals.

We also investigate for the first time the feasibility of using multilayer PCBs to assemble the narrow-wall slotted waveguide antenna configuration for applications at 26GHz band. Such practice has been adopted in the literature for realization of SIW and C band waveguide using 4 to 30 board layers [53] and [54]. Other more expensive technologies to realize flexible SIW structures include LTCC, photoimageable thick film material and ion-track technology performed on structures working in the W band (75-110GHz) [53].

This stack-up approach would allow for more flexibility in design as the width of the waveguide can be made longer or shorter and different stripline probe feeding techniques can be used depending on the application. Requirement for realization of such antenna in a multilayer PCB topology is discussed throughout this chapter.

Fig. 5-1 depicts initial configuration where eight Rogers 5880 dielectric substrates are stacked up to create the required width of the waveguide *a=5.7mm* for the TE10 single mode operation in the frequency band of 25-26 GHz. Choice of 26 GHz band was inspired by slot arrays developed for base stations in local multipoint distribution systems (LMDS). Waveguide narrow wall is selected equal to *b=3mm*. Later in this chapter where slot geometries and post heights are discussed in more details, number of layers and their arrangement will be changed in order to achieve good antenna performance.

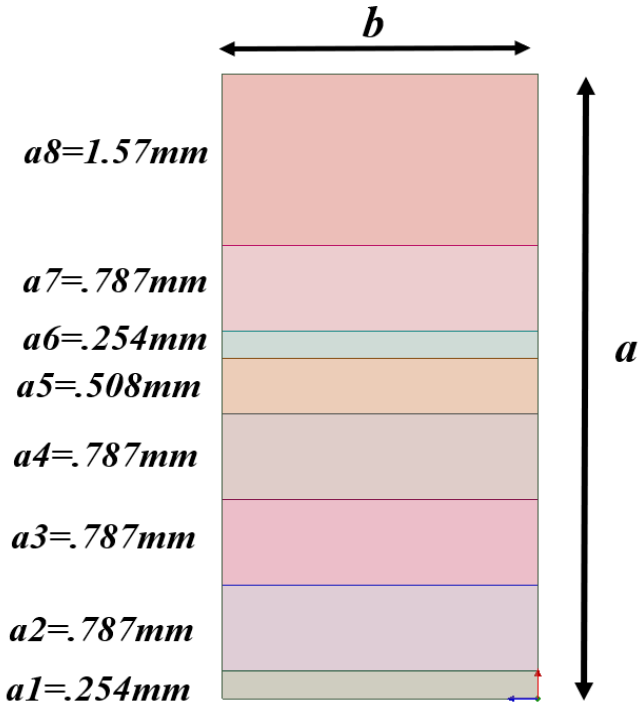

Fig. 5-1 Eight layer stack up of standard thickness Rogers 5880 dielectric substrates to realize a waveguide of width a=5.7mm.

Compared to its broad wall counterparts, the proposed narrow-wall antenna offers a low-profile design for future development of planar arrays. Furthermore, its multilayer PCB topology is advantageous in terms of full integration with the rest of planar circuitry.

5.2 Traveling Wave Slot Array Concept

An N element linear traveling wave slot antenna array is illustrated in Fig. 5-2.

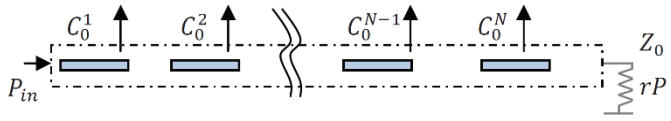

Fig. 5-2 Traveling wave slot antenna array. Courtesy of [55].

C_ns are radiation coefficients corresponding to a specific aperture distribution, P_{in} is the input power and $rP = |S_{21}|^2$ is the estimated power dissipated into the matched load. Array elements are numbered from the feed to the termination load. If the first element radiates P_1

$$P_{in}C_0^1 = P_1 \quad (5\text{-}1)$$

Then $P_{in}(1 - C_0^1)$ is the power incident on element 2, then the power radiated by this element is given by

$$P_{in}C_0^2(1 - C_0^1) = P_2 \quad (5\text{-}2)$$

Using the same logic, the power radiated by the third element can be described by

$$P_{in}C_0^3(1 - C_0^2)(1 - C_0^1) = P_3 \quad (5\text{-}3)$$

Hence the following recursive equation is derived [55]

$$P_{in}C_0^k \prod_{n=2}^{k} 1 - C_0^{n-1} = P_k \quad (5\text{-}4)$$

Defining C_0^n as

$$C_0^n = 1 - |T^{(n)}|^2 \quad (5\text{-}5)$$

From (5-1) to (5-3) we conclude

$$P_1 = P_{in}(1 - |T^{(1)}|^2) \quad (5\text{-}6)$$

$$P_{inc}^{(2)}=P_{in}(1-C_0^1)=P_{inc}^{(1)}|T^{(1)}|^2$$
$$P_2=P_{inc}^{(2)}(1-|T^{(2)}|^2) \quad (5\text{-}7)$$

and

$$P_{inc}^{(3)}=P_{in}(1-C_0^2)(1-C_0^1)=P_{inc}^{(2)}|T^{(2)}|^2$$
$$P_3=P_{inc}^{(3)}(1-|T^{(3)}|^2) \quad (5\text{-}8)$$

So, in general

$$P_{inc}^{(k)}=P_{inc}^{(k-1)}|T^{(k-1)}|^2$$
$$P_k=P_{inc}^{(k)}(1-|T^{(k)}|^2) \quad (5\text{-}9)$$

To design a linear array, first step is to obtain values of equi-phase excitation for a desired distribution, v_k, where

$$v_k=\sqrt{P_k} \quad (5\text{-}10)$$

Once v_k coefficients are known, P_k values can be derived from (5-10). Then $T^{(k)}$ values are obtained from (5-9) and eventually, radiation coefficients C_0^k can be calculated from (5-5).

A 13-element array with Taylor distribution with -20 dB SLL is considered. Ideal excitation coefficients for this distribution are plotted in Fig. 5-3.

The $|S_{21}|$ values corresponding to the appropriate coupling coefficients for such distribution are given in Table. 5-1.

Table. 5-1 Required $|S_{21}|$ values in dB for a prescribed pattern distribution.

Cell No.	1	2	3	4	5	6	7	8	9	10	11	12	13
$\|S_{21}\|$	-0.2	-0.38	-0.42	-0.55	-0.78	-0.9	-1.11	-1.37	-1.37	-1.68	-1.68	-1.68	-1.68

If mutual coupling is ignored, then $S_{21}^{(n)} = T^{(n)}$. Using S_{21} values in Table. 5-1 and formulas given in (5-9), normalized radiated power from each element is calculated and plotted against ideal values in Fig. 5-3. It can be seen that the S_{21} values of Table. 5-1 provide a decent approximation of the ideal Taylor distribution and therefore can be used as initial values to design appropriate unit cell geometries for the antenna design problem.

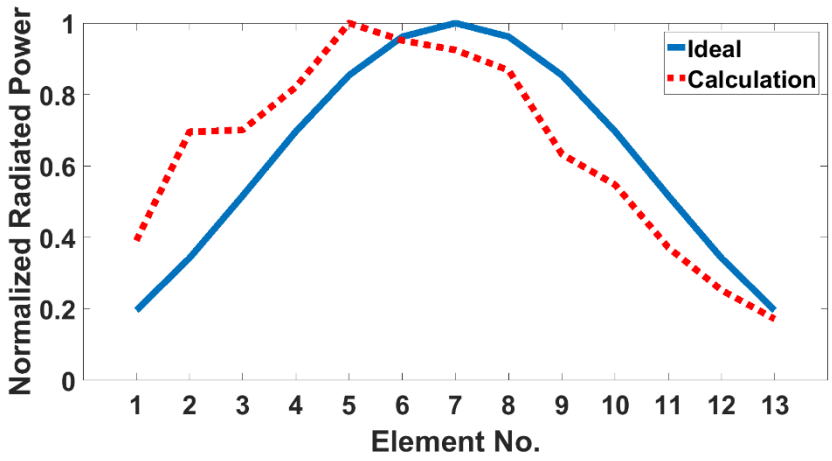

Fig. 5-3 Comparison between ideal and approximate normalized radiated power for Taylor distributation with SLL=-20 dB.

5.3 Unit Cell Characterization

Each unit cell consists of two inclined slots cut on the narrow wall of the waveguide. Since the narrow wall limits the slot length, in order to achieve the required radiation, metallic posts are located on the opposite side of the slot so to increase the energy coupled

from waveguide to the open region on top of the slot. The configuration of unit cell is seen in Fig. 5-4.

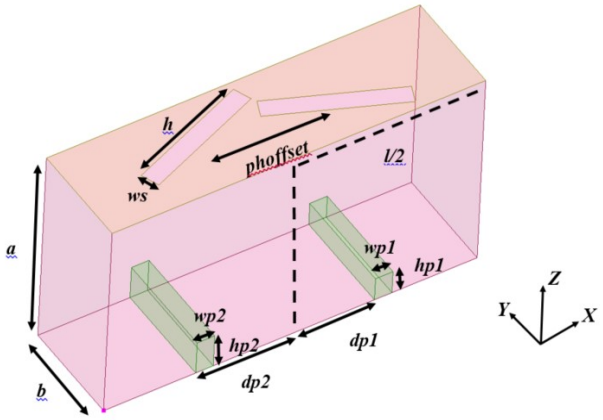

Fig. 5-4 Unit cell configuration and parameters.

Slot length, h determines radiation efficiency. Longer slot causes more energy to be radiated outside the waveguide. Larger slots length also translates to more reflection. Hence h affects both $|S_{21}|$ and $|S_{11}|$. $|S_{21}|$ also changes by mutual coupling which depends on distance between the slots.

Metallic posts are to improve S_{11}. The posts can cancel out the reflections from slots if the amplitudes of reflections from posts and slots are equal and they add up with 180^o phase difference.

To have equal reflection amplitudes, post height, hp must vary proportionally with h to control $|S_{11}|$.

Posts Offsets, dp, control the phase. Also, as slot length increases, so the phase perturbation. Hence dp has to accept larger values to compensate the reflection phase. Therefore, dp also varies proportionally to h.

Distance between the slots, *phoffset* and the tilt angle can change the phase between two orthogonal E fields and affect the axial ratio. Excited E fields also depend on slot

length, *h.* Therefore, values of *phoffset*, tilt angle and vertical offset of the slots should be tuned along with slot length *h* to achieve CP.

The design approach for the unit cell is to model slots and posts in a waveguide of length λ_g. A parameter sweep is conducted to obtain optimum values for key parameters i.e., slots length, slots spacing, tilt angle, post heights and offsets that would achieve the desired coupling factors according to Table. 5-1. Results of this study are given in Table. 5-2.

Table. 5-2 Optimum parameters for the unit cell to achieve CP with good return loss values. All the length units are in mm, angle unit is degree and scattering parameters and axial ratio are in dB. wp1 and wp2 are equal therefore only one column is designated for wp parameter.

Cell No.	h	Phoffset	Tilt	dp1	dp2	hp1	hp2	wp	S11	S21	AR
1	3.3	3.7	25	1.9	2.1	0.67	0.67	0.4	-27.78	-0.2	1.08
2	3.6	3.6	27	2.3	2.1	0.67	0.508	0.4	-31	-0.38	0.32
3	3.7	3.7	26	2.5	2.2	0.67	0.67	0.5	-32.94	-0.42	1.17
4	3.8	3.6	22	2.7	2.4	0.96	0.67	0.5	-32.9	-0.55	1.06
5	3.9	3.7	23	2.5	2.55	1.25	0.67	0.2	-27.18	-0.78	1.07
6	3.95	3.65	24	2.4	2.4	0.96	0.508	0.5	-27.01	-0.9	1.54
7	4	3.8	23	2.2	2.2	1.25	0.96	0.5	-31.03	-1.11	0.67
8	4.1	3.8	24	2.2	2.2	1.25	1.25	0.5	-30.9	-1.37	0.87
9	4.1	3.8	24	2.2	2.2	1.25	1.25	0.5	-30.9	-1.37	0.87
10	4.2	3.7	23	2.2	2.4	1.25	1.25	0.3	-32	-1.68	0.97
11	4.2	3.7	23	2.2	2.4	1.25	1.25	0.3	-32	-1.68	0.97
12	4.2	3.7	23	2.2	2.4	1.25	1.25	0.3	-32	-1.68	0.97
13	4.2	3.7	23	2.2	2.4	1.25	1.25	0.3	-32	-1.68	0.97

Unit cell scattering parameters, along with far-field patterns and axial ratio for some selected unit cells from Table. 5-2 are plotted in Fig. 5-5 (a) and (b) and Fig. 5-6 (a) and (b). Half-space radiation plot contours are illustrated in Fig. 5-5 (c) and (d) and Fig. 5-6 (c) and (d). It can be seen that the co-polarized gain (LHCP) has its maximum around the center (θ=φ=0) where the cross-polarized component is minimum. Moving outward from center along horizontal axis (increasing θ) results in the co-polarized gain to drop and cross component (RHCP) to increase.

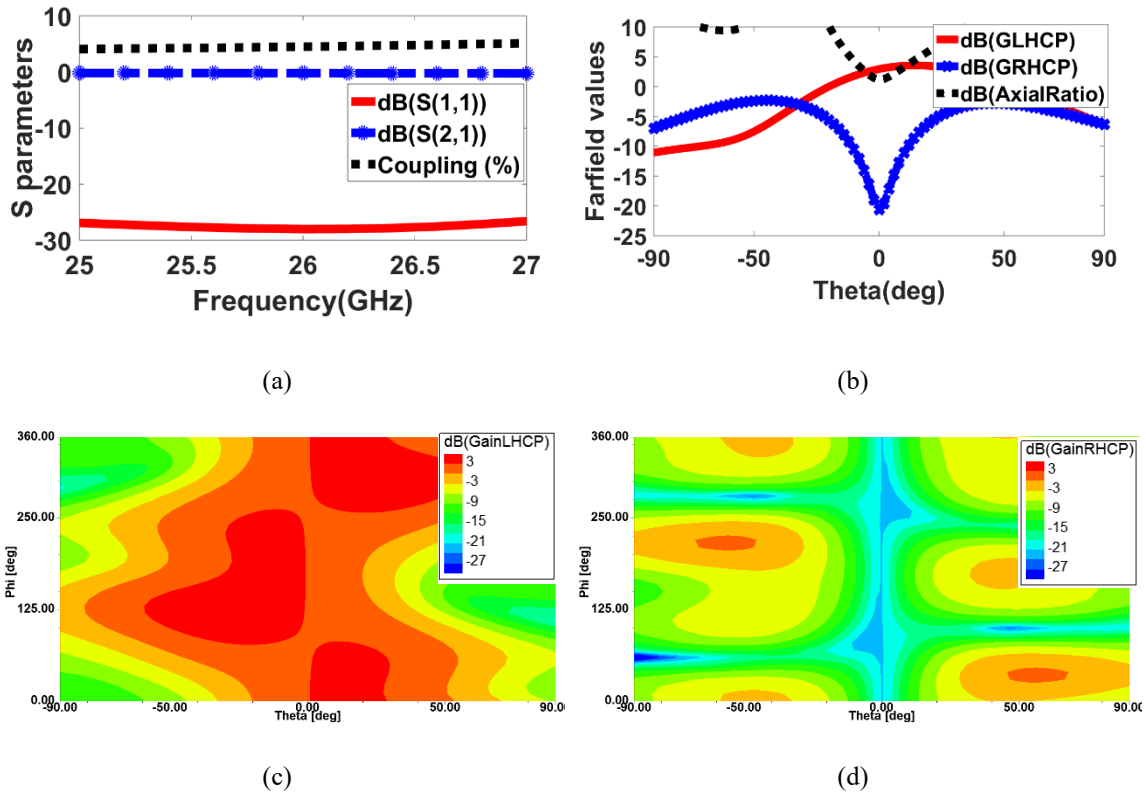

Fig. 5-5 Scattering parameters and far-field properties for a unit cell with $|S_{21}| = -0.2dB$.

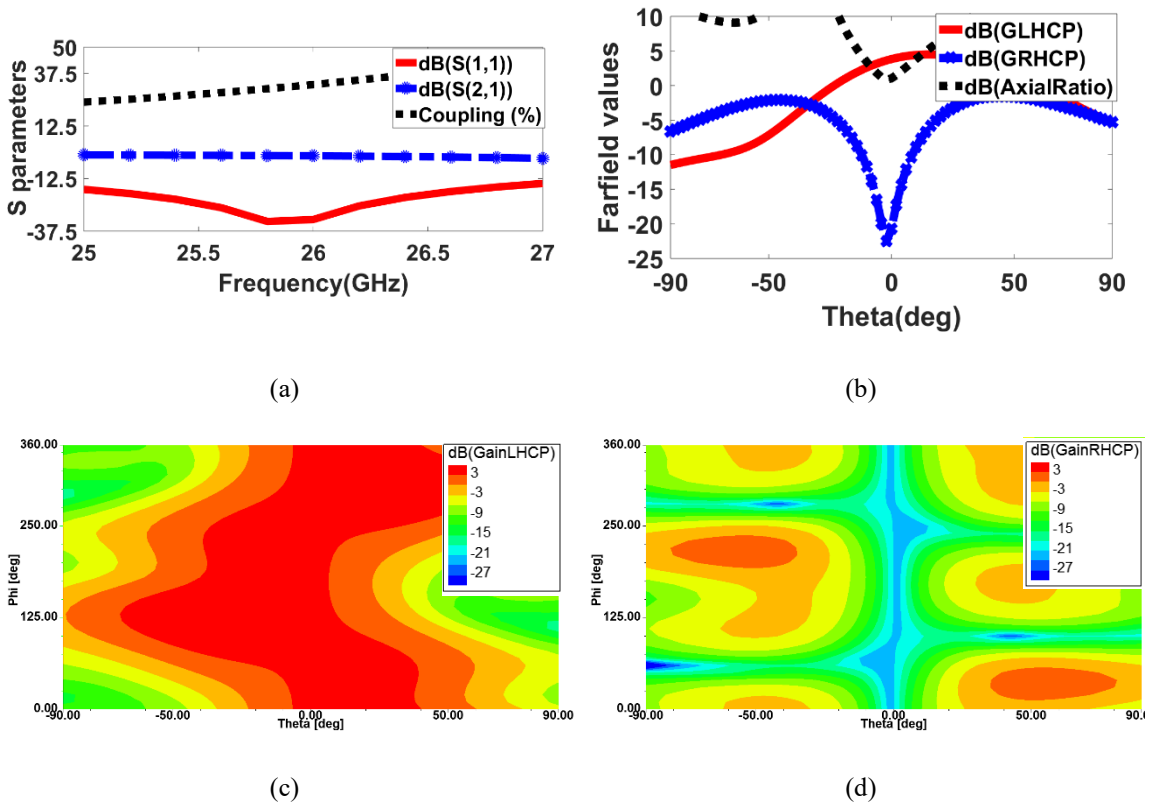

Fig. 5-6 Scattering parameters and far-field properties for a unit cell with $|S_{21}| = -1.68dB$.

It is observed that the $|S_{21}|$ value corresponds to the required coupling factor and unit cell has preserved a perfect circularly polarized radiation around the broadside direction. We aim for the $|S_{11}|$ values to be as small as possible (preferably below -30 dB) so that in the linear array structure, the sum of the partial reflections from the slots and posts does not ruin the input matching of the antenna. Also a reflection-less element means the slot element radiator is actually suitable for traveling wave antenna [21] and [56].

However due to limited space available on the narrow wall and the post heights being limited to Rogers standard substrate thicknesses, optimum values for geometry of slot and posts are chosen such that to provide the best performance possible while keeping the design realizable.

Using values S11 and S21 from each row of Table. 5-2, we can determine radiation capability of each isolated unit cell via (5-11).

$$coupling = 1 - |S_{11}|^2 - |S_{21}|^2 \quad (5\text{-}11)$$

Results are depicted in Fig. 5-7 which show that couplings from slots assigned to Tylor distribution of Table. 5-2 take values between 4.3% to 32.02%. More coupling factors could have been obtained if larger slot lengths could be fitted on the narrow wall and post heights were not limited to standard substrate thickness from Rogers.

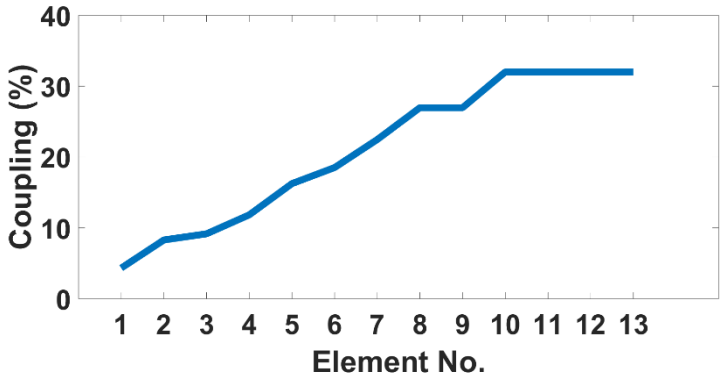

Fig. 5-7 Percentage of coupling from each isolated individual unitcell according to S-parameters given in Table. 5-2.

5.4 Waveguide Slot Antenna

A 13-element array is designed in a 25-26 GHz band. The slots are paired in each element to achieve circular polarization. The slot array depicted in Fig. 5-8 was simulated with HFSS and the results are given in Fig. 5-9 and Fig. 5-10. Good matching and efficiency are observed. The far-field pattern reveals axial ratio of 1.5 dB around the broadside where the main beam points and the Co polarized (LHCP) gain is 14.5 dB. Near E-field distribution on top surface of the antenna can be seen in Fig. 5-11 which reveals good approximation of Taylor aperture distribution.

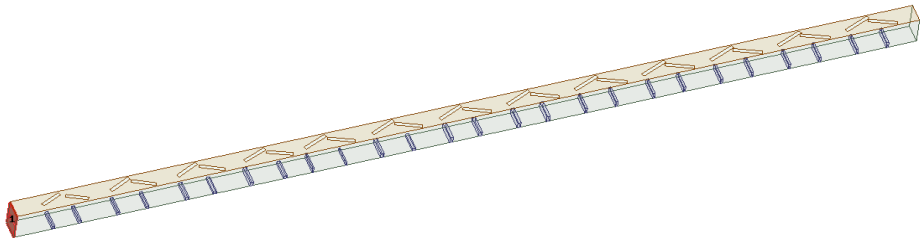

(a)

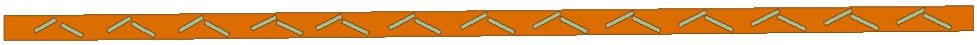

(b)

Fig. 5-8 13 element linear slot array (a) 3D view with posts (b) top view with slots.

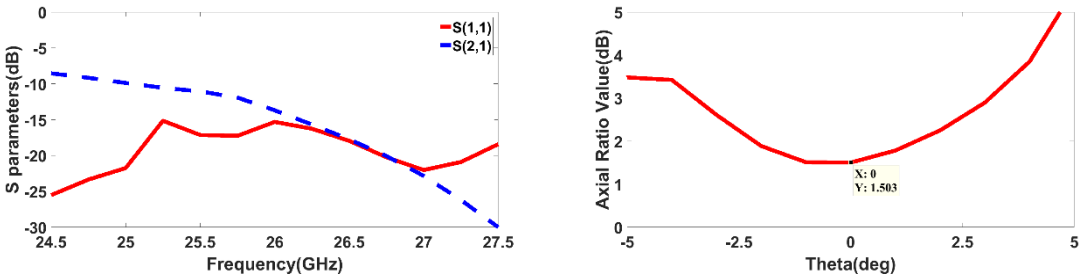

(a) (b)

Fig. 5-9 Result for 13 element linear slot array (a) Scattering parameters over frequency (b) Axial ratio.

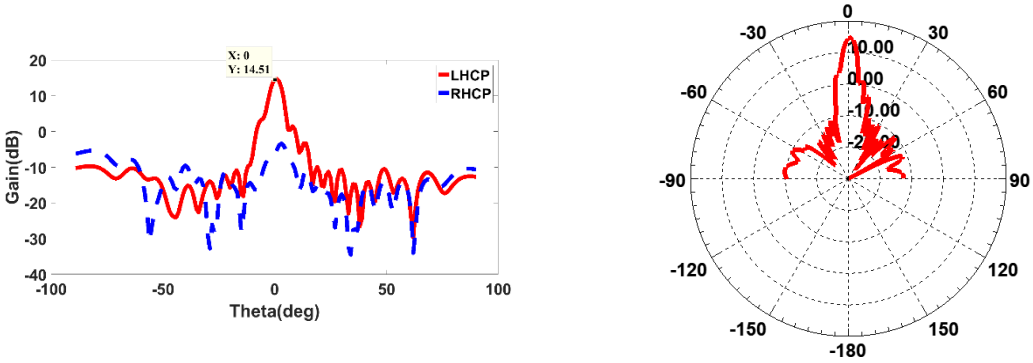

(a) (b)

Fig. 5-10 Result for 13 element linear slot array (a) Co (LHCP) and Cross (RHCP) Gains (b) Co-polarized radiation pattern.

(a)

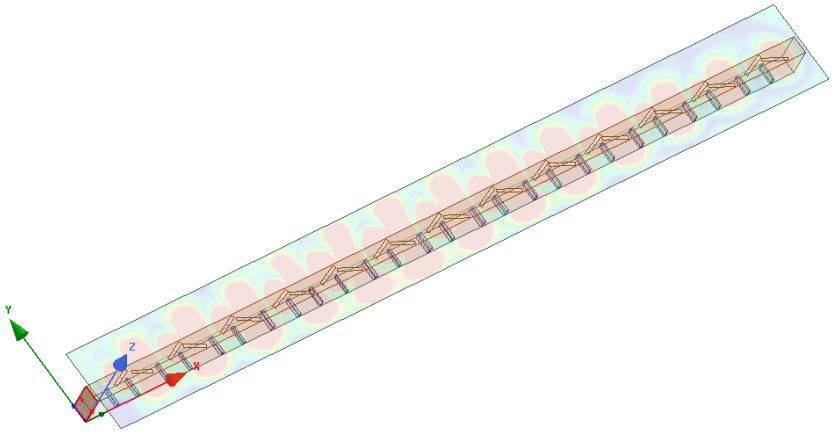

(b)

Fig. 5-11 Near E field distribution (a)Magnitude of total E field at distance z=0.1λ_o above the antenna (b) E field distribution with respect to orientation of slots and input port.

As described in section 5.2, once the array is designed, the residual power at the end is given by $rP = |S_{21}|^2$. According to Fig. 5-9 (a), at 26 GHz, value of $S_{21} \cong -14dB$ hence $rP = |S_{21}|^2 = 0.0398$. Now subtracting this 3.98% from P_{in}, we can find the sum of radiated power from all elements in the array as follows.

$$\sum_{k=1}^{13} P_k = P_{in}(1 - rP)=0.9602 \qquad (5\text{-}12)$$

which is very close to the sum of radiated powers obtained through (5-9) and plotted in Fig. 5-3 (with the assumption that $S_{21}^{(n)} = T^{(n)}$). The unnormalized radiated powers from Fig. 5-3 are listed in Table. 5-3 which give

$$\sum P_k = 0.9582 \qquad (5\text{-}13)$$

Table. 5-3 Radiated powers from each unit cell according to Taylor distribution of Fig. 5-3

Cell No.	1	2	3	4	5	6	7	8	9	10	11	12	13
P_k	0.045	0.08	0.0807	0.0945	0.115	0.109	0.106	0.099	0.073	0.063	0.042	0.029	0.019

However even ignoring the values of dielectric and metallic loss, the actual value of efficiency is lower than (5-12) and (5-13) as the assumption in these formulas is that the unit cells are perfectly reflection-less and ignoring mutual coupling and considering $S_{21}^{(n)} = T^{(n)}$ means that only energy in the forward direction is considered in the array. If we include the reflected power in the array, then at 26 GHz according to Fig. 5-9 (a), efficiency is given by $1 - |S_{11}|^2 - |S_{21}|^2 = 92.86\%$ which as expected is lower than what estimated by (5-12) and (5-13).

5.5 Feeding Technique

Various transitions for feeding slot array rectangular waveguide have been reported in the literature however they are mostly focused on broad wall slot antennas. For narrow-wall slot antenna however, the feeding is more challenging and, the most common practice is the use of another waveguide as in [21], [57] and [58]. Fig. 5-12 illustrates an example of a waveguide planar array and a feeding waveguide where the antenna input is located at the center of the feeding waveguide and radiating waveguides are connected on the broad wall of the feeding waveguide. Feeding happens through a cascade of T junction power dividers. The amount of energy radiated into each waveguide is controlled by the

dimension of the coupling window. This method usually requires a metal post on the opposite side of the window to cancel out reflections and provides large coupling into the radiating waveguides. Post height and offset from the center of the window are adjusted to obtain the required matching [21].

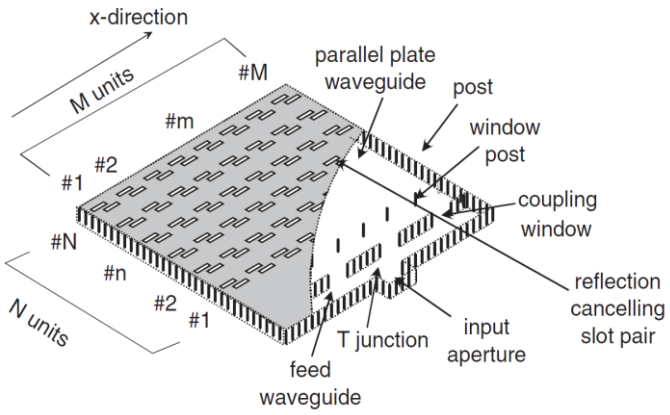

Fig. 5-12 Configuration of a feed waveguide, Tjunctions and window posts to feed a planar slot array. Courtesy of [57]

One difficulty with this method is that several components must be designed and assembled including a multiple-way power divider and a series of reflection cancelling elements such as reflection cancelling slot pairs and inductive posts to suppress the energy accumulated at the input port due to reflections from slots. This will make the fabrication process challenging.

To void such difficulties, we have used a stripline-CPW transition to feed the narrow-wall slotted waveguide antenna array. Among various planar transmission lines used to feed different types of circuits and components at the microwave and millimeter-wave bands, striplines have attractive features such as small radiation loss due to their shielded structure [59]. Furthermore, since we have a multilayer structure, stripline is a promising choice to ensure good isolation between adjacent layers.

5.5.1 Configuration and design

Fig. 5-13 shows the configuration of a back to back stripline to waveguide transition. It consists of a stripline with a U-shaped probe inserted into the broad wall of the waveguide.

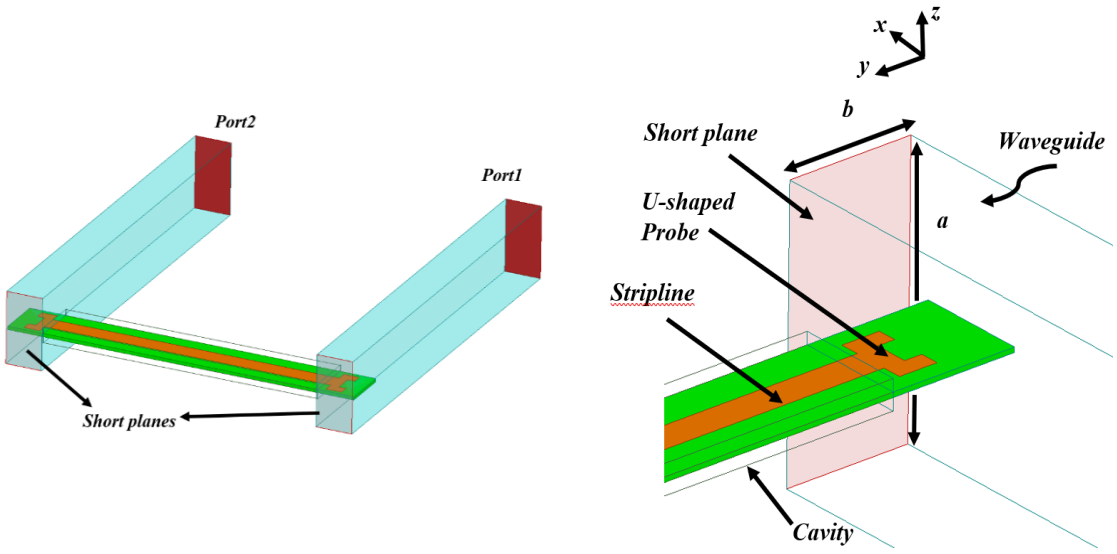

(a) (b)

Fig. 5-13 Configration of a back to back stripline to waveguide transition (b) Closer view of the suspended stripline and U-shaped probe inserted into the broad wall of the waveguide.

Waveguides are terminated with wave ports at one end and short plane at the other end. The probe is located approximately a quarter wave away from waveguide short plane so that the fields reflected off the probe and propagating in the backward direction, will be reflected back from the short plane and added up in phase with the forward traveling wave.

Critical parameters to guarantee perfect transmission and zero reflection, are the probe distance from the waveguide short plane, probe shape, probe height and insertion distance of the stripline probe into the waveguide as indicated in Fig. 5-14 (a) These parameters are optimized to achieve a perfect matching over the desired band of frequency.

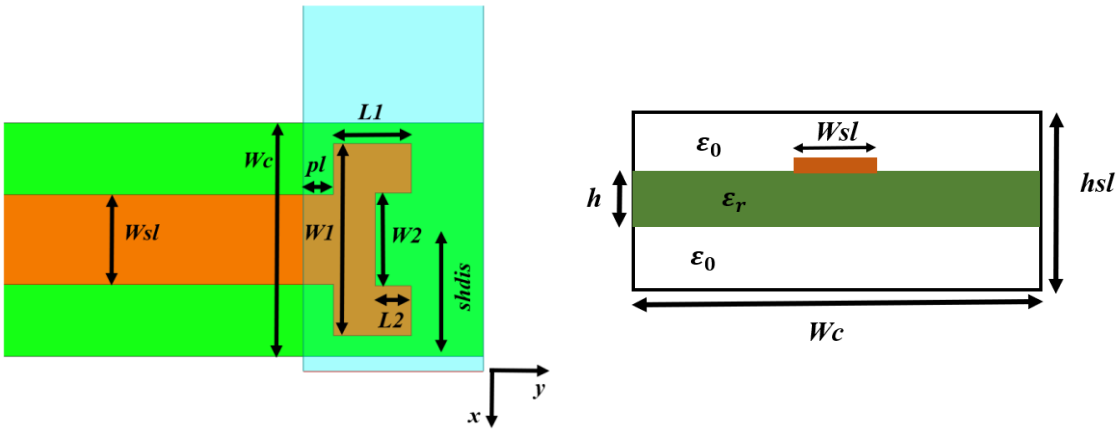

(a) (b)

Fig. 5-14(a) Top view of the feed with suspended stripline and U-shaped probe dimensions. Parameter shdis shows the distance from center of the line to the waveguide short plane and Wc is the width of the cavity. (b) Cross sectional view of suspended stripline. The width and height of cavity are Wc and hsl respectively.

The substrate chosen is RTDuroid 5880 with $\varepsilon_r = 2.2$ and thickness of 0.254 mm. To avoid propagation of higher order modes empirical formulas are available that relate cutoff frequency of quasi-TEM mode of the stripline to the physical dimensions of the cavity (stripline channel) [60] and [61]. The cutoff frequency to guarantee single mode (quasi-TEM) propagation in the stripline is given by

$$fc = \frac{c}{2Wc}\sqrt{1 - \frac{h(\varepsilon_r - 1)}{hsl\ \varepsilon_r}} \qquad (5\text{-}14)$$

where *Wc* and *hsl* are the width and height of the stripline channel, ε_r is the dielectric constant, *c* is the velocity of light and *h* is the substrate thickness.

Also for a given desired characteristic impedance of Z_o, appropriate width of the suspended stripline can be obtained using the formulas below [62].

$$\frac{Wsl}{hsl} = (Aexp\left(1.77245\frac{CZ_o}{120}\right) + Bexp(-1.77245\frac{DZ_o}{120}))^{-1} \qquad (5\text{-}15)$$

where for $\varepsilon_r = 2.2$ parameters A, B, C and D are given by

$$A = 0.0854(\frac{Wc}{hsl})^{-3} + 0.2901\left(\frac{h}{hsl}\right) + 0.2342 \quad (5\text{-}16)$$

$$B = -1.2083\ln\left(\frac{Wc}{hsl}\right) - 0.3796\ln\left(\frac{h}{hsl}\right) + 0.1370 \quad (5\text{-}17)$$

$$C = 1.446$$

$$D = 2.010 \quad (5\text{-}18)$$

Using the above formulas and tuning in HFSS the optimum dimensions of the stripline, U-shaped patch and cavity are obtained for the best performance. The final values of the probe parameters are given in Table. 5-4.

Table. 5-4 Optimum dimensions of the waveguide-stripline back to back transition. Dimensions are in mm.

a	*b*	*pl*	*shdis*	*Wc*	*hsl*	*Wsl*	*L1*	*L2*	*W1*	*W2*
5.72	3	0.5	2.2	4.2	1.2	1.5	1.3	0.6	3.2	1.55

The transition of the quasi-TEM wave in the stripline to TE10 mode in the waveguide is shown in Fig. 5-15 which proves perfect transmission and zero reflection.

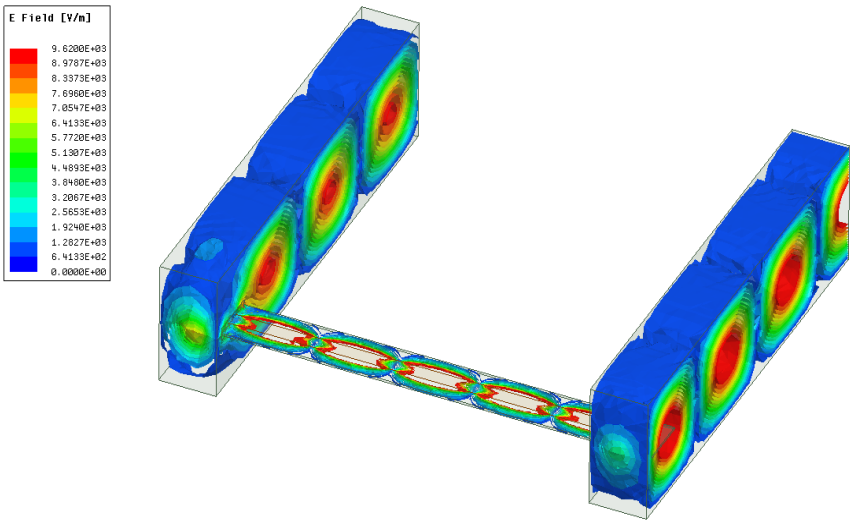

Fig. 5-15 E field plot in the waveguide stripline transition.

Plot of scattering parameters shows the back to back structure of stripline-waveguide proposed here can achieve $|S_{11}|$ of -32 dB and $|S_{21}|$ of -0.29 dB at the desired frequency of 26 GHz. Furthermore, the return loss is better that -10 dB while maximum insertion loss is 0.6 dB over the entire frequency band of 24 GHz-30 GHz.

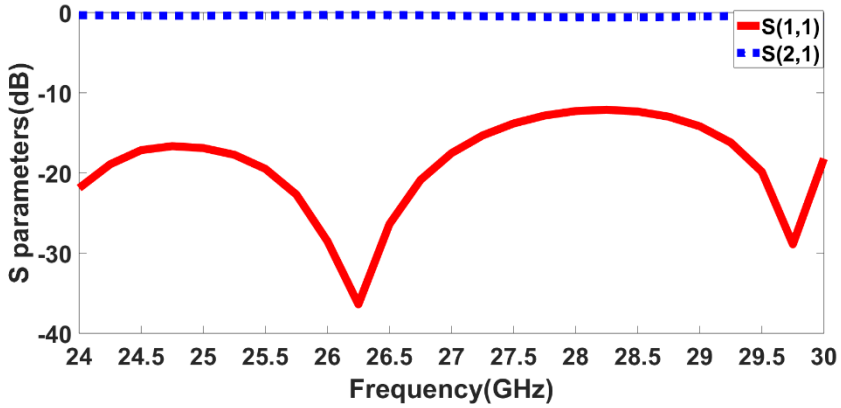

Fig. 5-16 Return loss and insertion loss of the proposed waveguide to stripline transition.

If wider bandwidths are desired for the transition, a meandered or fractal shaped probe (instead of a U-shaped probe) can be used. This will increase the current traveling along the edges and helps to achieve wider band widths.

5.5.2 Back to back feeding system

To access the internal stripline from output terminals of the antenna, we use a stripline-CBCPW transition. The cross-sectional view of this transition is depicted in Fig. 5-17. It can be seen that a metalized via (probe) is used to transfer the signal from stripline to the conductor-backed coplanar waveguide (CBCPW) line on the upper surface. Some parasitic vias had to be arranged around the probe to help with smooth field transition between layers. These vias can be observed in Fig. 5-18 where a closer view of the feed and cavity are depicted from the top.

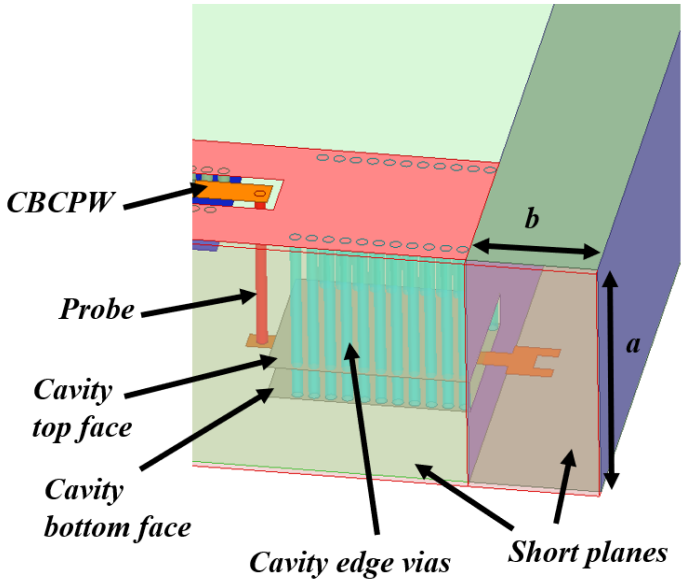

Fig. 5-17 Cross section of the stripline to conductor-backed CPW transition.

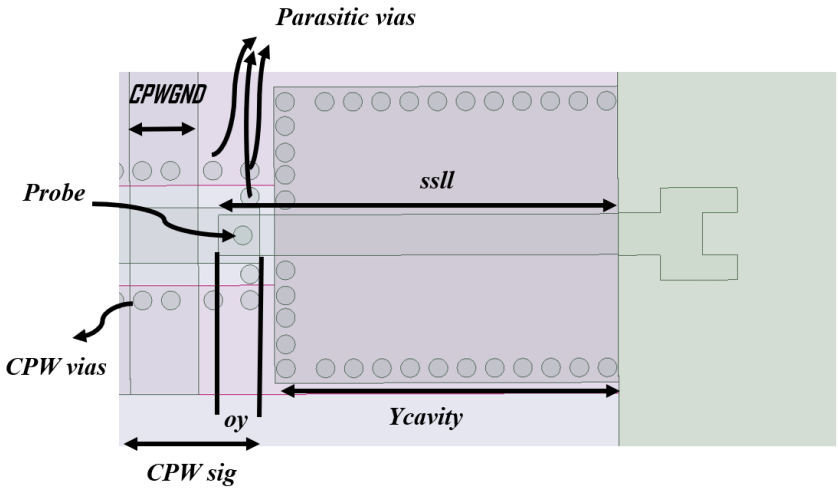

Fig. 5-18 Top view of the stripline to conductor-backed CPW transition with parasitic vias. Parameter CPWGND is indicated with capital letters to identify the CPW ground plane in the 2nd layer.

Next step is to taper the CPW line to be connected to the SMP connector. This transition is illustrated in Fig. 5-19.

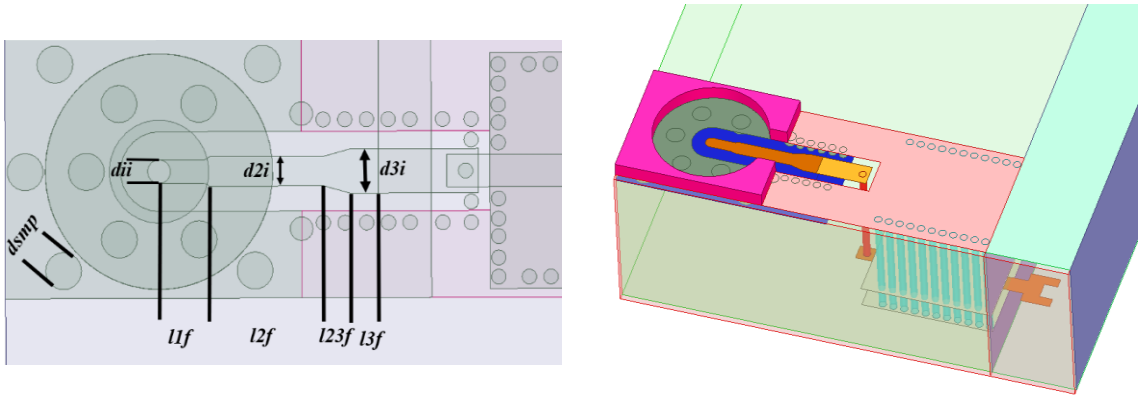

(a) (b)

Fig. 5-19 CBCPW transition to SMP connector (a) Top view (b) 3D view only SMP guard is shown and the external and internal conductors are made invisible for better clarification of the transition.

The dimensions of the SMP connector are taken from data sheet of 0853050232 by Molex which works perfectly for frequency range of 26 GHz. The structure of SMP connector and its scattering results are illustrated in Fig. 5-20 and Fig. 5-21 respectively.

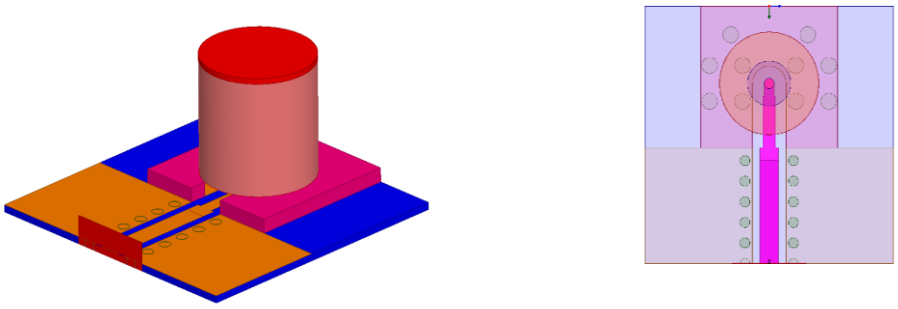

(a) (b)

Fig. 5-20 (a) 3D model and (b) Top view of the SMP connector and CPW transition.

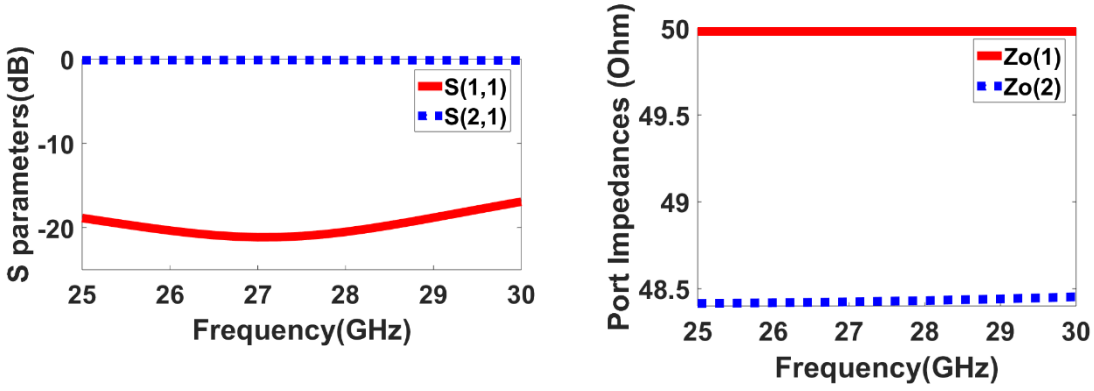

(a) (b)

Fig. 5-21 (a) Scattering parameters for a CPW-SMP transition. (b) Port impedances.

To implement this entire feeding in the antenna structure, we start off by first trying to feed a waveguide using this feeding configuration as depicted in Fig. 5-22. Dimensions of the proposed back to back feed structure are given in Table. 5-5.

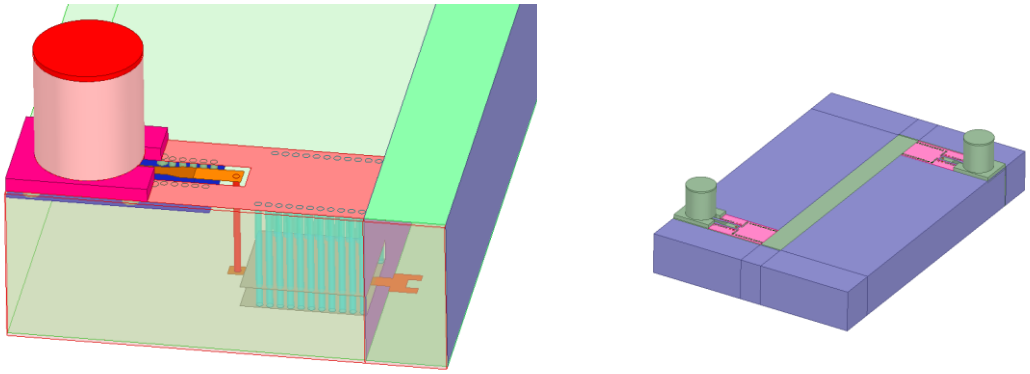

(a) (b)

Fig. 5-22 (a) The entire transition from stripline to external SMP connector (b) Back to back feeding of a waveguide using the transition in (a) on both ends.

Table. 5-5 Optimum parameters of the feed section for stripline to CBCPW and SMP connector. All values are in mm.

pl	***shdis***	***Wc***	***hsl***	***Wsl***	***L1***	***L2***	***W1***	***W2***	***ssll***	***Ycavity***
0.57	2.24	4	0.76	0.55	1.04	0.47	1.24	0.57	5.4	4.64
CPWsig	***CPWGND***	***oy***	***d3i***	***d2i***	***dii***	***dsmp***	***l1f***	***l2f***	***l3f***	***l23f***
1.75	0.925	0.554	0.75	0.5	0.4	0.63	0.8	2	0.5	0.46

Fig. 5-23 shows that a bandwidth of 10% is obtained for return loss smaller than 10dB. The average insertion loss over the frequency band is 1.35dB.

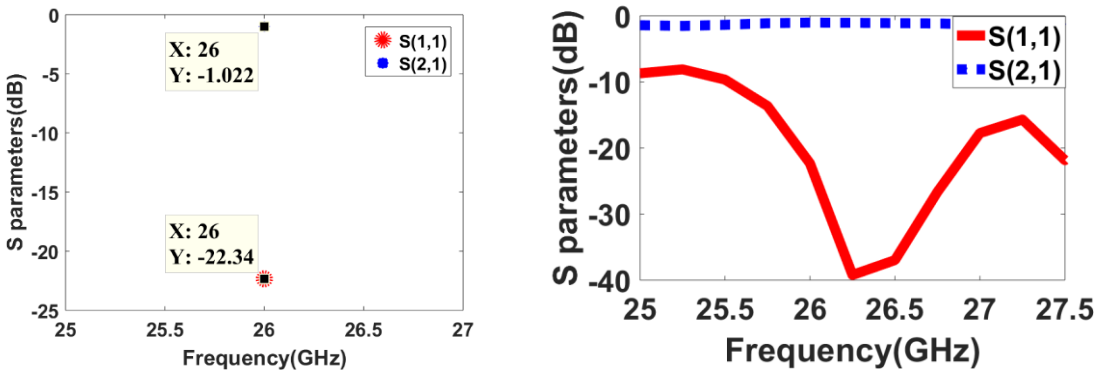

(a) (b)

Fig. 5-23 (a) Scattering parameters at the frequency of 26 GHz (b) Return loss and insertion loss over the frequency.

5.6 Feed and Antenna Structure

Configuration of antenna with feeding system connected to it is given in Fig. 5-24. It should be noted that although feed and antenna separately showed good performance, once connected together, meeting requirements for good matching and far-field characteristics from the entire structure proves to be a more challenging task.

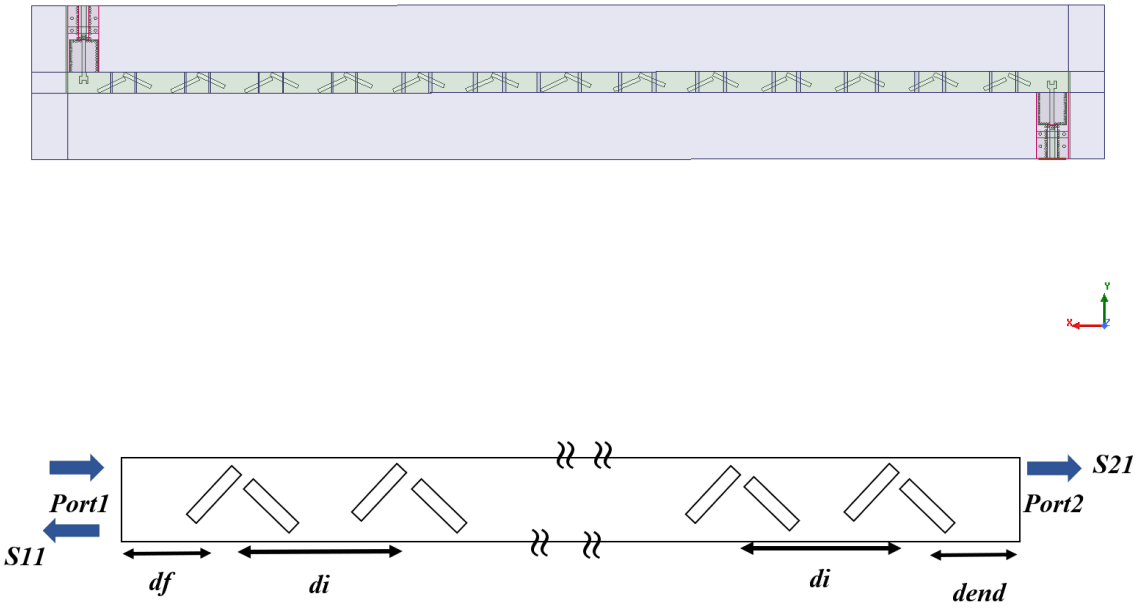

Fig. 5-24 Top view of the slot antenna with feed system connected on both ends.

A few key parameters playing an important role in antenna matching and AR in the configuration of Fig. 5-24 are height of the feeding probe (*hsl*) and parasitic vias (*hpar, hpar1*) along with the distance of feed from the first and last elements on each end of the array, namely *df* and *dend*. In order to find optimum values for these parameters and to understand how each of these factors could affect the final performance of the antenna, a few parametric studies are carried out. Some examples are given below.

Starting off with constant values of *hsl=1.8 mm, hpar=2.5 mm,* and *hpar1=1.5 mm,* we conduct a parametric sweep on *df* and *dend* values over the range of

$$3.8\,mm < df < 10.8\,mm$$

$$6.8\,mm < dend < 7.8\,mm$$

In another parametric study, *hsl=1.8 mm, df=6.5mm,* and *dend=8.9mm* are taken as constant values and height of parasitic vias are varied as follows

$$1.5\,mm < hpar < 2.3\,mm$$

$$0.65\ mm < hpar1 < 1.3\ mm$$

In all parametric studies, matching, axial ratio at broadside and average axial ratio over $-6 < \theta < 4$ were studied in order to find which set of parameters is given the best results. Ideally it is enough to have good CP in the 3 dB beamwidth of the antenna however the angular region selected here ($-6 < \theta < 4$) is considered slightly wider than 3 dB beamwidth to account for inaccuracies that might shift the main beam from broadside and consequently alter the 3 dB beamwidth. In order to decide on a set with best possible values of $|S_{11}|$, AR and Avg_AR, an error function must be created to take into account all of these parameters. Individual and total error functions are formulated as follows

$$\epsilon_{Total} = \sum_{i=1}^{N=4} w_i \epsilon_i$$

Where

$$\epsilon_1 = ||S_{11}| - |S_{11desired}||^2$$

$$\epsilon_2 = ||S_{21}| - |S_{21desired}||^2$$

$$\epsilon_3 = |AR(\theta = 0, \varphi = 0) - AR_{desired}(\theta = 0, \varphi = 0)|^2$$

$$\epsilon_4 = |Avg\_AR(-6 < \theta < 4, \varphi = 0) - Avg\_AR_{desired}(-6 < \theta < 4, \varphi = 0)|^2$$

Desired values for matching, insertion loss and axial ratio are chosen as below

$$|S_{11desired}| = |S_{21desired}| = -30\ dB$$

$$AR_{desired} = 0.5\ dB$$

$$Avg_{AR_{desired}} = 1\ dB$$

Values of weight functions are chosen as $w_1 = w_2 = 1$, $w_3 = 0.4$, and $w_5 = 0.5$.

Plots of error function for one example where *hsl=1.8mm, hpar=2.51mm, hpar1=1.54mm, and, dend=6.1 mm* are given in Fig. 5-25. It is clear that best values of *df* which will produce minimum error are found between *7mm to 9mm.*

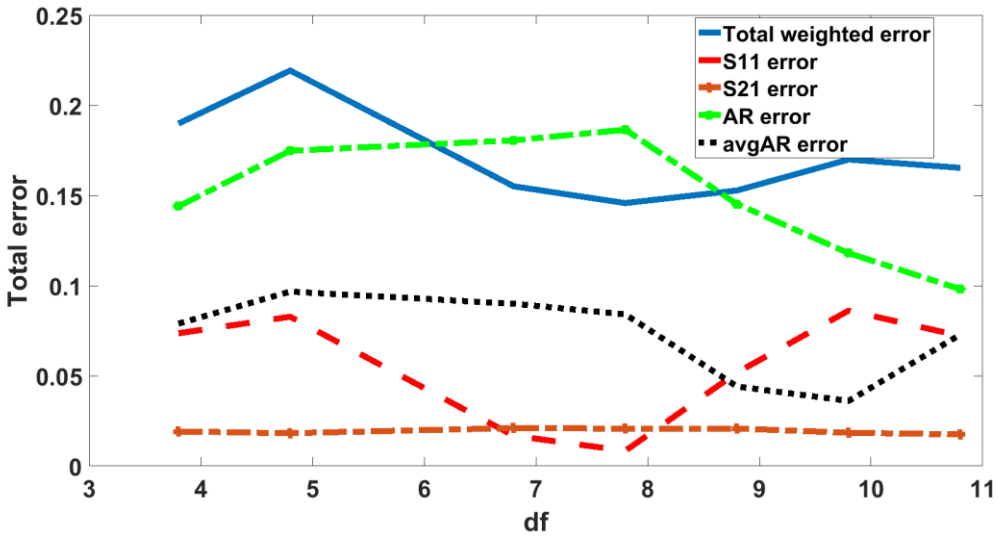

Fig. 5-25 Error functions for S11, S21, AR at broadside, average of AR in 3 dB beamwidth and total error.

This analysis is useful in the sense that it will help to find relation between different geometrical parameters. The way these factors influence the final matching or far-field of an antenna can also be measured through individual and total error functions which will offer appropriate range in which parameters can change and produce promising results.

This is useful for the next stage of the design where many parameters need to be varied simultaneously and it can produce effective accurate results and fast convergence for a multi-goal optimization process where finding an optimum solution could be very challenging.

In the next step parameters *df, dend, hsl, hpar* and *hpar1* are optimized and tuned using HFSS in order to provide smooth field transformation from Quasi TEM to TE10 mode and also, to cancel out all the reflections from the slots in the antenna. The Quasi Newton (Gradient) optimization method from HFSS optimizer is chosen.

Since we had some success with the set $hsl = 1.8\ mm, hpar = 2.5\ mm, hpar1 = 1.5\ mm$, in initial stages of design, now for the first round of optimization of feed connected to the slot antenna, we chose *hsl* to be equal to a constant value of 1.8 mm. The rest of the parameters *df, dend, hpar* and *hpar1* are varied within the ranges specified below.

$$1.8\ mm \leq hpar \leq 2.5\ mm$$

$$1\ mm \leq hpar1 \leq 1.5\ mm$$

$$6.8\ mm \leq df \leq 10.8\ mm$$

$$6.1\ mm \leq dend \leq 7.1\ mm$$

In order to speed up the convergence process, we let the optimization to choose parameters from a pool of 40 best initial values created through a parameter study. The optimizer is set up to minimize a multi-goal cost function as below

$$|S_{11}| < -15\ dB$$

$$|S_{21}| < -15\ dB$$

$$AR(\theta = 0, \varphi = 0) < 2\ dB$$

$$AR(\theta = -2, \theta = 3, \varphi = 0) < 3\ dB$$

This will guarantee that both S-parameters and far-field requirement will be met. The final cost function after 96 iterations is given below.

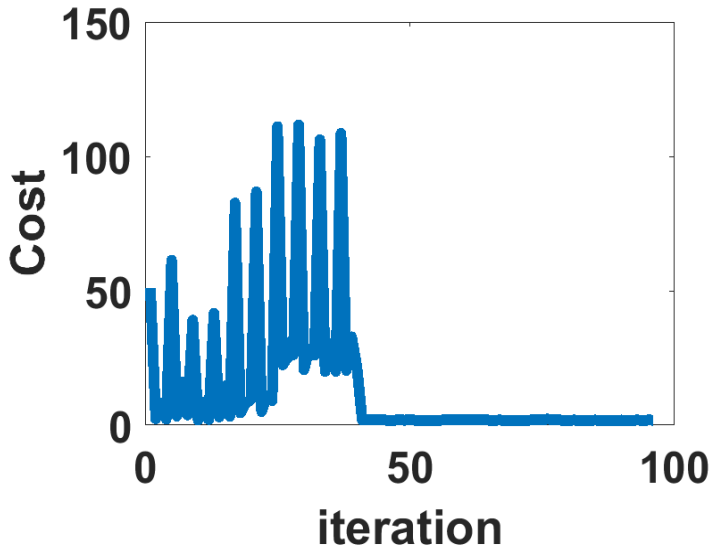

Fig. 5-26 Cost function for optimizing both S-parameters and axial ratio of antenna for hsl=1.8mm constant and, hpar, hpar1, df and dend variables.

Results of the above optimization will give us some insight on the relation between parameters. This will help to discover some rules to better estimate the range of desired values.

- It was observed that *df* values greater than 8.8 mm, did not give any good results.
- For every given value of *df, hpar*, and *hpar1*, parameter *dend=6.1 mm* proved to produce better results than *dend=7.1 mm.*
- Another useful lesson learned from the above optimization was that while $hpar \leq hsl$, cost function is maximum whereas for $hpar > hsl$ we start to see a huge drop in cost function values.
- Also, for constant values of *hsl* and $hpar > hsl$, values of $hpar1 \geq 0.6\ hpar$ usually offer better cost values.

Knowing all this, the second optimization is set with the following values

$$hsl = 2.8\ mm \quad const.$$

$$dend = 6.1\ mm \quad const.$$

$$6.8\ mm < df < 8.8\ mm$$

$$3.2\ mm < hpar < 4\ mm$$

$$2.5\ mm < hpar1 < 3\ mm$$

Optimizer was set to meet the following requirements

$$|S_{11}| < -15\ dB$$

$$|S_{21}| < -15\ dB$$

$$AR(\theta = 0, \varphi = 0) < 2.5\ dB$$

$$AR(\theta = -2, \theta = 3, \varphi = 0) < 3\ dB$$

Optimization is converged faster than the previous time. The results can be seen in the figure below.

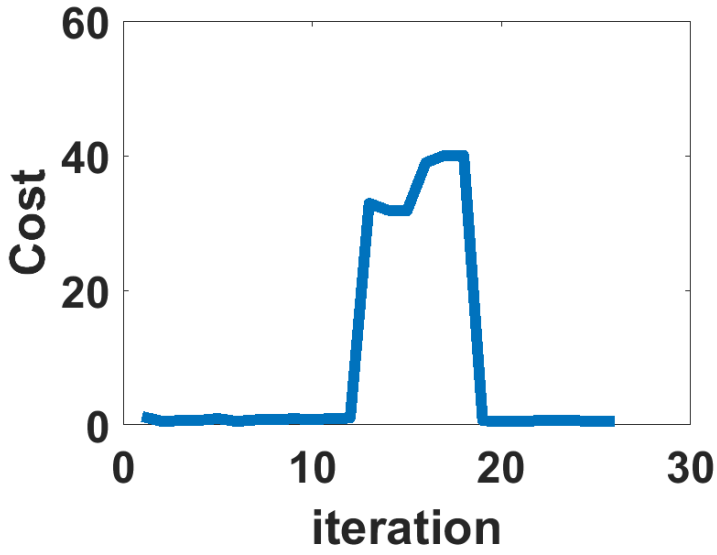

Fig. 5-27 Cost function for optimizing both S-parameters and axial ratio of antenna for hsl=2.8 mm and dend=6.1 mm constants and, hpar, hpar1, and df variables.

From this optimization, we have found some great candidates with almost zero cost function meeting the requirement on both pattern and scattering parameters. Result of this optimization ruled out $df > 7.8mm$ to be effective in producing minimum cost function values. For the final optimization we have changed the value of *hsl* one more time and decided to calculate the cost function for the following set of parameters.

$$hsl = 3.8\,mm \;\; const.$$

$$dend = 6.1\,mm \;\; const.$$

$$6.8\,mm < df < 7.8\,mm$$

$$4.4\,mm < hpar < 5.2\,mm$$

$$3.5\,mm < hpar1 < 4\,mm$$

Fig. 5-28 illustrates the results.

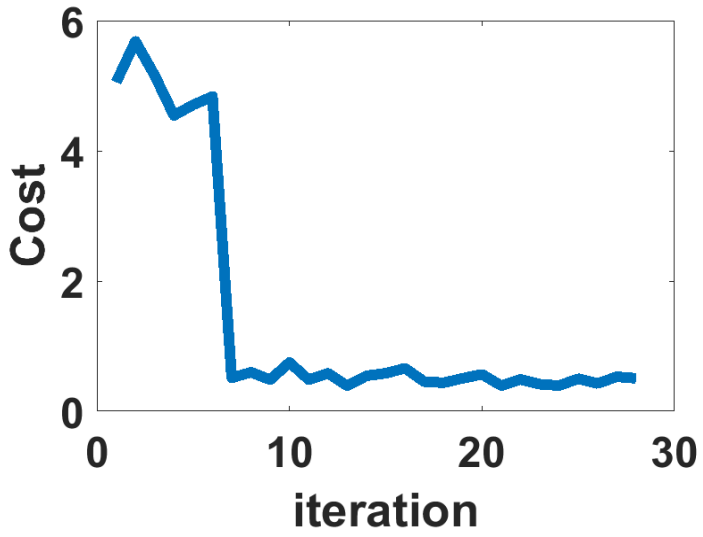

Fig. 5-28 Cost function for optimizing both S-parameters and axial ratio of antenna for hsl=3.8 mm , and dend =6.1 mm constants and, hpar, hpar1 and df variables.

Fig. 5-29 shows the scattering parameters and far-field plots for the best candidate obtained from the optimization. Maximum co-polarized gain of 13.7 dB is obtained at broadside where the axial ratio is 2.57 dB. Both $|S_{11}|$and $|S_{21}|$ values are below -10 dB over the entire frequency band. These results are obtained with the following parameters.

Table. 5-6 Optimum values of probe and parasitic via heights along with distances from feed sections on both ends of the antenna

df	*hsl*	*hpar*	*hpar1*	*dend*
6.8 mm	2.8 mm	4 mm	3.06 mm	6.1 mm

It is worth mentioning that $hsl = 2.8\,mm \approx a/2$ where the E field in the waveguide is maximum and best matching could be obtained if the rest of the parameters are designed accordingly.

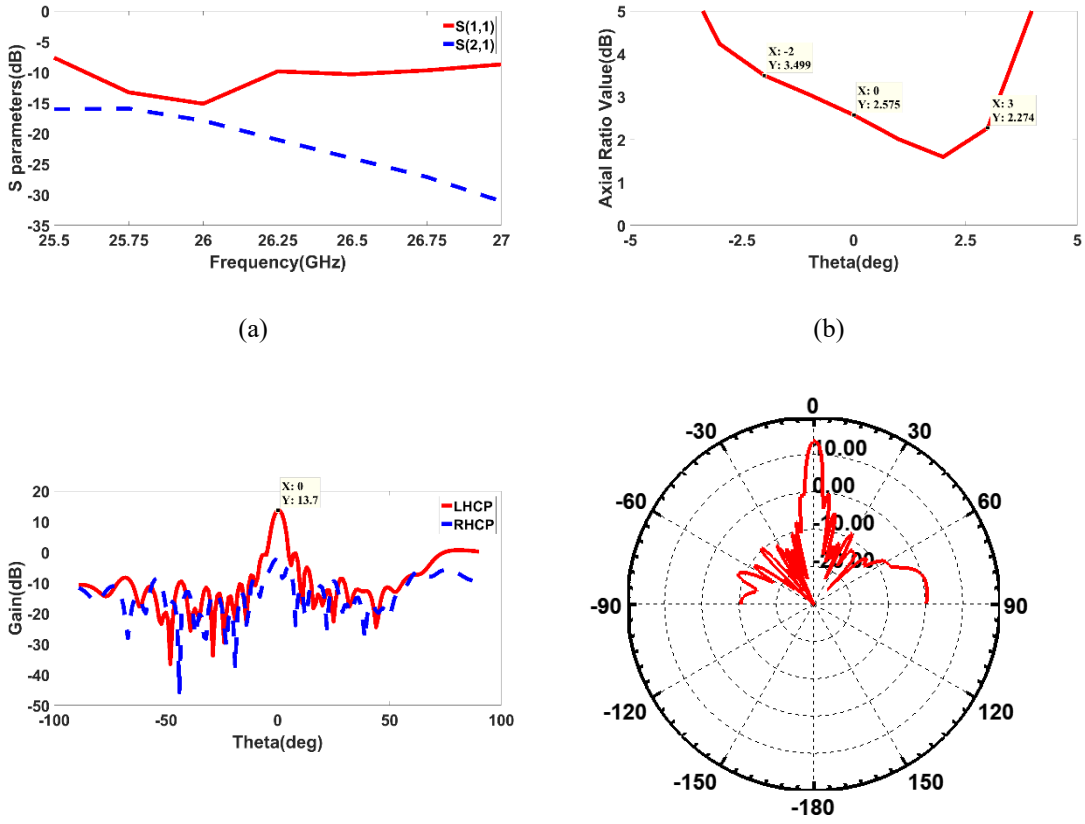

Fig. 5-29 Resultst for 13 element linear slot array and feeding system for optimized values of df=6.8 mm, dend=6.1 mm, hsl=2.8 mm, hpar=4 mm and hpar1=3.06 mm. (a) S-parameters, (b) Axial ratio, (c) Co (LHCP) and Cross (RHCP) Gains (d) Co-polarized radiation pattern.

It can be seen that the optimization goals are mostly met but the results can still be improved. It is partly due to the fact that the optimization goals were set not so strictly ($|S_{11}| < -15\,dB, AR < 2.5\,dB$) in the beginning, and secondly it should be noted that optimized values of slots and posts obtained previously were for a unit cell in an isolated waveguide. Now with the feeding system connected, it is likely that some of the unit cell properties must be redesigned to keep the good performance in this new configuration.

In order to achieve axial ratio and $|S_{11}|$ values better than the marginal (-15 dB and 2.5 dB) values, post offset and height values should be revisited again considering the slot array and feeding system structure as a whole. Optimizations are carried out on post offsets and heights to not only meet the following conditions on antenna scattering and far-field characteristics, but also for posts and via heights to match the standard thickness of Rogers 5880 substrates.

Conditions on S-parameters:

$$|S_{11}| < -15\ dB$$

$$|S_{21}| < -15\ dB$$

Conditions on axial ratio at broadside and axial ratio over 3 dB beamwidth:

$$AR(\theta = 0, \varphi = 0) < 2.5\ dB$$

$$AR(\theta = -2, \theta = 3, \varphi = 0) < 3\ dB$$

Condition on maximum gain at broadside:

$$GainLHCP(\theta = 0, \varphi = 0) > 12\ dB$$

Condition on sidelobe levels:

$$GainLHCP(\theta = 8, \varphi = 0) < 1\ dB$$

$$GainLHCP(\theta = 13, \varphi = 0) < -4\ dB$$

Fig. 5-30 illustrates the convergence process for such optimization.

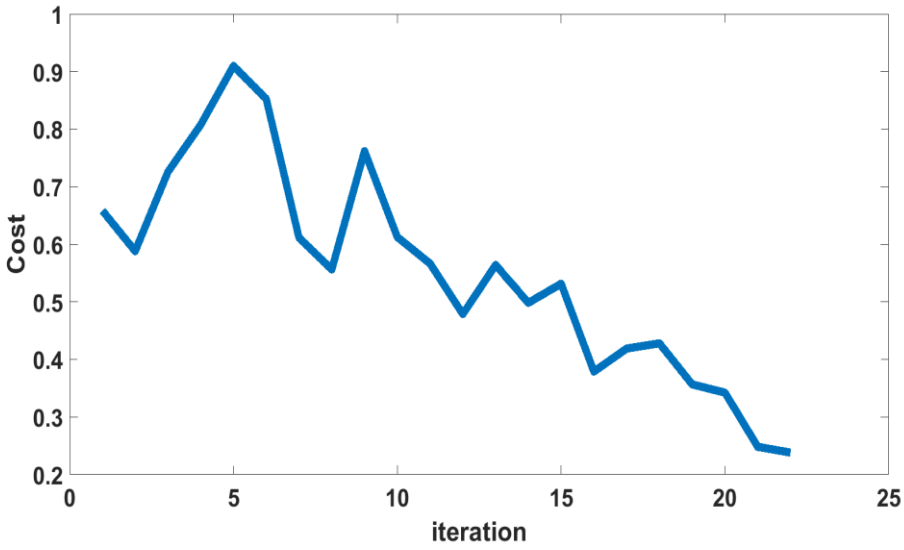

Fig. 5-30 Illustration of convergence results for optimization of antenna-feed configuration

After optimization and manipulation of dielectric boards thickness and arrangements, finally we achieved S-parameters of $|S_{11}| = -40\ dB, |S_{21}| = -15\ dB$, and $AR(\theta = 0, \varphi = 0) = 1.43dB$, and broadside gain of 13.5 dB that can be realized with 10 layer substrates with only three different types of posts with height values of 0.508 mm, 0.889 mm, and 1.14 mm. Far-field and S-parameter results for this antenna are shown in Fig. 5-31 and Fig. 5-32.

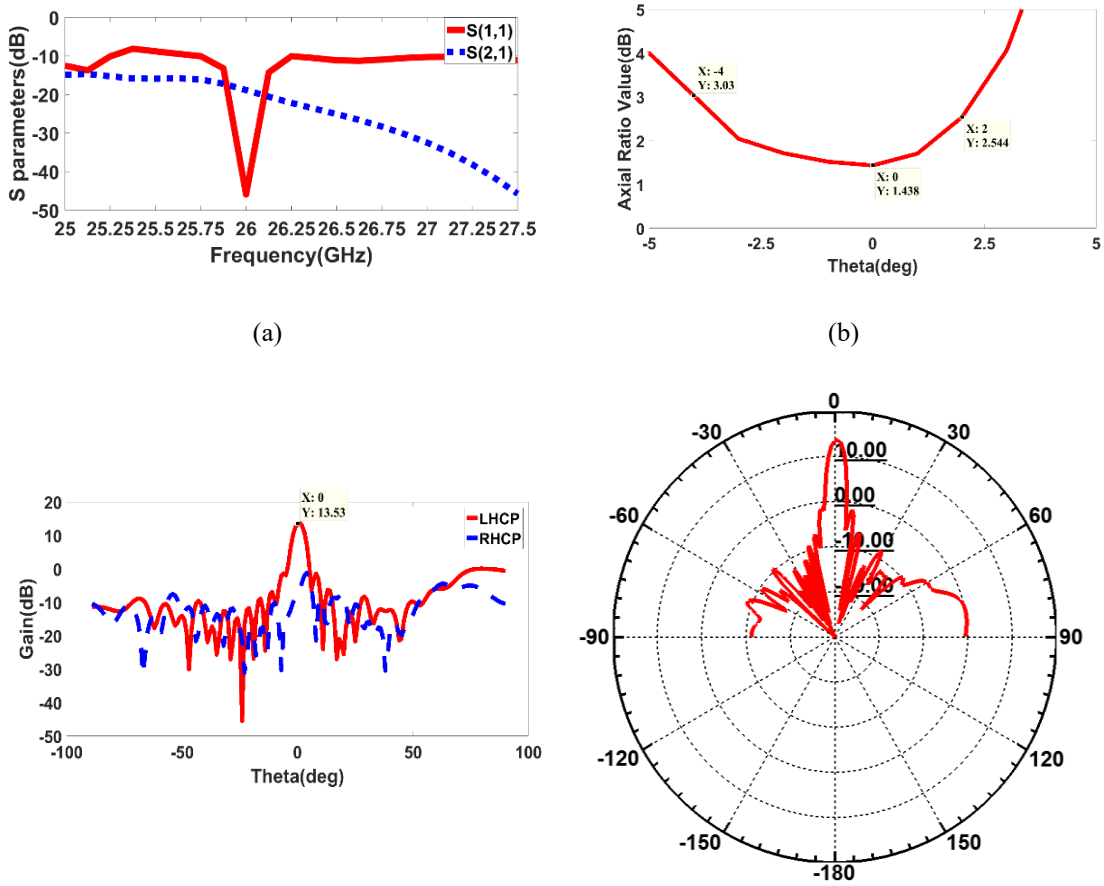

Fig. 5-31 Resultst for 13 element linear slot array and feeding system after optimization of feeding parameters, post offsets and post heights (a) S-parameters, (b) Axial ratio, (c) Co (LHCP) and Cross (RHCP) Gains (d) Co-polarized radiation pattern.

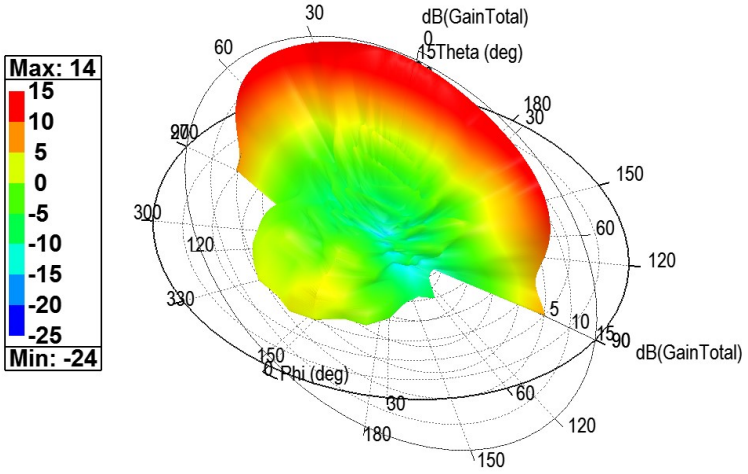

Fig. 5-32 3D pattern of optimized antenna-feed system.

In general, we could not achieve the SLL requirement of -20 dB as stated earlier in chapter 4 due to limited space available on the narrow wall of a dielectric loaded waveguide. However, it is worth to note that even in traditional standing wave design of narrow-wall slot arrays where resonant slots are wrapped around and penetrate both top and bottom broad walls, maximum SLL deviates from the design goal by 5 to 6 dB. To resolve this problem, usually over designing the array with stricter SLL goal, for example -25 dB to achieve -20 dB in practice, is recommended from literature. Literature also suggests that modulating excitation coefficients at the waveguide aperture with the cosine of the tilt angle ($v_{new} = v_k/\cos\theta_k$) could help reduce the difference between maximum achievable SLL and the design goal to the order of 3 to 4 dB. These methods are not pursued here. In the following sections we focus on how to fabricate the above design using the current PCB manufacturing facilities.

5.7 Realization Considerations

5.7.1 Via diameter and bonding films

In previous sections, via diameters and spacing were selected to be 0.254 mm and 0.381 mm respectively. However, considering the possibility that creating a via hole of this

size may be difficult in practice, we have changed the diameter of vias to a more common value of 0.4 mm with spacing of 0.8 mm. Given that most vias are located in the feeding section forming the perturbed cavity around the stripline, and especially at such high frequencies this variation of via size could have a noticeable effect on antenna matching.

Another precaution taken into account was to consider enough offset between edge of the slots and waveguide walls, so width of the narrow wall is increased to 3.36 mm.

Next thing to take into account, is the prepreg layers required for bonding. The bonding film used for RT duroid 5880 is RO3001 with quite similar dielectric constant of 2.28 and thickness 1.5 mil. This will affect the height of probe, parasitic vias and posts to some extent. Post offsets and heights are slightly tuned in order to maintain good performance. New values of heights for probe, parasitic vias and posts are listed in Table. 5-7.

Table. 5-7 New values of posts, probe and parasitic vias height considering the prepreg layers in the design.

hsl	*hpar*	*hpar1*	*hp_Type 1*	*hp_Type2*	*hp_Type3*
2.7555mm	4.0128mm	3.0476mm	0.508mm	0.9271mm	1.0922mm

The design is then updated considering all the above factors and results are given in Fig. 5-33 and Fig. 5-34.

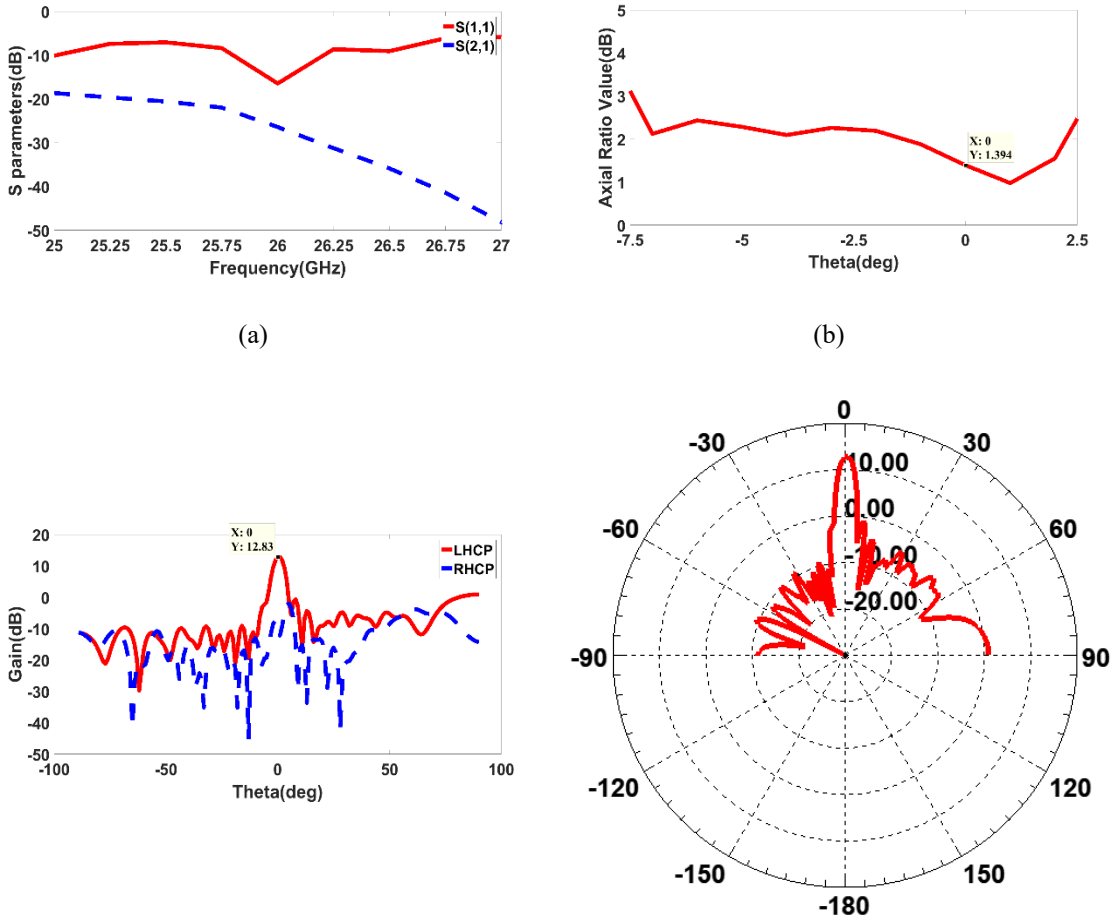

Fig. 5-33 Resultst for 13 element linear slot array and feed system after changing via diameters and considering bonding film between layers (a) S-parameters, (b) Axial ratio, (c) Co (LHCP) and Cross (RHCP) Gains (d) Co-polarized radiation pattern.

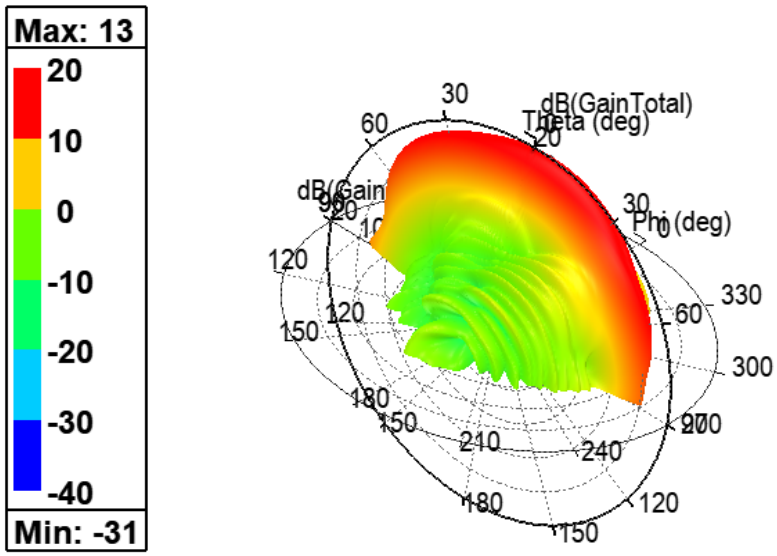

Fig. 5-34 3D pattern of for 13 element linear slot array and feed system after changing via diameters and considering bonding film between layers.

5.7.2 Waveguide wall thickness

In this step, we consider replacing the PEC sheets in simulations with rectangles of 0.7 mm thickness to better model waveguide walls. In practice a router can create a metalized slot of diameter 0.7 mm to imitate the PEC boundary condition on waveguide walls [53]. Such practice is also used to create short planes at waveguide ends and the back of feeding system.

One important thing that must be considered here is that since the antenna is in the middle and surrounded by waveguide walls (metalized slots), in order for the structure not to fall apart as the metalized slots (trenches) cut through the layers, we made sure to have a few gaps between trenches along the length of the structure and also at the corners as can be seen in the following figures. The orange lines show the metalized slots imitating PEC boundary condition on waveguide walls.

In Fig. 5-35(b) the dielectric block has been made invisible so the cross section of gaps in between trenches is better seen.

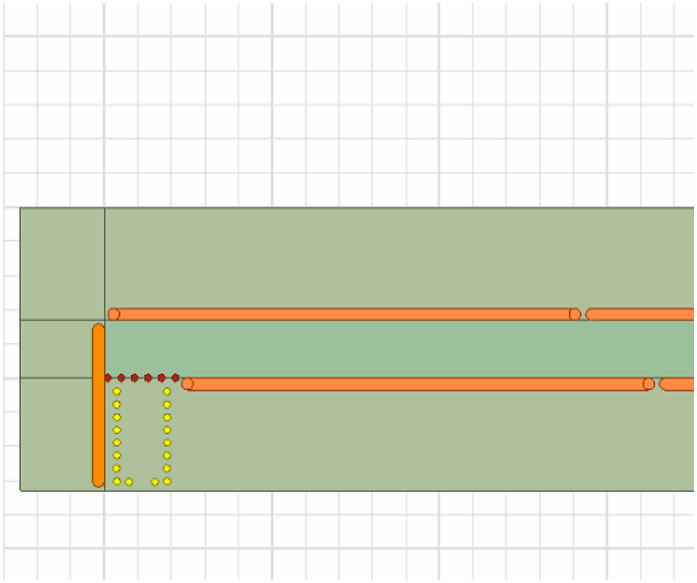

(a)

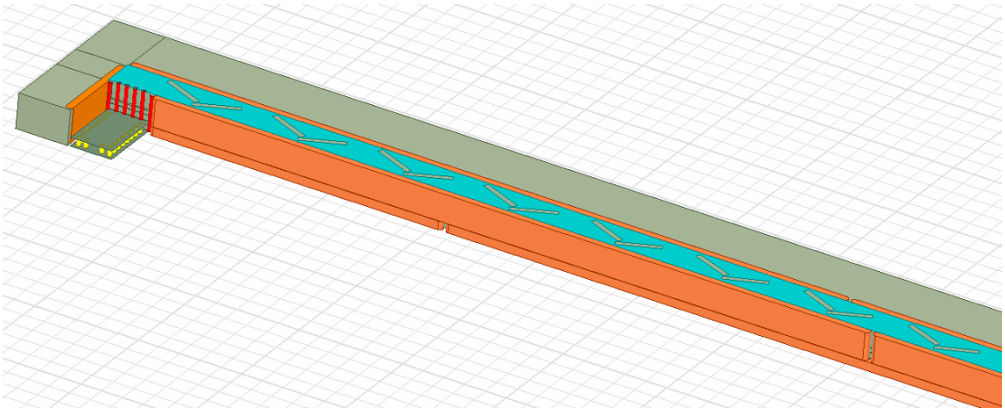

(b)

Fig. 5-35 Illustration of waveguide walls and gaps (a) Top view (b) Cross sectional view.

Location of these gaps and their diameter can impact the input matching. Therefore, a parameter study is conducted to find the best values of gap width and its distance from each end of the antenna.

In determining the best location for gaps, care must be taken so the gap does not fall on the location of any posts along the antenna, as it will ruin the antenna performance as expected.

Also in order to avoid significant perturbation of the PEC boundary conditions on waveguide walls, instead of creating a gap that goes all the way through the structure (*gap height=waveguide width=a*), we decided to have smaller gaps that will only involve a few substrate layers as depicted in Fig. 5-36(b). This guarantees the wall behavior is close enough to that of the PEC boundary condition as the level of perturbation is kept to minimum.

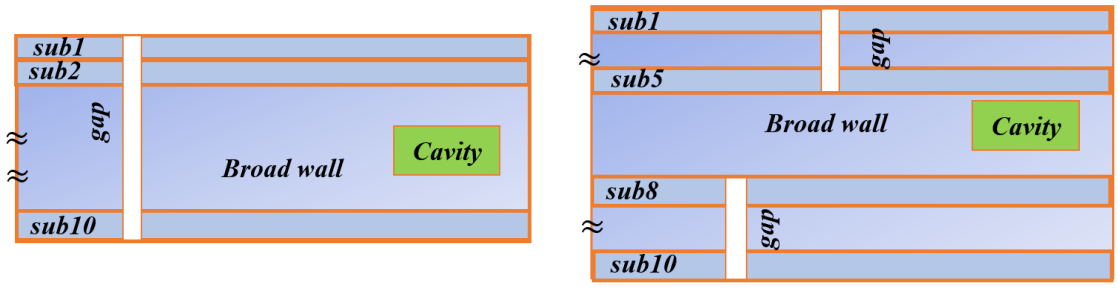

(a) (b)

Fig. 5-36 Illustration of two differeent methods to create gaps in waveguide walls (a) gap all-the-way-through with gap height equal to the waveguide width and (b) Individual gaps in separate layers.

Next step is to create the opening in waveguide walls for the stripline to enter. The perfect window cut out of the PEC walls in the previous stages of the design, is now replaced with two sets of vias going between layers 1 to 5, and 7 to 10, leaving a window size of (sub5+sub6) for the stripline opening into the waveguide. Offset distance of these vias with respect to the edge of waveguide broad walls, namely parameter *y_offset,* are tuned to find the best performance. A close view of the feed section is given in Fig. 5-37.

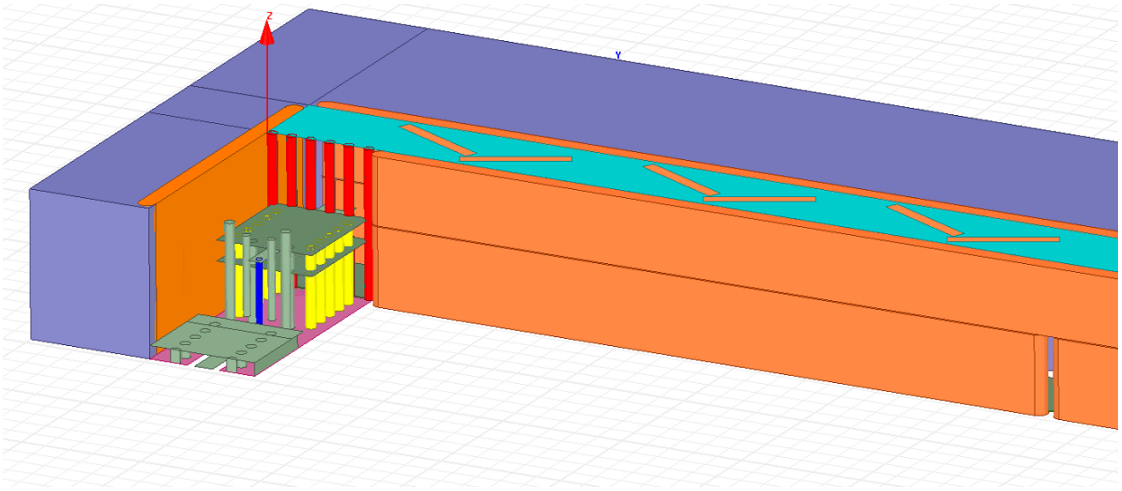

(a)

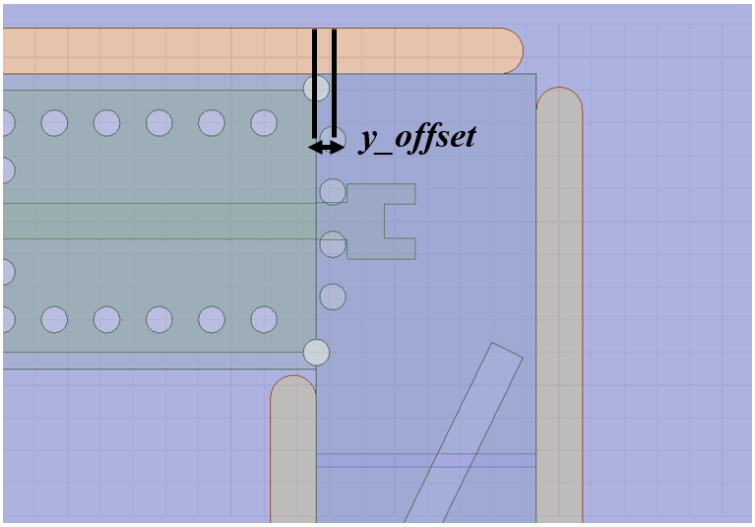

(b)

Fig. 5-37 Illustration of cavity vias (a) Cross sectional view (b) Top view.

The final stack up for this design with different types of vias are given in Appendix I. It can be seen that the feeding structure hosts a blind (buried) via, (indicated by Type 5 in Appendix I) that goes between sub2 to sub8. Since realization of buried via is difficult in practice, in the next stage of the design we plan to omit this buried via and also, reduce the number of drilling programs so the board can be realized with maximum 4 times lamination.

Results of reflection and insertion coefficients along with the far-field pattern of the antenna-feed configuration after modeling gaps and vias that create a cavity opening for feed line are given in Fig. 5-38.

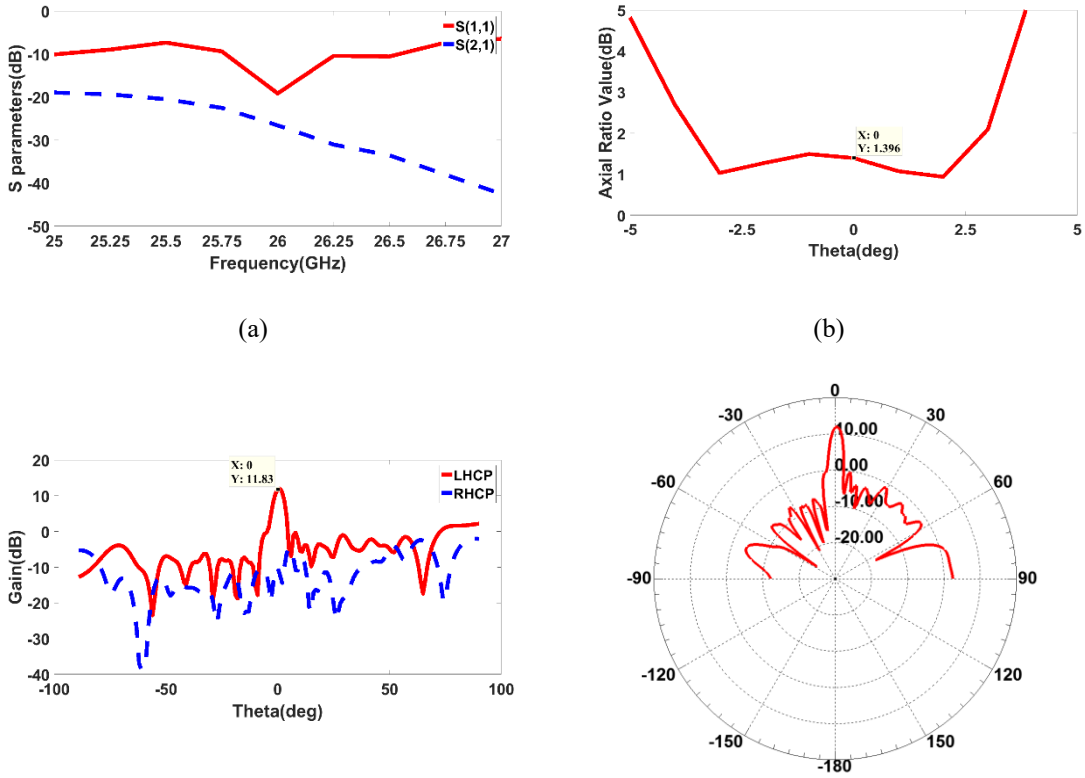

(a) (b)

(c) (d)

Fig. 5-38 Resultst for 13 element linear slot array and feed system after considering waveguide walls thickness and gaps (a) S-parameters, (b) Axial ratio, (c) Co (LHCP) and Cross (RHCP) Gains (d) Co-polarized radiation pattern.

5.7.3 Removing buried vias and keeping drill programming to maximum four laminations

In an attempt to omit some of the via programmings and to make the antenna more fabrication-friendly, we break the original design stack (shown in Appendix I) into two smaller stack ups each with maximum four number of laminations. One lamination is when all the layers are stacked, drilled and plated, then more layers must be added, stacked,

drilled and plated over. These two individual stack ups will be bonded together later to form the entire structure. As mentioned earlier here we have decided to break down the design into two stack ups identified with stack 1 and stack 2 in Appendix II. Stack 1 will include only the via programmings required to create metallic posts while stack 2 consists of drilling programs required for the feed section. This guarantees a much more simplified fabrication since maximum number of laminations in each stack is kept to four.

Probe feed along with the parasitic vias are omitted in this new design stack and instead of having to transfer signal from inner stripline to the grounded CPW on the bottom surface of the antenna, we manage to have a CPW transition on the same layer as the stripline. This way all the feeding section including stripline, CPW, and stripline channel (cavity) are kept in design stack 2, and once this is fabricated it will be bonded to the design stack 1 (consisting metal posts). Since the stacks will be attached together by hand using Teflon screws on four corners as opposed to an adhesive bonding film, a 40 um air gap is considered in the simulations to account for the imperfect bonding.

Fig. 5-39 shows the final structure using this new feeding technique where a stripline-CPW transition is used to feed the antenna. Also, metal layers are now replaced with copper with thickness 17.5 um. Considering a 40 um air gaps between two different stack ups, the new structure is simulated and, the results are given in Fig. 5-40.

Fig. 5-40 shows that the antenna is perfectly matched and, the far-field performance is as expected. Maximum Gain LHCP is 10.63 dB with axial ratio of 1.87 dB at broadside. Also posts offsets were tuned to keep the axial ratio below 3 dB over the angular region of 3 dB beamwidth. Gain drop observed in Fig. 5-40(c) compared to the original feeing is due to added dielectric loss in the new design as the width of the entire antenna structure had to extend over one wavelength in order to accommodate the CPW transition on both sides. (port 1 and 2)

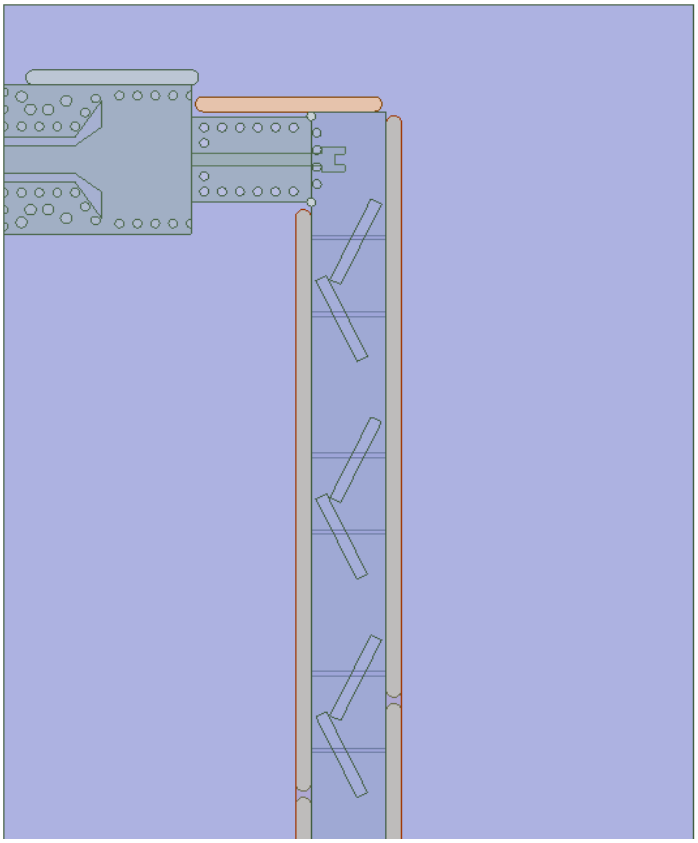

Fig. 5-39 New feeding technique for the stack up in Appendix II.

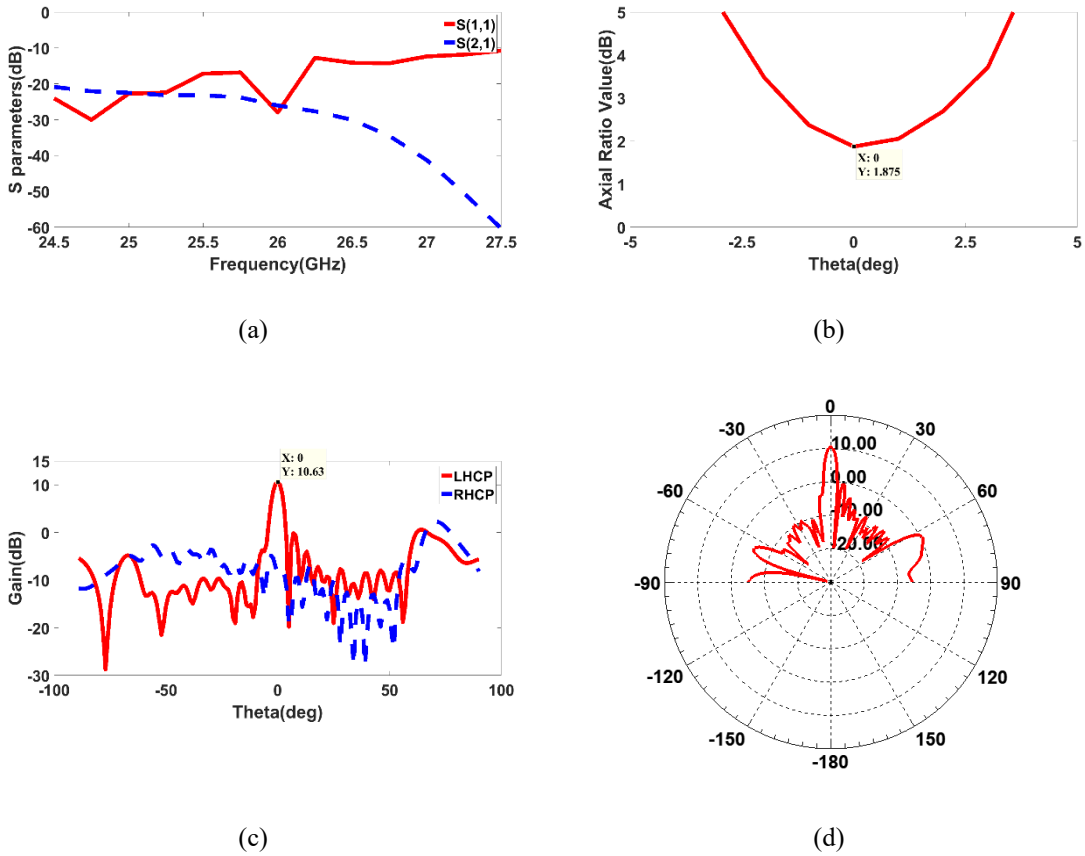

Fig. 5-40 Results for 13 element linear slot array and feed system after breaking the design into two stack ups of maximum four laminations (a) S-parameters, (b) Axial ratio, (c) Co (LHCP) and Cross (RHCP) Gains (d) Co-polarized radiation pattern.

5.8 Conclusion

This chapter elaborates on the design, optimization and simulation of a narrow-wall circularly polarized slotted waveguide antenna array. Multi-layer PCB technology is chosen to realize the antenna configuration to provide more flexibility in terms of choice of feeding, waveguide cut off frequency and hence scaling the design to be used for higher/lower frequency bands. A step-by-step design of the feed section is presented through simulations and parametric study. Fabrication challenges are taken into account by offering two different design stack ups and changing the feeding section accordingly. The first design has the benefit of larger gain due to its more compact size whereas the second topology has a more simplified via programming. One of the notable features of the proposed design is the ability to accomplish CP on the unit cell level to avoid use of phase

shifters for cost, size and complexity reasons. Also, arrangement of slots on the narrow wall guarantees future developments of planar arrays will be low profile and also prevent intrusion of extra beams for wide angle beam scanning often required in 5G applications.

Chapter 6

6 Conclusion and Future Research

6.1 Conclusion

In this work, after a short introduction on 5G networks and review of literature we were convinced that realization of 5G vision is highly dependent on development of advanced antenna solutions. Two advanced antenna prototypes

A dual layer leaky-wave antenna

and

A circularly polarized narrow-wall waveguide slot antenna

Were selected to be designed. Some of the key features of these architectures are briefly discussed in chapter 1 which reveals their potential for the performance enhancement required in 5G base stations.

Different architectures of beam scanning antennas along with their advantages and drawbacks are reviewed and discussed in chapter 2.

In chapter 3, design and implementation of a novel dual layer vertically-stacked substrate integrated waveguide leaky-wave antenna (SIW LWA) has been proposed. This architecture is capable of providing service for variety of different scenarios with distribution of users in vertical and/or horizontal plane. The former is can be accomplished by steering of leaky beam in the elevation, whereas the realization of the latter vision has been made possible by multi spot flat-topped illumination of the azimuth plane through an arrangement of these antenna modules on a cylindrical array. Simulation and measurement results verified the proposed concept. A list of popular types of base station antennas along with their advantages and drawbacks are provided in the end of this chapter. Criteria used for comparison are taken from 5G five exemplary scenarios. Comparisons reveal that the proposed leaky-wave antenna is capable of tackling some of the challenges such as high gain and latency reduction, however when it comes to wide band applications, the beam-squint is an issue and strategies must be employed to improve and upgrade the proposed design in order to obtain a squint-free beam which is more suited for wide band base station systems.

Chapter 4 covers main challenges and problems associated with linear slot array design including how to achieve vertical, horizontal, arbitrary linear and circular polarizations. General requirements on array elements and aperture distributions to generate a broadside beam are discussed. The choice of hollow and dielectric loaded waveguides with regards to different performance parameters is addressed and justified.

Chapter 5 describes the design and simulation of a 13-element narrow-wall waveguide slotted linear antenna at 26 GHz. For more flexibility in feeding and cutoff frequency, a multi-layer PCB technology is used to simulate this prototype. After a review of concept for traveling-wave slot arrays, unit cell design is revealed in more details. A slot pair with reflection cancelling posts are chosen to achieve minimum return loss and CP at broadside for each unit cell. The linear antenna consisting of thirteen unit cells achieved 14.5 dB LHCP gain and 1.5 dB axial ratio on broadside. The stripline-vertical probe-CPW transition used for antenna feeding is explained in detail and, at the end the entire structure is optimized to meet the design goals. Among features that make this antenna a good candidate for 5G BSA systems are first, the possibility of generating CP radiation at the

unit cell level which eliminates the need for phase shifters and second, having slots on the narrow wall of the waveguide which is beneficial in developing low-profile planar arrays.

6.2 Future Work

Following is a list of suggestions for further research and future work.

- Regarding the beam squint problem of leaky-wave antenna presented in chapter 3, strategies must be developed to improve and upgrade the proposed design to obtain a squint-free beam which is more suited for wide band base station applications.
- Regarding the narrow-wall slot array, since the probe design limits the bandwidth of the waveguide to some degree, if more bandwidth is required, instead of a simple probe, a probe with three-branch-end or a fractal-end can be used.
- In chapter 5, one of the main goals was to achieve CP high directive beams for BSA while taking advantage of high-power handling and low-profile configuration that narrow-wall slot arrays offer. Since the proposed antenna is a high gain traveling wave array where unit cells are designed to have minimum reflection possible, and changes in geometry between adjacent unit cells are kept small, hence the mutual coupling is ignored. However, if more stringent design goals (for example on SLL) are required this factor should be considered.
- Considering the real-world application of base station antennas, adaptive beamforming (ABF) can be developed to maximize radiated power in the user direction by placing nulls in unwanted directions to minimize the interference and multipath fading of the signal. Also, in the planar array configuration mutual coupling between linear arrays can be compensated for by employing beamforming techniques.

References

[1] E. Dahlman, S. Parkvall, D. Astély, and H. Tullberg, "Advanced antenna solutions for 5G wireless access," in *2014 48th Asilomar Conference on Signals, Systems and Computers*, 2014, pp. 810–814.

[2] D. Muirhead, M. A. Imran, and K. Arshad, "Insights and Approaches for Low-Complexity 5G Small-Cell Base-Station Design for Indoor Dense Networks," *IEEE Access*, vol. 3, pp. 1562–1572, 2015.

[3] W. Roh *et al.*, "Millimeter-wave beamforming as an enabling technology for 5G cellular communications: theoretical feasibility and prototype results," *IEEE Commun. Mag.*, vol. 52, no. 2, pp. 106–113, Feb. 2014.

[4] W. Hong, K. Baek, Y. Lee, Y. Kim, and S. Ko, "Study and prototyping of practically large-scale mmWave antenna systems for 5G cellular devices," *IEEE Commun. Mag.*, vol. 52, no. 9, pp. 63–69, Sep. 2014.

[5] J. Park, J. Ko, H. Kwon, B. Kang, B. Park, and D. Kim, "A Tilted Combined Beam Antenna for 5G Communications Using a 28-GHz Band," *IEEE Antennas Wirel. Propag. Lett.*, vol. 15, pp. 1685–1688, 2016.

[6] K. Linehan and J. Robson, "What base station antenna configuration is best for LTE-Advanced?," *Commscope*, 2017.

[7] C. Beckman and B. Lindmark, "The Evolution of Base Station Antennas for Mobile Communications," in *2007 International Conference on Electromagnetics in Advanced Applications*, 2007, pp. 85–92.

[8] J. Gozalvez, "5G Tests and Demonstrations [Mobile Radio]," *IEEE Veh. Technol. Mag.*, vol. 10, no. 2, pp. 16–25, Jun. 2015.

[9] F. Xu and K. Wu, "Guided-wave and leakage characteristics of substrate integrated waveguide," *IEEE Trans. Microw. Theory Tech.*, vol. 53, no. 1, pp. 66–73, Jan. 2005.

[10] D. Deslandes, "Design equations for tapered microstrip-to-Substrate Integrated Waveguide transitions," in *2010 IEEE MTT-S International Microwave Symposium*, 2010, pp. 704–707.

[11] J. Xu, W. Hong, H. Tang, Z. Kuai, and K. Wu, "Half-Mode Substrate Integrated Waveguide (HMSIW) Leaky-Wave Antenna for Millimeter-Wave Applications," *IEEE Antennas Wirel. Propag. Lett.*, vol. 7, pp. 85–88, 2008.

[12] F. Xu, K. Wu, and X. Zhang, "Periodic Leaky-Wave Antenna for Millimeter Wave Applications Based on Substrate Integrated Waveguide," *IEEE Trans. Antennas Propag.*, vol. 58, no. 2, pp. 340–347, Feb. 2010.

[13] C. Caloz, T. Itoh, and A. Rennings, "CRLH metamaterial leaky-wave and resonant antennas," *IEEE Antennas Propag. Mag.*, vol. 50, no. 5, pp. 25–39, Oct. 2008.

[14] L. Liu, C. Caloz, and T. Itoh, "Dominant mode leaky-wave antenna with backfire-to-endfire scanning capability," *Electron. Lett.*, vol. 38, no. 23, pp. 1414–1416, Nov. 2002.

[15] Y. Li, Q. Xue, E. K. Yung, and Y. Long, "The Periodic Half-Width Microstrip Leaky-Wave Antenna With a Backward to Forward Scanning Capability," *IEEE Trans. Antennas Propag.*, vol. 58, no. 3, pp. 963–966, Mar. 2010.

[16] Y. Dong and T. Itoh, "Composite Right/Left-Handed Substrate Integrated Waveguide and Half Mode Substrate Integrated Waveguide Leaky-Wave Structures," *IEEE Trans. Antennas Propag.*, vol. 59, no. 3, pp. 767–775, Mar. 2011.
[17] J. L. Gomez-Tornero, F. D. Quesada-Pereira, and A. Alvarez-Melcon, "Analysis and design of periodic leaky-wave antennas for the millimeter waveband in hybrid waveguide-planar technology," *IEEE Trans. Antennas Propag.*, vol. 53, no. 9, pp. 2834–2842, Sep. 2005.
[18] J. Liu, D. R. Jackson, and Y. Long, "Substrate Integrated Waveguide (SIW) Leaky-Wave Antenna With Transverse Slots," *IEEE Trans. Antennas Propag.*, vol. 60, no. 1, pp. 20–29, Jan. 2012.
[19] A. Grbic and G. V. Eleftheriades, "Leaky CPW-based slot antenna arrays for millimeter-wave applications," *IEEE Trans. Antennas Propag.*, vol. 50, no. 11, pp. 1494–1504, Nov. 2002.
[20] L. M. Paulsen, "Study of and design procedure for dual circularly polarized waveguide slot arrays," Ph.D. Dissertation, Michigan Technological University, 2006.
[21] A. Mizutani, K. Sakakibara, N. Kikuma, and H. Hirayama, "Grating Lobe Suppression of Narrow-Wall Slotted Hollow Waveguide Millimeter-Wave Planar Antenna for Arbitrarily Linear Polarization," *IEEE Trans. Antennas Propag.*, vol. 55, no. 2, pp. 313–320, Feb. 2007.
[22] A. J. Martinez-Ros, J. L. Gomez-Tornero, and G. Goussetis, "Planar Leaky-Wave Antenna With Flexible Control of the Complex Propagation Constant," *IEEE Trans. Antennas Propag.*, vol. 60, no. 3, pp. 1625–1630, Mar. 2012.
[23] A. M. Patel and A. Grbic, "A Printed Leaky-Wave Antenna Based on a Sinusoidally-Modulated Reactance Surface," *IEEE Trans. Antennas Propag.*, vol. 59, no. 6, pp. 2087–2096, Jun. 2011.
[24] K. R. Mahmoud and A. M. Montaser, "Design of dual-band circularly polarised array antenna package for 5G mobile terminals with beam-steering capabilities," *Antennas Propag. IET Microw.*, vol. 12, no. 1, pp. 29–39, 2018.
[25] F. D. Kashani and S. Golmohammady, "Reliability analysis of the flat-topped multi-beam FSO communication link," in *6th International Symposium on Telecommunications (IST)*, 2012, pp. 500–505.
[26] H. Mosallaei and K. Sarabandi, "Antenna miniaturization and bandwidth enhancement using a reactive impedance substrate," *IEEE Trans. Antennas Propag.*, vol. 52, no. 9, pp. 2403–2414, Sep. 2004.
[27] F. Yang and Y. Rahmat-Samii, "Microstrip antennas integrated with electromagnetic band-gap (EBG) structures: a low mutual coupling design for array applications," *IEEE Trans. Antennas Propag.*, vol. 51, no. 10, pp. 2936–2946, Oct. 2003.
[28] G. P. Gauthier, A. Courtay, and G. M. Rebeiz, "Microstrip antennas on synthesized low dielectric-constant substrates," *IEEE Trans. Antennas Propag.*, vol. 45, no. 8, pp. 1310–1314, Aug. 1997.
[29] L. Matekovits, G. C. V. Colome, and M. Orefice, "Controlling the Bandlimits of TE-Surface Wave Propagation Along a Modulated Microstrip-Line-Based High Impedance Surface," *IEEE Trans. Antennas Propag.*, vol. 56, no. 8, pp. 2555–2562, Aug. 2008.
[30] L. Goldstone and A. Oliner, "Leaky-wave antennas I: Rectangular waveguides," *IRE Trans. Antennas Propag.*, vol. 7, no. 4, pp. 307–319, Oct. 1959.

[31] A. A. Oliner, "Leakage from higher modes on microstrip line with application to antennas," *Radio Sci.*, vol. 22, no. 06, pp. 907–912, Nov. 1987.
[32] M. Guglielmi and G. Boccalone, "A novel theory for dielectric-inset waveguide leaky-wave antennas," *IEEE Trans. Antennas Propag.*, vol. 39, no. 4, pp. 497–504, Apr. 1991.
[33] J. A. Encinar, "Mode-matching and point-matching techniques applied to the analysis of metal-strip-loaded dielectric antennas," *IEEE Trans. Antennas Propag.*, vol. 38, no. 9, pp. 1405–1412, Sep. 1990.
[34] Y. D. Dong and T. Itoh, "Composite right/left-handed substrate integrated waveguide leaky-wave antennas," in *2009 European Microwave Conference (EuMC)*, 2009, pp. 276–279.
[35] G. M. Zelinski, G. A. Thiele, M. L. Hastriter, M. J. Havrilla, and A. J. Terzuoli, "Half width leaky wave antennas," *Antennas Propag. IET Microw.*, vol. 1, no. 2, pp. 341–348, Apr. 2007.
[36] H. Ermert, "Guiding and radiation characteristics of planar waveguides," *IEE J. Microw. Opt. Acoust.*, vol. 3, no. 2, pp. 59–62, Mar. 1979.
[37] Y.-D. Lin, J.-W. Sheen, and C.-C. Tzuang, "Analysis and design of feeding structures for microstrip leaky wave antenna," *IEEE Trans. Microw. Theory Tech.*, vol. 44, no. 9, pp. 1540–1547, Sep. 1996.
[38] A. J. Martinez Ros, "Analysis and Synthesis of Leaky-Wave Devices in Planar Technology," *PhD Thesis*, 2014.
[39] N. Marcuvitz, *Waveguide Handbook*. IET, 1951.
[40] A. J. Martinez-Ros, J. L. Gómez-Tornero, and F. Quesada-Pereira, "Efficient Analysis and Design of Novel SIW Leaky-Wave Antenna," *IEEE Antennas Wirel. Propag. Lett.*, vol. 12, pp. 496–499, 2013.
[41] A. Mehdipour and G. V. Eleftheriades, "Leaky-Wave Antennas Using Negative-Refractive-Index Transmission-Line Metamaterial Supercells," *IEEE Trans. Antennas Propag.*, vol. 62, no. 8, pp. 3929–3942, Aug. 2014.
[42] Y. J. Cheng, W. Hong, K. Wu, and Y. Fan, "Millimeter-Wave Substrate Integrated Waveguide Long Slot Leaky-Wave Antennas and Two-Dimensional Multibeam Applications," *IEEE Trans. Antennas Propag.*, vol. 59, no. 1, pp. 40–47, Jan. 2011.
[43] J. Garrido-Holgado and J. L. Gómez-Tornero, "LTE low-cost vertical sectorization through a leaky-wave antenna," in *The 8th European Conference on Antennas and Propagation (EuCAP 2014)*, 2014, pp. 2061–2065.
[44] S. Gupta, S. Abielmona, and C. Caloz, "Microwave Analog Real-Time Spectrum Analyzer (RTSA) Based on the Spectral–Spatial Decomposition Property of Leaky-Wave Structures," *IEEE Trans. Microw. Theory Tech.*, vol. 57, no. 12, pp. 2989–2999, Dec. 2009.
[45] A. Osseiran *et al.*, "Scenarios for 5G mobile and wireless communications: the vision of the METIS project," *IEEE Commun. Mag.*, vol. 52, no. 5, pp. 26–35, May 2014.
[46] N. Ojaroudiparchin, M. Shen, and G. F. Pedersen, "8×8 planar phased array antenna with high efficiency and insensitivity properties for 5G mobile base stations," in *2016 10th European Conference on Antennas and Propagation (EuCAP)*, 2016, pp. 1–5.
[47] F. Aryanfar *et al.*, "Millimeter-wave base station for mobile broadband communication," in *2015 IEEE MTT-S International Microwave Symposium*, 2015, pp. 1–3.

[48] P. Hallbjorner, M. Bergstrom, M. Boman, P. Lindberg, E. Ojefors, and A. Rydberg, "Millimetre-wave switched beam antenna using multiple travelling-wave patch arrays," *Antennas Propag. IEE Proc. - Microw.*, vol. 152, no. 6, pp. 551–555, Dec. 2005.

[49] C. A. Fernandese, P. O. Frances, and A. M. Barbosa, "Shaped coverage of elongated cells at millimetrewaves using a dielectric lens antennas," in *1995 25th European Microwave Conference*, 1995, vol. 1, pp. 66–70.

[50] B. Johannisson, "Adaptive base station antennas for mobile communication systems," in *1998 IEEE-APS Conference on Antennas and Propagation for Wireless Communications (Cat. No.98EX184)*, 1998, pp. 49–52.

[51] Y. T. Lo and S. W. Lee, *Antenna Hand Book*, vol. II. Springer, 1993.

[52] R. K. Enjiu, C. AG, and M. B. Perotoni, "Slotted Waveguide Antenna Design Using 3D EM Simulation," *Microw. J.*, 2013.

[53] M. Bozzi, A. Georgiadis, and K. Wu, "Review of substrate-integrated waveguide circuits and antennas," *Antennas Propag. IET Microw.*, vol. 5, no. 8, pp. 909–920, Jun. 2011.

[54] M. Gomez and R. Henderson, "Printed circuit board rectangular waveguide with full band microstrip to waveguide transition," in *2016 Texas Symposium on Wireless and Microwave Circuits and Systems (WMCS)*, 2016, pp. 1–4.

[55] F. D. L. Peters, S. O. Tatu, and T. A. Denidni, "Design of traveling-wave equidistant slot antennas for millimeter-wave applications," in *2011 IEEE International Symposium on Antennas and Propagation (APSURSI)*, 2011, pp. 3037–3040.

[56] G. Montisci, "Design of Circularly Polarized Waveguide Slot Linear Arrays," *IEEE Trans. Antennas Propag.*, vol. 54, no. 10, pp. 3025–3029, Oct. 2006.

[57] H. Kai, J. Hirokawa, and M. Ando, "Analysis of inner fields and aperture illumination of an oversize rectangular slotted waveguide," *Antennas Propag. IEE Proc. - Microw.*, vol. 150, no. 6, pp. 415–421, Dec. 2003.

[58] S. Park, Y. Tsunemitsu, J. Hirokawa, and M. Ando, "Center feed single layer slotted waveguide array," *IEEE Trans. Antennas Propag.*, vol. 54, no. 5, pp. 1474–1480, May 2006.

[59] I. Kim, H. Choi, and K. W. Kim, "Ultra-wideband transition from stripline to conductor-backed coplanar waveguide," *Electron. Lett.*, vol. 51, no. 13, pp. 996–998, 2015.

[60] H. o Roy, S. Mandal, A. K. Shukla, and A. K. Kush, "Waveguide to suspended stripline transition techniques at 140 GHz," in *2008 International Conference on Recent Advances in Microwave Theory and Applications*, 2008, pp. 110–112.

[61] J. Dong, H. Peng, Y. Liu, H. Lin, and T. Yang, "Broadband suspended stripline to air-filled rectangular waveguide transition," *Electron. Lett.*, vol. 51, no. 23, pp. 1886–1888, 2015.

[62] Y. Wang, K. Gu, and Y. Shu, "Synthesis equations for shielded suspended substrate microstrip line and broadside-coupled stripline," in *1988., IEEE MTT-S International Microwave Symposium Digest*, 1988, pp. 331–334 vol.1.

Appendix I

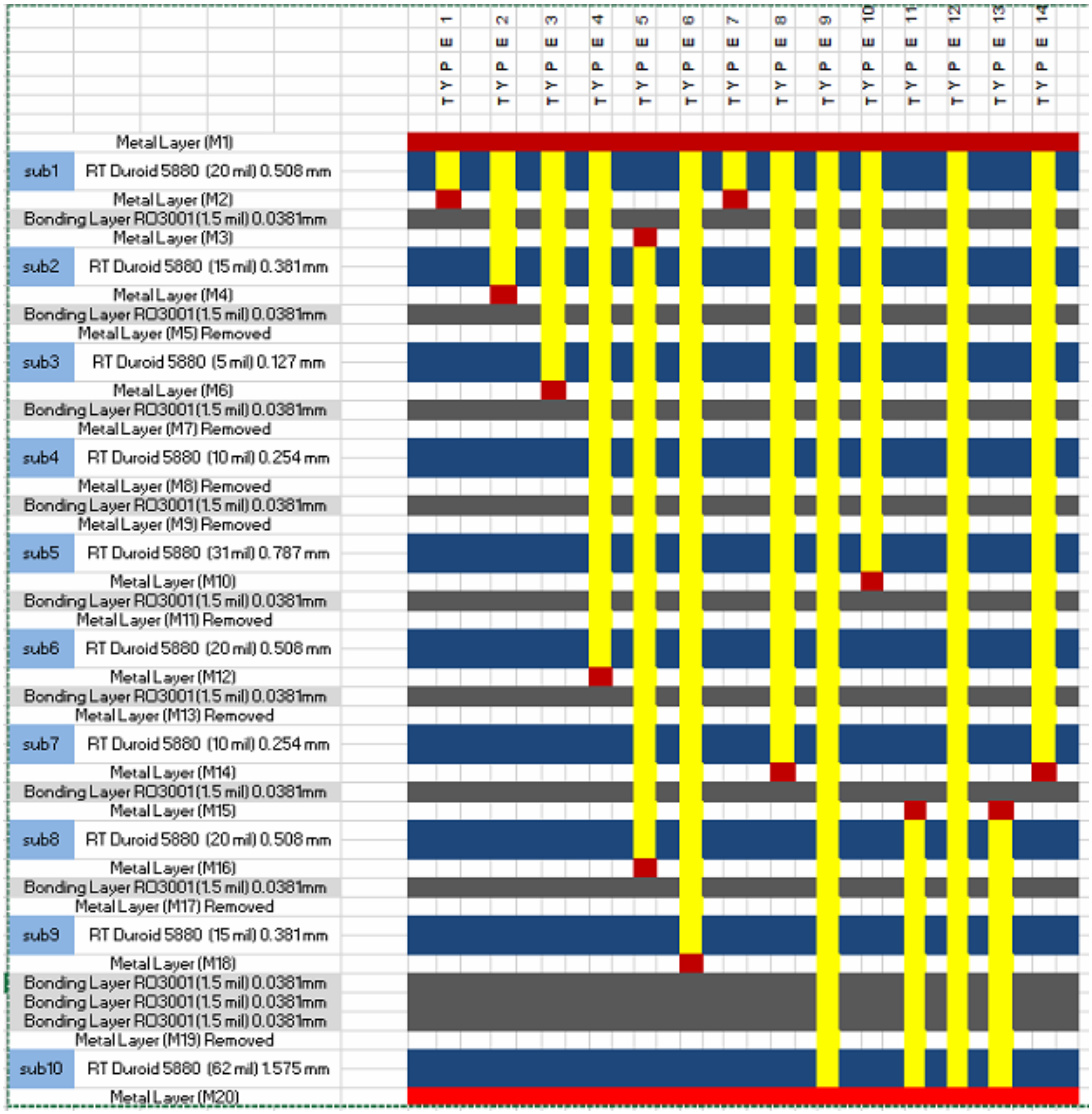

Fig. I- 1 First design of narrow-wall slot array with a 10-layer stack up.

Appendix II

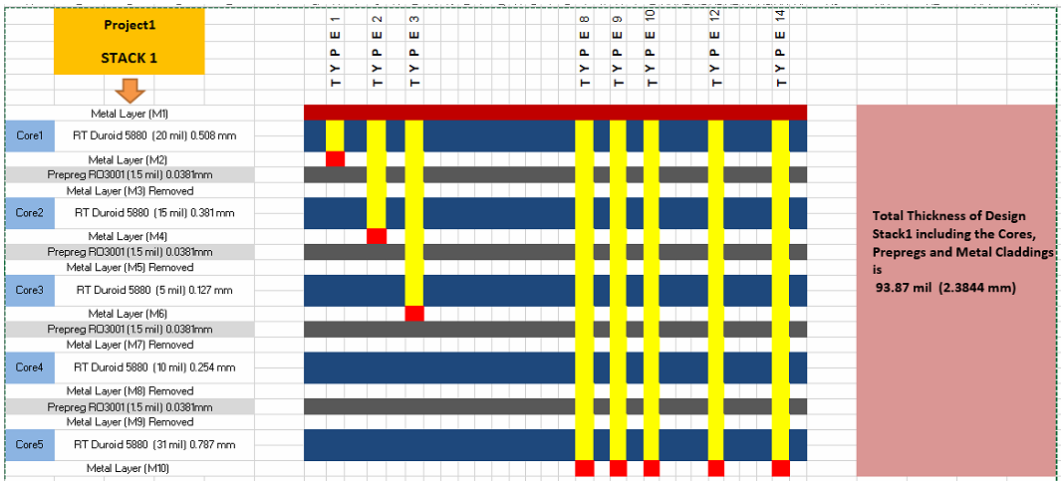

(a)

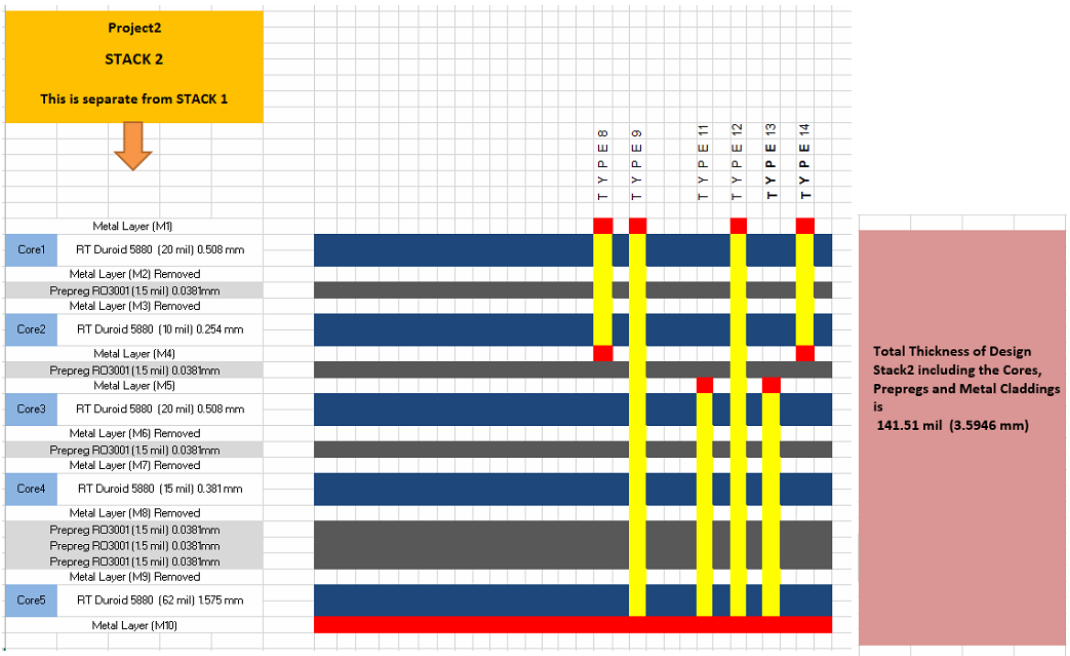

(b)

Fig. II- 1 Second design of narrow-wall slot array with (a) A 5-layer stack up with maximum four number of laminations and (b) A 5-layer stack up with three number of laminations.